Dimensional Crossover in a Photonic Quantum Gas

Dissertation

zur

Erlangung des Doktorgrades (Dr. rer. nat.)

der

Mathematisch-Naturwissenschaftlichen Fakultät

der

Rheinischen Friedrich-Wilhelms-Universität Bonn

vorgelegt von

Kirankumar Karkihalli Umesh

aus

Koppal

Bonn 2025

Angefertigt mit Genehmigung der
Mathematisch-Naturwissenschaftlichen Fakultät der
Rheinischen Friedrich-Wilhelms-Universität Bonn

Gutachter/Betreuer:	Prof. Dr. Martin Weitz
Gutachter:	Prof. Dr. Georg von Freymann
Tag der Promotion:	12.09.2025
Erscheinungsjahr:	2025

Abstract

For many-body quantum systems, dimensionality is known to exert a profound influence on the physical behaviour, allowing for the shaping of distinct phases of matter. In general, for lower dimensions, enhanced fluctuations serve to suppress long range order. For bosonic gases, for example, Bose-Einstein condensation in one dimension requires confinement that is stronger than linear in order to occur, in contrast to two-dimensional systems where harmonic confinement can suffice.

In this thesis, the dimensional crossover between one and two dimensions in a harmonically trapped photon gas has been experimentally investigated. The photons were confined within a dye filled optical microcavity, where polymer nanostructures produced by direct laser writing defined the trapping potential. By systematically adjusting the aspect ratio of the harmonic trap, the confinement was varied from an isotropic two dimensional regime to a highly anisotropic one dimensional regime.

The caloric properties of the photon gas were characterised across this transition, revealing that the sharp phase transition observed in two dimensions evolves into a smooth crossover in one dimension. This work enhances understanding of thermodynamic behaviour in photon Bose gases under confinement and demonstrates that here dimensionality can be used to tailor phase transition phenomena.

Furthermore, polymer cavities fabricated via direct laser writing afforded precise control over the confinement geometry, enabling exploration of variable potential landscapes. Proof of concept studies of advanced geometries, previously inaccessible, are presented, opening new directions for research in driven dissipative Bose gases and photonic quantum simulation platforms.

Publications

Portions of the work presented herein have been published:

- Karkihalli Umesh, K., Schulz, J., Schmitt, J., Weitz, M., von Freymann, G. and Vewinger, F., *Dimensional crossover in a quantum gas of light*. Nat. Phys. **20**, 1810–1815 (2024)

  DOI: 10.1038/s41567-024-02641-7

Further publications related to this thesis:

- E. Busley, L. Espert Miranda, A. Redmann, C. Kurtscheid, K. Karkihalli Umesh, F. Vewinger, M. Weitz, and J. Schmitt, *Compressibility and the Equation of State of an Optical Quantum Gas in a Box*. Science **375**, 1403-1406 (2022)

  DOI: https://doi.org/10.1126/science.abm2543

- S. Enns, J. Schulz, K. Karkihalli Umesh, F. Vewinger and G. v. Freymann, *Polarization properties of photon Bose-Einstein condensates*.arXiv preprint, arXiv:2506.06141 (2025)

  DOI: 10.48550/arXiv.2506.06141

Contents

CHAPTER 1

Introduction

In the field of condensed matter and many-body physics, low-dimensional systems immediately draw attention to the Hohenberg–Mermin–Wagner theorem [1, 2], which rules out long-range order in systems with short-range interactions due to enhanced fluctuations [3, 4]. This leads to the emergence of novel phases and states of matter that are absent in three-dimensional space. Notable examples include the Berezinskii–Kosterlitz–Thouless (BKT) transition [5–7] in lower dimensions [8–11] and Tomonaga–Luttinger-liquid physics in one-dimensional systems [12, 13]. These intriguing phases arise from the interplay between particle interactions and the effects of dimensionality. For instance, the loss of order in lower dimensions can be restored by introducing long-range interactions [14], as demonstrated in references [15–17]. A superfluid to supersolid transition arising due to the dimensional crossover in dipolar gases has been studied [18], and a transition from BKT to the TonksGirardeau regime has been observed in strongly-interacting bosons upon the dimensional crossover from two- to one-dimensions [19].

For ideal bosonic gases, Bose–Einstein condensation in low dimensions is only possible under strong confinement [20]. In two dimensions, a harmonically trapped gas can undergo a finite-temperature phase transition to a Bose–Einstein condensate. However, in one dimension, a similar transition is only observed under tighter confinement [20]. When a infinite sized one-dimensional system is confined harmonically, no sharply defined thermodynamic phase transition occurs; instead, a smooth crossover to a quasi-condensate is expected [21].

Optical quantum gases have recently emerged as a promising alternative platform for studying such dimensional crossovers [22]. Due to their weak or negligible interactions, these systems are ideally suited for exploring low-dimensional physics. Experimentally, the formation dynamics have been examined in one-dimensional system [23, 24] and in coupled lattices a Kardar–Parisi–Zhang scaling has been observed in polaritonic system [25] . In semiconductor microcavities, dimensional crossover has also been probed by modifying the drive geometry. A dissipative phase transition observed under two-dimensions vanishes when reduced to one-dimension [26].

In this work, a dye-filled optical microcavity platform is employed. The photons in this system, characterised by negligible interactions, allow for the study of nearly ideal Bose gas physics [27]. The inherently two-dimensional confinement in this platform is ideal for examining the physics of such interaction-less two-dimensional Bose, for example a

homogeneous 2D Bose gas [28]. Additionally, dissipation can be tuned from nearly lossless regime to that of a driven-dissipative condensate [29]

Dimensional tuning within this platform is, in principle, achievable by engineering highly asymmetric potential landscapes [30]. However, current techniques such as controlled mirror surface delamination [31], while effective in creating box potentials [28] and coupled lattice geometries [32], are limited in the curvatures they can produce [31] [28]. This limitation has been addressed in the present work by integrating polymer nanostructures fabricated via direct laser writing (DLW) into the dye microcavity. DLW, a well-established method [33–38] across fields from biology [39, 40] to photonics [41–44], enables sub-micrometre fabrication of complex polymer structures [38]. The structures fabricated in this manner within a microcavity act as effective potentials due to the refractive index contrast with the surrounding medium, enabling the realisation of high curvature one-dimensional geometries and thereby facilitating the study of dimensional crossover in photon gases.

This thesis is structured as follows. In Chapter 2, the theoretical framework underpinning photon gases in dye microcavities is presented, and thermodynamic quantities relevant for the study of the dimensional crossover are introduced. The chapter also discusses the dye-solution mediated thermalisation mechanism for photons, with emphasis on conditions under which thermalisation remains effective even in one-dimensional confinement.

Chapter 3 details the custom-built dye microcavity setup, which has been optimised to incorporate DLW-fabricated nanostructures. In Chapter 4, the DLW technique is introduced, along with the challenges of fabricating polymer structures on highly reflective cavity mirrors and the methods developed to overcome them.

In Chapter 5, the characterisation of two- to one-dimensional engineered potentials is presented, alongside experimental observations of the dimensional crossover in photon gases. A Bose–Einstein condensate phase transition is observed in an isotropic two-dimensional harmonic potential, while a gradual softening of the transition is identified in intermediate anisotropic geometries. A smooth crossover, rather than a distinct phase transition, is recorded in the one-dimensional harmonic confinement, supported by both population measurements and calorimetry.

In Chapter 6, new avenues enabled by direct laser writing (DLW) are explored through proof-of-concept studies of advanced potential geometries in previously inaccessible parameter regimes. The geometries investigated include small-footprint box potentials with rectangular and circular bases. Double-well potentials with substantially enhanced coupling, beyond that achieved previously, are demonstrated through the coupling of two zero-dimensional cylindrical structures. This progress facilitated the fabrication of extended one-dimensional lattice chains with coherent coupling, leading to the realisation of a Su–Schrieffer–Heeger (SSH) model [45–48] with detectable edge modes in the dye-microcavity platform. For the future, these developments open experimental routes to studying Kardar–Parisi–Zhang universality [49] in a driven-dissipative platform [50–57], the bosonic skin effect [58], and stable vortex formation in two-dimensional photon lattices [59]. In addition, efforts towards constructing a potential where condensation occurs below the single-photon threshold are presented, using a two-dimensional potential resembling two-level system [60] but with high terahertz scale mode spacing.

The fabrication, by the means of direct laser writing, of the polymer structures used in

this work has been carried out in the research group of Prof. Dr. Georg von Freymann at the Physics Department and Research Center OPTIMAS, RPTU Kaiserslautern-Landau, Kaiserslautern, Germany. The majority of the structures have been fabricated by Dr. Julian Schulz, while M.Sc. Sven Enns also contributed to the fabrication of some of the structures presented in Chapter 6. Both contributors are affiliated with the same research group.

CHAPTER 2

Theoretical background

In this chapter, the general theoretical framework of photon Bose-Einstein condensation in a dye-filled microcavity platform [27] [61] is discussed, here the photon number, rather than temperature, is typically employed as the tuning parameter to achieve condensation. To facilitate the experimental study of dimensional crossover in photon gases, the theoretical expectations for the nature of the transition from a classical to a quantum-degenerate phase are presented, as the dimensionality is reduced from two-dimensional (2D) to one-dimensional (1D) confinement within a harmonic oscillator potential. Intermediate regimes between isotropic 2D and purely 1D geometries hinder a straightforward mapping between the total photon number and an effective temperature, thereby limiting the applicability of conventional thermodynamic quantities such as the heat capacity at constant volume. In this context, the chemical potential like quantity $\tilde{\mu}$ is identified as a more suitable thermodynamic parameter, exhibiting distinct signatures that differentiate a Bose-Einstein condensation phase transition from a crossover as the 1D limit is approached.

Subsequently, the conditions required for realising a thermalised photon gas are examined, together with the ways in which the influence of dimensionality on the thermalisation mechanism may be suppressed.

2.1 Confinement for photons

For a Bose-Einstein condensate to form, a non-zero low-energy cutoff i.e., a non-trivial ground state is required [62]. This condition is not fulfilled for free photons, whose dispersion relation is linear in the wave vector $\vec{k}$. As a result, the minimum photon energy $\epsilon_0 = 0$ eV would correspond to a system with no photons. In order to allow for condensation, the photon dispersion must be modified to introduce a non-zero minimum energy. This modification may be achieved by introducing a strong confinement in one of the spatial dimensions. Specifically, by freezing the longitudinal (z) direction, the photons acquire a dispersion characteristic of massive particles, featuring an effective non-zero rest mass and a non-zero minimum energy [22, 63], as illustrated in Figure 2.1.

For photons, confining boundaries may be achieved using mirrors, thus forming an optical

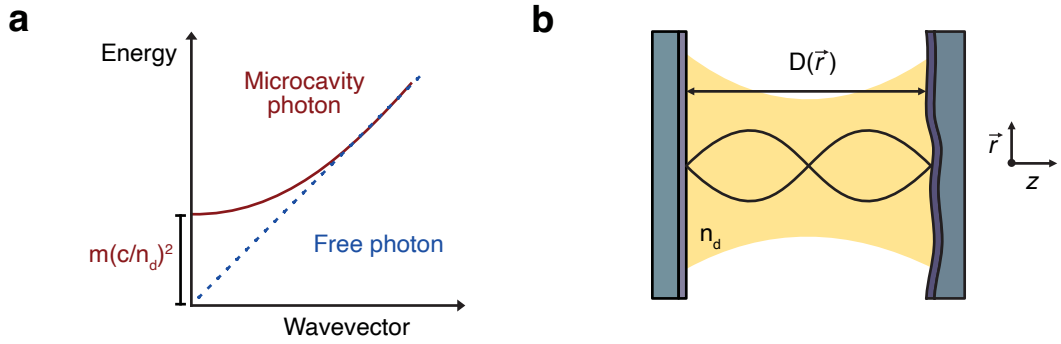

Figure 2.1: **a**. The dispersion relation, depicting the energy of a dimensional photon as a function of its wavevector $\vec{k}$, is shown. For free photons, the relation is linear (dashed blue line) as function of wavevector $\vec{k}$, whereas for photons confined in an optical cavity of micrometer-scale length (two-dimensional photons), the dispersion, which is a function of transverse wavevector $\vec{k}_r$ only, becomes parabolic (solid red curve) for a small transverse wavevector. **b**. A schematic of an optical microcavity is presented, illustrating strong confinement along the longitudinal (z) axis. The optical field in this direction forms a standing wave with a low longitudinal mode number q.

cavity resonator. Let the cavity mirror surfaces along the longitudinal axis be separated by a distance $D(\vec{r})$, where $\vec{r} = (x, y)$ defines the coordinates in the transverse plane. This spatial dependence of the cavity length will be utilised later for potential landscape engineering. The optical field inside the cavity forms a standing wave along the longitudinal axis, with the wave vector component

$$|k_z| = \frac{q\pi}{D_0}, \tag{2.1}$$

where D_0 is the maximum cavity length, and q is the longitudinal mode number ($q = 1, 2, 3, \ldots$). For sufficiently small D_0, the longitudinal component dominates the transverse one, i.e., $|k_z| \gg |k_r|$, where $k_r = \sqrt{k_x^2 + k_y^2}$. Under this condition, the photon dispersion relation becomes

$$E = \frac{\hbar c}{n_d}|\vec{k}| = \frac{\hbar c}{n_d}\sqrt{k_z^2 + k_r^2} = \frac{\hbar c}{n_d}k_z\sqrt{1 + \left(\frac{k_r}{k_z}\right)^2} \approx \frac{\hbar c}{n_d}\left(k_z + \frac{k_r^2}{2k_z}\right) \tag{2.2}$$

where $\hbar$ and c are the reduced Planck's constant and speed of light in vacuum respectively, with the latter being modified by the intra cavity medium refractive index n_d. In the final expression, a series expansion has been applied to the square-root term, and terms of order $O(k_r^3/k_z^3)$ have been neglected.

Let the transverse coordinate of the cavity be centred at the position of maximum cavity length D_0, such that $D(0) = D_0$. The cavity length at any transverse position can then be expressed as

$$D(\vec{r}) = D_0 - d(\vec{r}), \tag{2.3}$$

where $d(\vec{r})$ denotes the transverse modulation. This transverse position dependence of the

cavity length renders k_z a function of $\vec{r}$ and may be expressed as

$$k_z(\vec{r}) = k_z \frac{D_0}{D(\vec{r})} = \frac{q\pi}{D_0}\frac{D_0}{D(\vec{r})} = \frac{q\pi}{D(\vec{r})} = \frac{q\pi}{D_0 - d(\vec{r})} \tag{2.4}$$

substituting this in the dispersion relation 2.2 yields

$$E \approx \frac{\hbar c}{n_d}\left(\frac{q\pi}{D_0 - d(\vec{r})} + \frac{k_r^2}{2\pi q}(D_0 - d(\vec{r}))\right). \tag{2.5}$$

For sufficiently small modulation of the cavity length , i.e., $d(\vec{r}) \ll D_0$, the first term, $\frac{q\pi}{D_0 - d(\vec{r})}$, in Equation 2.5 may be expanded using a Taylor series, yielding $\frac{q\pi}{D_0}\left(1 + \frac{d(\vec{r})}{D_0}\right)$, while neglecting terms of order $O(d^2(\vec{r})/D_0^2)$. The second term simplifies to $\frac{k_r^2 D_0}{2\pi q}$. Substituting these into Equation 2.5 and rearranging gives

$$E \approx \frac{\hbar c}{n_d}\left(\frac{q\pi}{D_0} + \frac{k_r^2}{2\pi q}D_0 + \frac{q\pi d(\vec{r})}{D_0^2}\right) = \underbrace{\frac{m_{\text{eff}}c^2}{n_d^2}}_{\text{Rest Energy}} + \underbrace{\frac{\hbar^2 k_r^2}{2m_{\text{eff}}}}_{\text{Kinetic Energy}} + \underbrace{\frac{m_{\text{eff}}c^2}{n_d^2}\frac{d(\vec{r})}{D_0}}_{\text{Potential Energy}}. \tag{2.6}$$

Here, $m_{\text{eff}} = \frac{\hbar n_d q\pi}{cD_0}$ is the effective photon mass in the cavity and the dispersion relation resembles that of a massive boson, comprising rest, kinetic, and potential energy components. The rest energy serves as a low-energy cutoff, i.e., the minimum non-zero energy state into which photons may condense. The kinetic energy of the photons is governed by the potential landscape established through the transverse modulation of the cavity length, $d(\vec{r})$, which determines the system's Eigenenergies.

The transverse modulation of the cavity length, $d(\vec{r})$ need not only be the physical distance between the cavity mirrors but the effective optical path length. This modulation for example may be achieved in three different ways, which then leads to decomposition of the potentials energy as follows,

$$V(\vec{r}) \simeq \frac{m_{\text{eff}}c^2}{n_d^2}\frac{d(\vec{r})}{D_0} = \frac{m_{\text{eff}}c^2}{n_d^2}\left(\frac{\Delta d(\vec{r})}{D_0} + \frac{\Delta n(\vec{r})}{n_d} - \frac{n_s - n_d}{n_d}\frac{h(\vec{r})}{D_0}\right). \tag{2.7}$$

Here, the longitudinal optical path length is changed by the physical cavity length $\Delta d(\vec{r})$ in the first term, in the second term by creating a refractive index gradient $\Delta n(\vec{r})$ in the intra-cavity medium and finally in the last term by additive structuring of material with height profile $h(\vec{r})$ and refractive index n_s.

One-dimensional potentials required for the study of the dimensional crossover would require a method of modulating the optical path length with a lateral resolution much smaller than the wavelength of the photon gas or a potential of sufficiently high curvature, such that the second-dimensional bound state energy exceeds the thermal energy and the chemical

potential [30]. To achieve this, a novel method was developed in this work [1] to realise one-dimensional potentials exploiting the last term in Equation 2.1 as will be discussed in Chapter 4.

2.2 Statistical mechanics of an ideal Bose gas

As this study focuses on a photon gas confined within a dye microcavity platform, the interactions between the constituent particles, namely photons, may be neglected [27]. Consequently, the physics of the system may be accurately described by the Bose-Einstein distribution for an ideal Bose gas. The primary tuning parameter is taken to be the total photon number, rather than the temperature which is commonly used in cold atom experiments, for exploring the transition between classical and quantum degenerate phases. This choice necessitates the usage of the photon number based thermodynamic quantities in order to characterise the onset of condensation. Furthermore, the influence of finite-depth potentials on condensation into the quantum degenerate phase is also examined.

2.2.1 Bose-Einstein distribution

The probability of finding a photon with energy ϵ in a photon gas with temperature T and chemical potential μ is governed by the Bose-Einstein distribution [64–66]

$$N(\epsilon) = \frac{g(\epsilon)}{e^{(\epsilon-\mu)/k_{\mathrm{B}}T} - 1} \tag{2.8}$$

where $g(\epsilon)$ denotes the degeneracy of the energy level at energy ϵ. For large photon numbers, this function may also be interpreted as the population of photons at a given energy. Without loss of generality, the energy scale may be rescaled such that the minimum energy corresponds to zero, i.e. $\epsilon_0 = 0$. Summation over all energy levels yields the total photon number N

$$N = \sum_{\epsilon=0}^{\infty} N(\epsilon) = \sum_{\epsilon=0} \frac{g(\epsilon)}{e^{(\epsilon-\mu)/k_{\mathrm{B}}T} - 1} \ , \tag{2.9}$$

which fixes μ for a given temperature T. For systems with infinitely many bound sates or if thermal energy $k_{\mathrm{B}}T$ is much larger than the energy spacing between bound energy levels, this summation may be replaced by an integral over the continuous energy spectrum, with the degeneracy $g(\epsilon)$ replaced by the density of states $\rho(\epsilon)$ [67]

$$N = \int_0^{\infty} \frac{\rho(\epsilon)}{e^{(\epsilon-\mu)/k_{\mathrm{B}}T} - 1} \, d\epsilon \tag{2.10}$$

[1] in collaboration with J. Schulz and G. von Freymann from the RPTU Kaiserslautern-Landau, Kaiserslautern, Germany

2.2.2 Transition from the classical phase to the quantum degenerate phase

For a potential characterised by a density of states $\rho(\epsilon)$, two tuning parameters are available: the total photon number N and the temperature T. These parameters may be employed to induce a transition from the classical gas phase to a quantum degenerate phase such as a Bose–Einstein condensate (BEC). Historically, BEC was achieved in atomic Bose gases by lowering the temperature below a critical threshold T_c, while keeping the total particle number fixed. When $T < T_c$, a macroscopic occupation of the ground state was realised at the expense of the excited state population [62, 68, 69].

Alternatively, condensation may also be achieved by increasing the total particle number at a fixed temperature, in this case the total photon number N. As N increases, the population in excited states saturate, and the chemical potential approaches zero, $\mu \longrightarrow 0$, resulting in a macroscopic occupation of the ground state and the onset of condensation [64] [62].

Infinite potential

The realisation of Bose–Einstein condensation is not guaranteed in infinite systems. This behaviour may be quantified by decomposing the total photon number N, as expressed in Equation 2.10, into two contributions: the ground-state population N_0 and the total population in all excited states N_{ex}, given by

$$N = N_0 + N_{\text{ex}} = N_0 + \int_{\epsilon \neq 0}^{\infty} \frac{\rho(\epsilon)}{e^{(\epsilon-\mu)/k_{\text{B}}T} - 1} \, . \tag{2.11}$$

As the system transitions from the classical to the quantum degenerate phase, the absolute value of the chemical potential $|\mu|$ decreases from a finite value to zero. Under this condition, i.e $\mu = 0$, the population in the excited states becomes the saturation photon number N_s, defined as

$$N_s = \int_{\epsilon \neq 0}^{\infty} \frac{\rho(\epsilon)}{e^{\epsilon/k_{\text{B}}T} - 1} \, . \tag{2.12}$$

The value of N_s depends on the form of the density of states $\rho(\epsilon)$. Table 2.1 lists $\rho(\epsilon)$ and the corresponding saturation photon number N_s for three different potential shapes.

Potential	$\rho(\epsilon)$	N_s
2D Harmonic oscillator	$\propto \epsilon$	Finite
2D Box	$\propto \epsilon^0$	∞
1D Harmonic oscillator	$\propto \epsilon^0$	∞

Table 2.1: Density of states $\rho(\epsilon)$ and saturation photon number N_s for three different potential shapes.

It is evident that not all infinitely deep potentials in one or two dimensions yield a finite saturation photon number N_s, and thus Bose–Einstein condensation into the quantum degenerate phase may not occur. However, in most experimental systems, the potentials are

neither infinitely deep nor unbounded in spatial extent. Instead, they possess a finite depth V_0 and finite spatial extent, which restores a finite value for N_s, as discussed below.

Finite potential depth

For potentials of finite depth V_0, Equation 2.9 becomes

$$N = N_0 + N_{\text{ex}} = N_0 + \sum_{\epsilon \neq 0}^{\epsilon_{\text{max}}} \frac{g(\epsilon)}{e^{\epsilon/k_{\text{B}}T} - 1} , \tag{2.13}$$

where ϵ_{max} denotes the highest bound state energy level. The corresponding saturation photon number at fixed temperature T is given by

$$N_s = \sum_{\epsilon \neq 0}^{\epsilon_{\text{max}}} \frac{g(\epsilon)}{e^{\epsilon/k_{\text{B}}T} - 1} . \tag{2.14}$$

For potentials of finite depth, with ϵ_{max} being finite, it might be expected that the summation in Equation 2.14 would be finite, thereby ensuring convergence and a finite value of N_s. However, this expectation holds only for potentials that support a finite number of bound states, which is not a universal property of all finite-depth potentials.

In particular, certain classes of potentials, such as a two-dimensional box potential with finite wall height (i.e., finite depth) but infinite lateral extent, or a slowly decaying confining potentials, may support an infinite number of bound states despite having a finite depth [70]. In such cases, the summation over bound states does not necessarily converge. This condition is related to what is sometimes referred to as the Bergmann bound.

All potentials considered in the present study are spatially and energetically constrained to support a finite number of bound states. Therefore, the summation in Equation 2.14 is always finite, and a finite saturation photon number N_s is guaranteed, regardless of the potential shape. This ensures that the system may reach a macroscopic occupation of the ground state, thereby entering the quantum degenerate phase. However, this does not necessarily imply that a discontinuity in a thermodynamic quantity is present, as would be the case in an infinite system. Consequently, the quantum degenerate phase of the system may not persist in the thermodynamic limit [21, 66].

2.2.3 Thermodynamic quantities

As established in Section 2.2.2, a quantum degenerate phase, characterised by a macroscopic population of the ground state, can be reached for all finite potentials satisfying the saturation condition. The nature of the transition from the classical phase to the quantum degenerate phase then becomes of interest. Specifically, it is necessary to determine whether this transition constitutes a true phase transition or merely a smooth crossover.

In classical thermodynamics, the characteristics of gases governed by classical statistics, including their phases and the nature of transitions between them, are often studied through thermodynamic quantities. These quantities also prove valuable when analysing gases obeying non-classical statistics, such as a photon gas governed by Bose–Einstein statistics. Among

these, the heat capacity at constant volume C_V as a function of temperature T is frequently utilised to probe second order phase transitions. In interacting Bose systems such as superfluid ^{4}He, a sharp divergence in C_V, often referred to as a lambda peak, is observed. This feature is classified in modern terminology as a second order (continuous) transition, although it does not conform neatly to Ehrenfest's rule on account of its logarithmic divergence [62]. [2]

However, the definitions of thermodynamic quantities such as volume and pressure in the used power-law confined system are not straightforward, as they depend on the geometry of the confining potential. Consequently, it is beneficial to employ a thermodynamic quantity that is general and can be applied consistently across potentials of different dimensionalities. Further, it is the photon number, rather than the temperature, that is employed as the control parameter. To this end, the following quantity is introduced :

$$\tilde{\mu} = \frac{\partial U}{\partial N}, \tag{2.15}$$

where U is the internal energy of the photon gas [3], defined as

$$U = \sum_{\epsilon=0}^{\epsilon_{\max}} \epsilon N(\epsilon) = \sum_{\epsilon=0}^{\epsilon_{\max}} \epsilon \frac{g(\epsilon)}{e^{(\epsilon-\mu)/k_{\mathrm{B}}T} - 1}. \tag{2.16}$$

Since the ground-state energy is rescaled to zero, the internal energy can be decomposed as

$$U = U_0 + U_{\mathrm{ex}} = U_{\mathrm{ex}}, \tag{2.17}$$

and hence depends solely on the population of the excited states [4].

As the total photon number N is increased, the population of the excited states is raised, resulting in a corresponding increase in the internal energy. For systems that support a true phase transition, such as the isotropic 2D harmonic oscillator, a critical total photon number exists beyond which the population in excited states saturate. Any additional photons then occupy the ground state, which lies at zero energy. Consequently, the internal energy ceases to increase, and the derivative $\tilde{\mu} = \partial U/\partial N$ exhibits an abrupt change, thereby serving as a useful indicator of phase transition behaviour.

[2] Bose Einstein condensation in an ideal Bose gas (confined in a potentials with density of states which grow slower than linear in energy) is regarded as a higher order phase transition [65] [62], since a discontinuity appears in one of the higher derivatives of the Helmholtz free energy F with respect to temperature at the critical temperature T_c. Conversely, a smooth variation of that same higher derivative is taken to signify a crossover. Nonetheless, care must be taken depending on the system in consideration [62].

[3] The quantity $\tilde{\mu}$ is analogous to the chemical potential but is not identical. In standard homogeneous thermodynamic systems, the chemical potential is defined as $\mu = (\partial U/\partial N)_{S,V}$, that is, at constant entropy S and volume V [64, 65]. However, this condition is not fulfilled in the present system, which involves a dimensional crossover from a two-dimensional to a one-dimensional harmonic potential. In this context, the notion of volume is non-trivial and must be replaced by a harmonic volume. More critically, the entropy, specifically the photonic contribution, excluding the dye solution acting as a heat bath, is not held constant [71]. Consequently, the quantity $\tilde{\mu} = \partial U/\partial N$ must be regarded as distinct from the conventional chemical potential μ.

[4] The ground state contribution to the internal energy is set to zero owing to the rescaling of the bound energy levels such that the ground state energy satisfies $\epsilon_0 = 0$

In contrast, for systems in which no true phase transition occurs, i.e. where population in excited states do not exhibit a sharply defined saturation point, it is found that U changes smoothly with N. In such cases, a continuous crossover from the classical to the quantum degenerate phase takes place, which is also captured by the smooth behaviour of $\tilde{\mu}$.

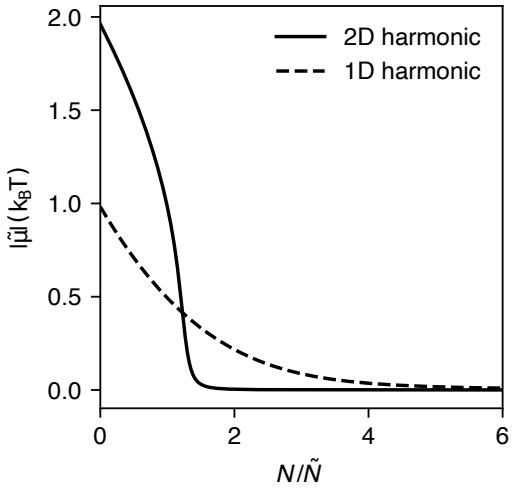

Figure 2.2: Comparison of, numerically calculated, $|\tilde{\mu}|$ (in units of $k_{\mathrm{B}}T$) as a function of normalised total photon number $N/\tilde{N}$ for isotropic 2D and 1D harmonic oscillator potentials with finite depth $V_0 = 10k_{\mathrm{B}}T$.

This hypothesis is tested for harmonic oscillator potentials, as listed in Table 2.1, with finite depth. The finite nature of the system ensures that condensation is possible regardless of dimensionality. Figure 2.2 shows the absolute value of $\tilde{\mu}$, normalised by thermal energy $k_{\mathrm{B}}T$, as a function of the normalised total photon number for both the isotropic 2D and 1D harmonic oscillator potentials with $V_0 = 10k_{\mathrm{B}}T$. The normalisation constant $\tilde{N}$ is defined such that $\tilde{\mu}(\tilde{N}) = \tilde{\mu}(N \to 0)/2$. Unlike the infinite case, the 1D system exhibits a transition from classical behaviour ($|\tilde{\mu}| \gg 0$) to the quantum degenerate phase ($|\tilde{\mu}| = 0$), confirming that finite depth permits condensation even in lower-dimensional systems.

However, the nature of this transition varies with potential geometry, in this case dimension. In the isotropic 2D harmonic oscillator, $|\tilde{\mu}|$ shows an abrupt decline, characteristic of a phase transition. Conversely, in the 1D harmonic oscillator, $|\tilde{\mu}|$ decreases smoothly, indicating a crossover rather than a sharp transition.

Effects of a finite potential depth

In practical experimental setups, the potential depth for the photon gas in the dye microcavity is not infinitely large, but typically ranges between $1k_{\mathrm{B}}T$ and $1.3k_{\mathrm{B}}T$. To investigate the influence of finite potential depth on the transition behaviour, $\tilde{\mu}$ was computed as a function of the normalised total photon number for both isotropic 2D and 1D harmonic oscillator potentials. The potential depth V_0 was varied from $0.5k_{\mathrm{B}}T$ to $14k_{\mathrm{B}}T$, while the trap frequencies, $\omega = 2\pi \times 0.22$ THz, were held constant, as shown in Figure 2.3.

The results indicate that the qualitative nature of the transition, namely the curvature of $|\tilde{\mu}|$, is not altered by variations in the potential depth V_0 for either geometry. However, the

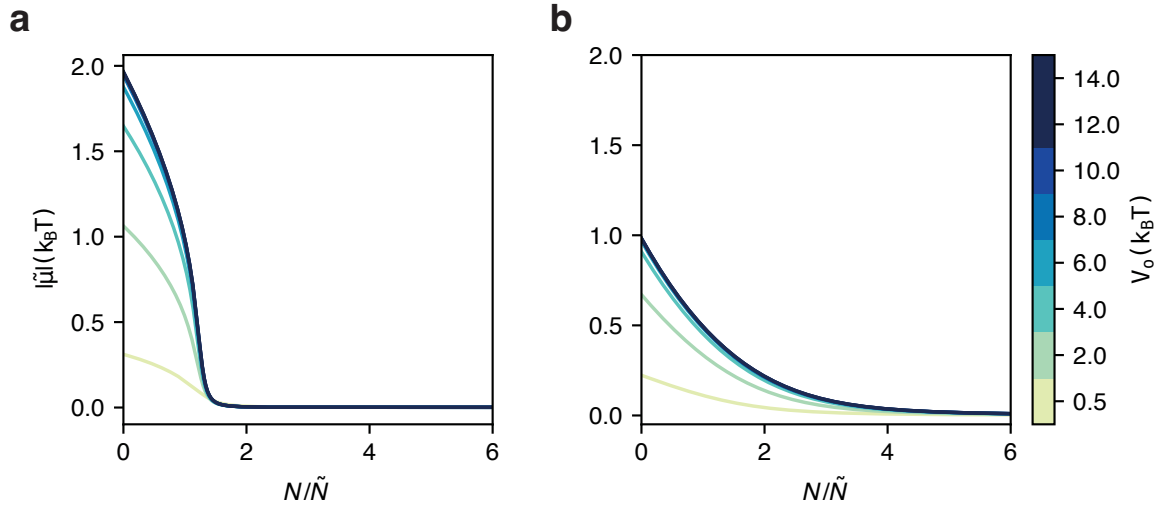

Figure 2.3: The effects of the potential depth V_0 on $|\tilde{\mu}|$ as a function of the total photon number are shown in panels **a** and **b** for isotropic two-dimensional and one-dimensional harmonic oscillator potentials, respectively.

low photon number limit (classical limit) values of $|\tilde{\mu}|$ are found to decrease as V_0 is reduced. It may therefore be anticipated in experiments that these low photon number limit values of $|\tilde{\mu}|$ depend on both the potential depth and the dimensionality, while it's curvature reflects a purely dimensional effect.

2.3 Photon gas thermalisation

To realise a Bose-Einstein condensate (BEC) of photons, a number conserving thermalisation mechanism is required.

Thermalisation, in the context of gases composed of particles, refers to the redistribution of energy among the constituents until thermal equilibrium is attained. At equilibrium, thermodynamic quantities such as temperature become well defined, and the microscopic states of the system obey the appropriate statistical distributions: Maxwell-Boltzmann for classical particles, Bose-Einstein for bosons, and Fermi-Dirac for fermions.

Photons, unlike atoms or molecules, do not thermalise via particle-particle collisions in free space. Although photon-photon interactions are not strictly forbidden, they occur with exceedingly low probability and negligible strength [72]. Nevertheless, thermalisation of photons can occur through absorption and re-emission processes by a blackbody, yielding a state as described by Planck's law of blackbody radiation [64, 65]. However, this process does not conserve photon number, as photons are lost to the environment upon temperature reduction, and the chemical potential μ remains pinned at zero.

To overcome this limitation, number conserving thermalisation of visible photons has been demonstrated using fluorescent dye molecules, such as Rhodamine 6G dissolved in ethylene glycol, confined within a high-finesse microcavity [27, 61]. More recently, thermalisation has also been achieved for photons in the infrared regime using semiconductor quantum wells in a

microcavity [73] [74], and with erbium-ytterbium co-doped optical fibre cavities [75].

2.3.1 Photon thermalisation via dye solution bath

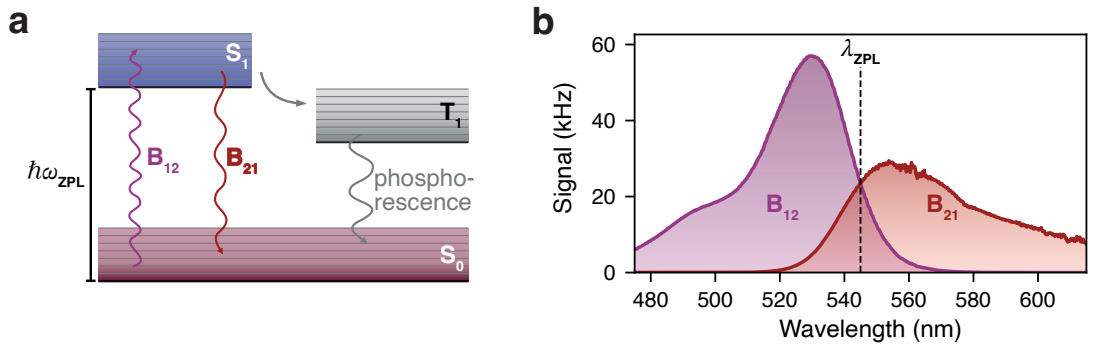

Figure 2.4: Rhodamine 6G dye properties. **a.** A simplified Jablonski diagram is shown, depicting the electronic state and corresponding rovibrational manifold relevant to the fluorescence cycle of Rhodamine 6G. The dye molecule is excited from its singlet ground state manifold S_0 to the excited singlet manifold S_1 through photon absorption, as described by the Einstein coefficients, with rate B_{12}. De-excitation proceeds predominantly via the fluorescence channel, characterised by the rate B_{21}, with the zero-phonon line energy indicated by $\hbar\omega_{\mathrm{ZPL}}$. Less probable decay pathways include non-radiative transitions and inter-system crossing to the triplet state T_1, followed by phosphorescence. These are illustrated in grey. **b.** The absorption and emission spectra, corresponding to the rates B_{12} and B_{21} respectively, are presented for Rhodamine 6G in an ethylene glycol environment at an ambient temperature of 300 K. The zero-phonon line, located at $\lambda_{\mathrm{ZPL}} = 545$ nm, is marked by a black dashed line. The data have been replotted from the database [76].

Photons are considered to be thermalised to the dye solution (comprising dye molecules and solvent) when the following conditions are met: (1) Chemical equilibrium between the photons and the dye molecules is established, and (2) an equilibrium distribution is acquired by the photons, characterised by a spectral temperature matching that of the dye solution [27, 61, 77].

Although exact equilibrium is challenging to realise, it can be closely approximated by employing dye molecules with high quantum efficiency, which minimises non-radiative losses. Rhodamine 6G, for instance, exhibits a quantum yield of approximately 95% [78, 79]. Additionally, the cavity lifetime is required to exceed the thermalisation time, the latter being on the order of the dye reabsorption time [27, 61, 77].

The mapping of ambient temperature to spectral temperature via the thermalisation mechanism may be understood with reference to the simplified Jablonski diagram in Figure 2.4. Rhodamine 6G molecules possess a ground electronic singlet state (S_0) and a first excited singlet state (S_1), each of which contains a rovibrational manifold arising from the molecule's internal structure. Upon absorption of a photon with energy $\hbar\omega$, an electronic transition is induced from a rovibrational level in the ground state to one in the excited state. The excited state has a lifetime of the order 10^{-9} s [78–80].

As the dye molecules are immersed in a solvent at ambient temperature T, frequent collisions with solvent molecules occur. These collisions induce rapid non-radiative transitions among rovibrational levels, on a timescale of the order 10^{-12} s. Consequently, thermal distributions are established within the rovibrational sublevels of both electronic states [80, 81].

This results in the Kennard-Stepanov relation, which connects the absorption spectrum $\alpha(\omega)$ and the fluorescence spectrum $f(\omega)$ via a Boltzmann factor associated with the spectral temperature of the bath. Within the spectral range from 550 nm to 600 nm, the relation takes the form

$$\frac{f(\omega)}{\alpha(\omega)} \propto \omega^3 \exp\left[-\frac{\hbar(\omega - \omega_{\mathrm{ZPL}})}{k_{\mathrm{B}}T}\right], \tag{2.18}$$

where $\hbar\omega_{\mathrm{ZPL}}$ denotes the energy of the zero-phonon line associated with a pure electronic transition in the molecule [82].

Under typical experimental conditions, the average time between photon emission and reabsorption is in the order of picoseconds, if not less [27]. This interval is considerably shorter than the photon lifetime, which is typically on the order of several hundred picoseconds (see Section 3.1.1). Therefore, efficient thermalisation can be achieved through repeated absorption and emission events, provided that the reabsorption time is sufficiently short, as demonstrated in previous studies in dye filled microcavity platform [27, 29, 61, 83, 84].

2.3.2 Suppression of dimensional effects on thermalisation

Thermalisation via coupling to an external bath, such as a dye solution, not only allows thermalisation for non-interacting bosons but also mitigates the influence of reduced dimensionality. In low-dimensional systems, such as one-dimensional confinements, thermalisation through particle collisions is hindered or even entirely suppressed due to integrability [85, 86]. Experimental observations have confirmed the absence of thermalisation in atomic Bose gases confined to one dimension [87, 88].

A simplified explanation is as follows: in a pairwise elastic collision between two identical particles of equal mass, energy and momentum conservation allows only for momentum exchange. In the quantum regime, particles may either transmit or reflect, but for indistinguishable particles, the final state remains unchanged, preventing any redistribution of momentum and, hence, inhibiting thermalisation [89, 90].

By contrast, bath-mediated thermalisation avoids these constraints. Since the bath remains three-dimensional, even when the bosonic system is confined to a lower dimension, thermalisation proceeds unimpeded [91, 92]. For this reason, the use of a three-dimensional dye solution bath is particularly effective in suppressing dimensionality induced hindrances to the thermalisation of photon gases confined in one dimension.

CHAPTER 3

Dye microcavity experimental setup

In this chapter, a detailed description of the dye microcavity experimental setup is provided. The setup has been optimised for the operation with photon gas potentials realised through polymer nanostructures. A comprehensive discussion of this novel fabrication technique applicable to the dye microcavity platform is presented in Chapter 4.

In addition to the usual constraints imposed by the dye microcavity platform [27, 28, 31, 93], the design also addresses specific challenges such as the pumping of the dye for highly elongated potentials and operation at low intra-cavity photon numbers.

The preparation and measurement of the photon gas require three main components: (1) the optical microcavity, (2) the dye excitation light source and its spatial beam shaping for introducing photons into the cavity (dye microcavity pumping setup), and (3) the measurement setup, which utilises the transmitted radiation through the cavity mirrors. These setups are discussed in Sections 3.1, 3.2, and 3.3, respectively.

3.1 Optical microcavity

The optical microcavity is composed of highly reflective mirrors that permit the excitation (pump) light for the dye to enter the cavity while remaining reflective for the photon gas. These mirrors are integrated with a mounting platform, which enables tuning of essential cavity parameters such as the cavity length along the longitudinal axis, the transverse position, and the angular tilt of the mirrors as shown in Figure 3.1 [1].

3.1.1 Cavity mirrors

In order to confine photons within the cavity for durations on the order of 10^{-9} s, exceeding the thermalisation timescale, two highly reflective mirrors are employed. A reflectivity exceeding 99.998% was achieved by selecting super-polished glass substrates with a root-mean-square

[1] The cantilevered mount was designed and fabricated at the IAP mechanical workshop by Mr. W.Graf

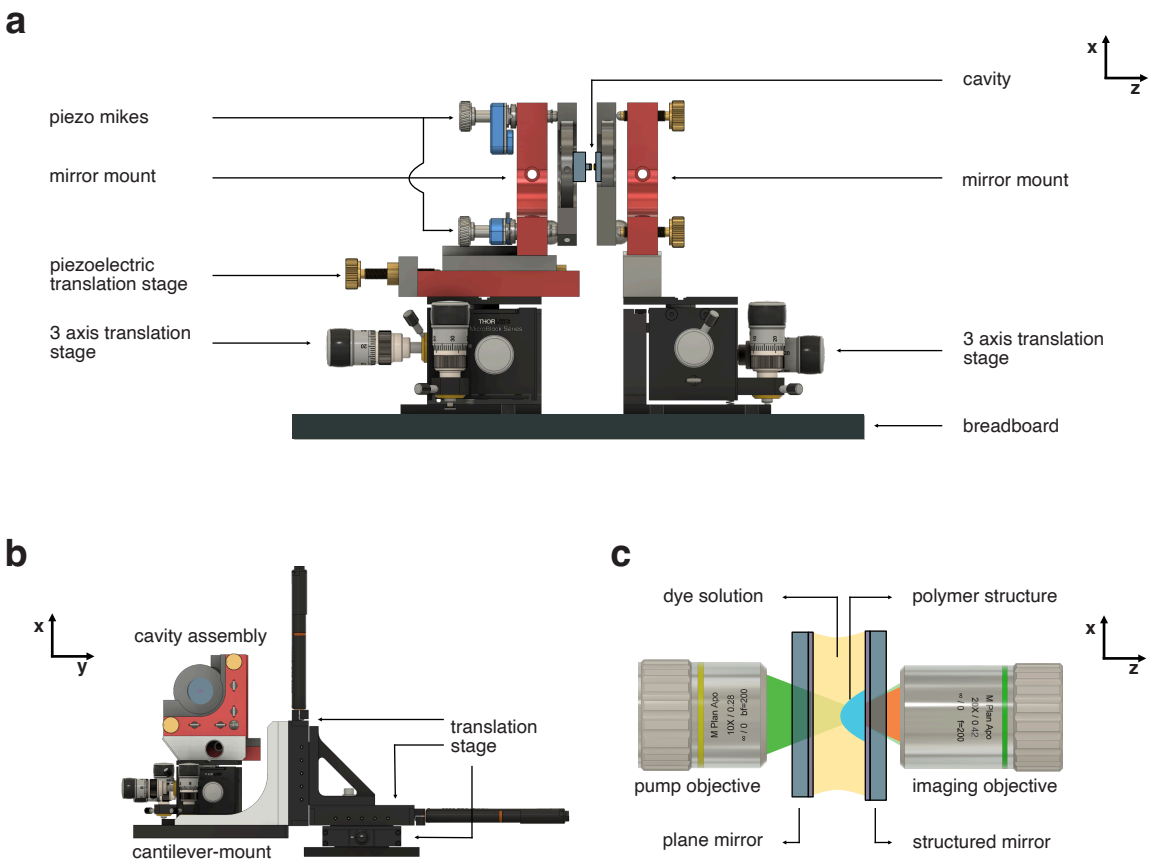

Figure 3.1: Dye-filled optical microcavity setup.**a.** Illustration of the cavity assembly is shown. The mirrors are mounted on mirror holders, with the left holder equipped with piezoelectric actuators (piezo-mikes) for tilt adjustment. This holder is further mounted on an open-loop piezoelectric translation stage. Both mirrors are aligned by a three-axis translation stage. **b.** The cavity assembly is mounted on a cantilevered three-axis stage equipped with a spring suspension system, allowing alignment of the cavity's optical axis with that of the pump and imaging optics. **c.** The microcavity is formed by dielectric Bragg reflector (DBR) mirrors, comprising a exemplary structured mirror on the right (imaging facet) and a planar unstructured mirror on the left (pumping facet), and is filled with a dye solution of refractive index n_d. The dye filled cavity is pumped at normal incidence relative to the mirror surface, i.e with an angle of 0 $^\circ$ to the optical axis, and fluorescence is collected using a 20× objective with a numerical aperture of 0.42.

surface roughness of 0.5 Å, which were subsequently coated with a distributed Bragg reflector (DBR) stack composed of dielectric materials provided by *Laseroptik GmbH* [2].

The DBR mirrors were designed to exhibit high reflectivity at 580 nm, corresponding to the targeted photon condensate wavelength, while maintaining low reflectivity at the pump

[2] The mirror substrates have a diameter of 2" and a thickness of 6 mm. However, due to their bulkiness, the mirrors were diced into segments of 5 mm × 5 mm × 6 mm following DBR coating.

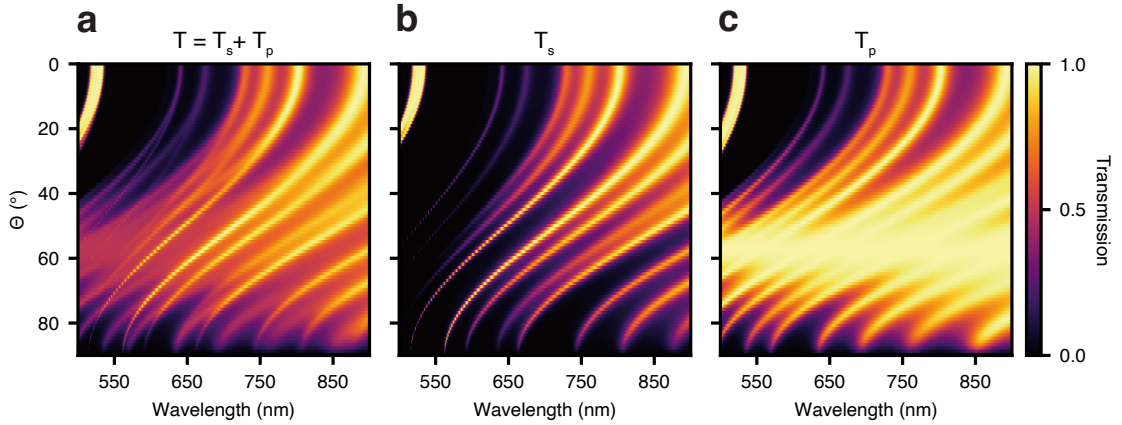

Figure 3.2: Calculated transmission profile of the cavity mirror as a function of wavelength and angle of incidence. **a.** The transmission profile was calculated as the average of the transmissions for s- and p-polarised light, which are presented in **b** and **c**, respectively.

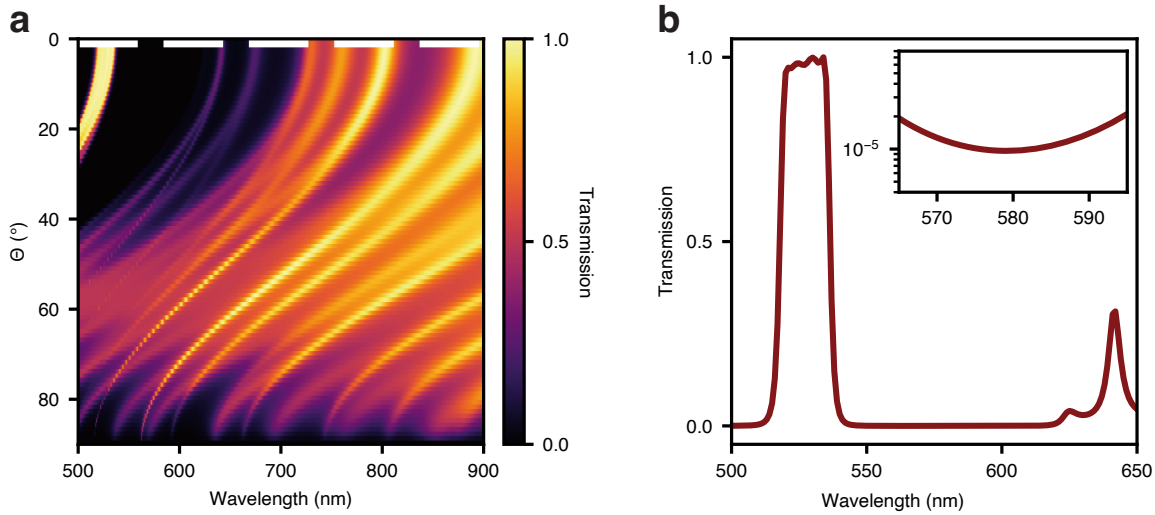

Figure 3.3: **a.** The calculated total transmission profile of the cavity mirror is shown as a function of the wavelength at normal incidence (0°), marked by a white dashed line. **b.** The mirror transmission in the region of interest for the photon gas and the pump wavelength at 532 nm is extracted from the trace at 0° in **a**. The inset displays the transmission profile on a logarithmic scale around the photon gas wavelength, between 570 nm and 580 nm.

wavelength of 532 nm. In earlier dye microcavity photon gas designs, such a differential reflectivity is achieved by introducing a pump beam at an incidence angle of 43° for a specific linear polarisation, owing to the angle-dependent reflectivity of DBR coatings. However, this approach introduces two main drawbacks: first, the spatial profile of the pump beam cannot be modified without introducing optical aberrations due to the high incidence angle; and second, the pump polarisation is restricted to a single linear orientation.

These limitations were addressed through the implementation of a novel Bragg mirror

design, which provides low reflectivity for the pump wavelength even at normal incidence, while preserving high reflectivity across the photon condensate wavelength range. The computed transmission matrix of the DBR mirror as a function of wavelength and incidence angle is presented in Figure 3.2. At 532 nm and 0° incidence, increased transmission is observed for both pump polarisations. In contrast, for the thermalised photon gas spectrum spanning 560 to 580 nm, the transmission remains low, reaching a minimum value of 10^{-5} at 580 nm, as shown in Figure 3.3.

Cavity lifetime

The cavity photon lifetime can be compared to the absorption and emission time scales of the dye molecules, which are crucial for establishing thermalisation. The finesse of an empty cavity with mirror reflectivity $R = 0.99998$ is given by [63]

$$\mathcal{F} = \frac{\pi\sqrt{R}}{1-R} = 1.57 \times 10^5 \, . \tag{3.1}$$

The round-trip time, defined as the time required for a photon to traverse twice the optical path length L of the cavity at the speed of light in vacuum c, is given by

$$t_{\mathrm{rt}} = \frac{2L}{c} \, . \tag{3.2}$$

For longitudinal mode number $q \leq 10$ at a cutoff wavelength of $\lambda_c = 580$ nm, the optical path length inside the cavity is approximately

$$L \leq \frac{q\lambda_c}{2} \approx 2.9 \, \mu\mathrm{m} \, ,$$

yielding a round-trip time of

$$t_{\mathrm{rt}} \approx 10 \, \mathrm{fs} \, . \tag{3.3}$$

The photon storage time, or cavity lifetime, is then determined as

$$\tau_{\mathrm{c}} = \frac{\mathcal{F} t_{\mathrm{rt}}}{2\pi} = 250 \, \mathrm{ps} \, . \tag{3.4}$$

This lifetime is significantly longer than the typical absorption–emission timescale of the dye molecules, which is on the order of a few picoseconds for a concentration of 1 mmol L^{-1} [27]. Therefore, photons remain within the cavity long enough to undergo repeated absorption and re-emission processes, enabling thermalisation of the photons via the dye medium.

3.1.2 Cavity alignment and control

An optical cavity with micrometre-scale spacing and two independently mounted mirrors offers both versatility and significant experimental challenges. This configuration, commonly referred to as an open cavity design, provides the advantage of independent control over critical cavity parameters. However, alignment becomes increasingly demanding as the mirror

separation is reduced to only a few micrometres. Care must be taken to ensure that the mirrors, as well as any structures present on them (such as polymer structures), do not come into contact with the opposing cavity mirror during the tuning of the longitudinal cavity length or the adjustment of the mirror tilt.

To address these challenges, a robust and tunable cavity assembly was constructed, incorporating the necessary degrees of freedom as outlined below.

The tilt of each mirror is independently controlled. The mirrors are mounted on separate mirror holders, with the left mirror holder equipped with a piezo-actuated micrometre screw (piezo mike). This mechanism provides precision tilt control with a step size of 20 nm, enabling the introduction or compensation of a linear gradient across the cavity by modifying the cavity length along the transverse plane. This feature is particularly useful for eliminating unwanted gradients induced by nano-structuring on the mirror surface.

The mirrors must be positioned sufficiently close, on the order of micrometres, such that the longitudinal mode number of the optical field within the cavity, q, corresponding to a cutoff wavelength of $\lambda_c = 580$ nm, remains sufficiently small. As a result, the free spectral range becomes large, and the majority of fluorescence is constrained to the same longitudinal mode. Under these conditions, the photon gas remains effectively two-dimensional, which also ensures a non-zero rest energy for the photon gas [27, 61]. In this work, the short mirror spacing is realised by mounting the left mirror holder on a piezoelectric translation stage capable of sub-100 nm precision. The cavity is typically operated at longitudinal mode numbers $q \leq 10$, corresponding to a mirror separation of $D_0 = q\lambda_c/(2n_d) \leq 2$ µm. Under these conditions, the resulting free spectral range exceeds 64 nm, which is considered sufficiently large. The piezoelectric stage also facilitates long-term drift compensation by monitoring the cutoff wavelength using a spectrometer, which serves as a reference signal for tuning the cavity length.

The structured right mirror contains multiple regions of interest featuring polymer structures with varied parameters. To access these regions across the mirror surface, the cavity mirrors are mounted on a three-axis translation stage [3], allowing precise translation of the mirror with a resolution of 50 µm/revolution via a micrometre screw.

The entire cavity assembly is positioned at the confocal point of both the pump and imaging optics by mounting it on a custom-built, suspended three-axis translation breadboard (see Figure 3.1). This configuration serves two main purposes: (1) it enables precise positioning of the cavity relative to the pump and imaging optics, thereby minimising aberrations; and (2) the suspended breadboard, supported by springs integrated into a vertical translation stage, passively reduces vibrations and suppresses jitter in the cavity cutoff wavelength. This passive stabilisation is particularly beneficial in experiments involving variable intra-cavity photon numbers, where locking the cavity via the cutoff wavelength becomes challenging due to weak signal intensities.

[3] Thorlabs three-axis microblocks

3.2 Pumping the dye microcavity

In optical microcavity experiment platforms, a mechanism is required to inject photons into the cavity. Depending on the thermalisation medium, this injection can be achieved optically or electrically, as demonstrated in semiconductor-based photon Bose–Einstein condensation platforms [73]. In the present work, where Rhodamine 6G dye molecules serve as the thermalisation medium, optical excitation is used to introduce photons into the dye-filled microcavity.

Rhodamine 6G exhibits a broad absorption spectrum ranging from 425 nm to 585 nm, enabling pumping the dye at shorter wavelength than the photon gas at thermal equilibrium. The photons generated by emission from dye molecules within the dye-filled microcavity subsequently undergo thermalisation, redistributing their energy via repeated absorption and re-emission processes [27, 61]. This results in the formation of a thermalised photon gas, typically within the spectral range of 560 nm to 580 nm, depending on the depth of the confining potential.

A commercially available, frequency-doubled laser operating at 532 nm was here employed as the pump source. The system, provided by *SpectraPhysics* (*Millennia EV10S*), delivers up to 10 W of optical power, offering sufficient intensity for effective pumping the dye.

To prevent photobleaching of the dye and to maintain a steady-state condition over a finite time period, temporal shaping of the pump beam is required. In order to confine dye pumping to the vicinity of the microstructure and suppress the excitation of unconfined modes (free space modes), spatial beam shaping is employed, as described in Sections 3.2.1 and 3.2.2, respectively. The full dye microcavity pumping setup is illustrated in Figure 3.4.

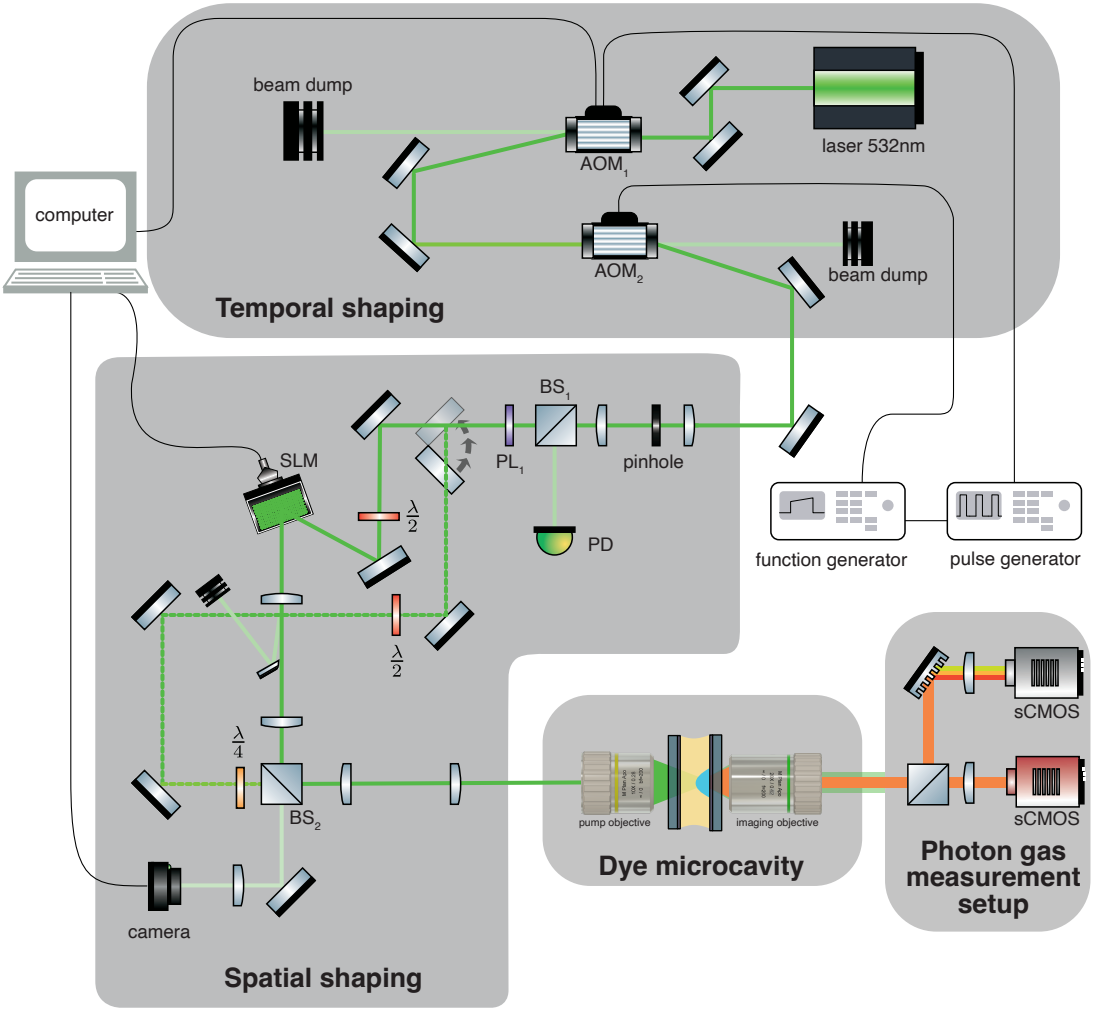

Figure 3.4: Dye microcavity pumping setup, subdivided into temporal and spatial shaping modules. Additional essential components, such as the dye-filled microcavity and photon gas measurement setup, are also included for completeness. The polarised pump laser is temporally modulated using AOM_1 and AOM_2, spatially cleaned using a telescope with a pinhole in the focal plane, and subsequently split into two optical paths by a flip mirror. One path enables spatial beam modulation via a spatial light modulator (SLM), while the other provides a standard Gaussian beam profile for pumping. The polarisation state is adjusted using wave plates positioned at designated locations. The beam profile is monitored with a camera, and final focusing into the cavity is achieved using a 10× magnification objective. Some of the graphical components employed have been sourced from an online graphics component library [94].

3.2.1 Temporal shaping

Continuous, steady state operation of a photon gas, achieved by balancing the pump with cavity losses, would be ideal. However, the dye molecules used here for thermalising the photons undergo photobleaching under continuous-wave (CW) light exposure [95].

Photobleaching is minimised by limiting the active pumping duration, or the steady state period, to between 200 ns and 500 ns, followed by a dark interval ranging from 5 ms to 20 ms. Timing control is achieved via a pulse generator that provides periodic TTL signal with adjustable pulse widths and delays. To temporally modulate the pump light into quasi-CW pulses, an acousto optic modulator (AOM_1) is employed. AOM_1 deflects the incident 532 nm pump beam into the first-order diffraction path with approximately 85% efficiency, with the temporal pulse duration defined by the input TTL signal. Additionally, an analogue input to AOM_1 permits fine control of the first-order diffraction intensity, and thereby the pump power, as shown in Figure 3.4.

Despite the quasi-CW operation, dye molecules may still undergo transient photobleaching by being excited into triplet dark states within the 500 ns illumination period. Although this effect is relatively minor, it causes deviation from the ideal steady-state photon gas conditions. To compensate for this transient response, the first-order beam from AOM_1 is directed through a second acousto optic modulator (AOM_2). AOM_2 is used to apply a steady linear ramp to the diffraction efficiency over the pulse duration, increasing from 90% to 100%, controlled via an arbitrary function generator. This helps to offset the temporary drop in dye efficiency.

The temporally shaped pump beam is monitored in real time using a photodiode (PD), ensuring consistent pulse shaping across repeated cycles.

3.2.2 Spatial shaping

To ensure optical pumping of dye molecules in the region of the microstructure, spatial shaping of the pump is carried out using a dedicated optical setup, as illustrated in Figure 3.4.

The first-order beam from the AOMs typically exhibits a non-Gaussian and irregular spatial profile, which necessitates beam cleaning. This is accomplished using a spatial filter comprising a pinhole placed at the focal point of a telescope configuration. The result is a collimated Gaussian beam with a full-width at half-maximum (FWHM) of approximately 3.4 mm (see Figure 3.5) [4]. Following spatial filtering, a linear polarisation state of the pump beam is achieved using a polariser PL_1 (see Figure 3.4), which is required for the subsequent modulation steps. Depending on the experimental requirements, both the spatial profile and the polarisation of the pump beam must be adjusted. To enable this flexibility, the beam is split into two paths via a flip mirror: one for standard Gaussian-profile excitation and the other for spatial modulation using a Spatial Light Modulator (SLM), as illustrated in Figure 3.4.

For experiments involving small and isotropic confining potentials, the Gaussian pump profile is sufficient and yields a nearly flat chemical potential. This path also permits full control over the pump beam's polarisation using a combination of $\lambda/2$ and $\lambda/4$ wave plates. Since the cavity mirrors exhibit high transmission at 532 nm for all polarisation states at normal

[4] A small deviation from the true ideal Gaussian shape is attributed to the aperture and residual interference effects arising from the camera window and sensor surface.

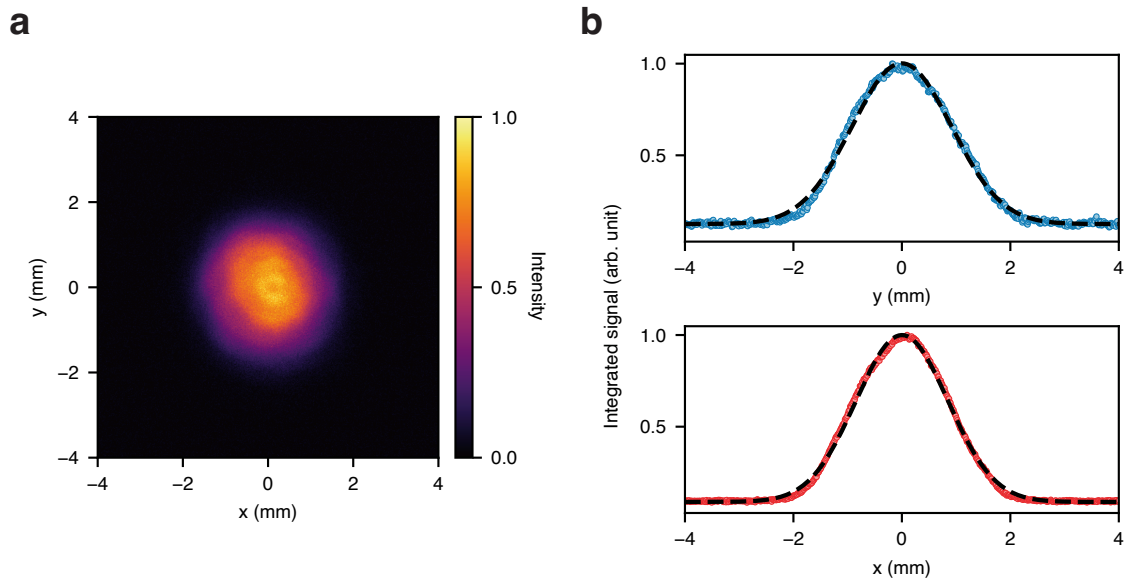

Figure 3.5: **a.** The spatial profile of the pump light is shown after spatial filtering with a pinhole in the focal plane of the telescope, resulting in a collimated Gaussian beam. **b.** The integrated intensity profiles along the x and y directions are plotted, along with Gaussian fits. The extracted full width at half maximum (FWHM) is approximately 3.4 mm.

incidence (see Figure 3.2), the polarisation degree of freedom can be fully exploited [96, 97].

For more complex spatial modulation, a phase-only, reflective, liquid-crystal Spatial Light Modulator (*PLUTO-2.1-VIS-130* by the supplier *HOLOEYE Photonics AG*) is employed, which is positioned at the Fourier plane of the pump objective. This SLM is selected over Digital Micromirror Devices (DMDs) owing to its higher modulation efficiency. Additionally, the dielectric-coated reflective backplane of the SLM allows for high-power operation (up to several tens of watts CW at 532 nm), as it enhances reflectivity while minimising absorption.

The SLM imprints a phase pattern onto the incident beam in the Fourier plane. Upon interference in the image plane, this yields the desired spatially modulated intensity profile. The required phase pattern is calculated using the Gerchberg–Saxton (GS) algorithm [98–100], implemented via software provided by the supplier *HOLOEYE Photonics AG*.

The modulation efficiency is determined by three main factors: (1) the spatial overlap between the incident and modulated optical fields in the Fourier plane, (2) the fill factor of the SLM, specified as 93%, that is, the region of the liquid-crystal display covered by the pixels [5], and (3) the inherent modulation efficiency of the SLM, which is typically below 99%. As a result, a portion of the pump beam remains unmodulated and co-propagates with the shaped beam.

To spatially separate the modulated and unmodulated components, a blazed grating phase mask is added to the desired modulation. This results in diffraction of the modulated

[5] Light incident on the gaps between the pixels is simply reflected without modulation. In this configuration, 7% of the total surface area of the SLM is rendered unusable.

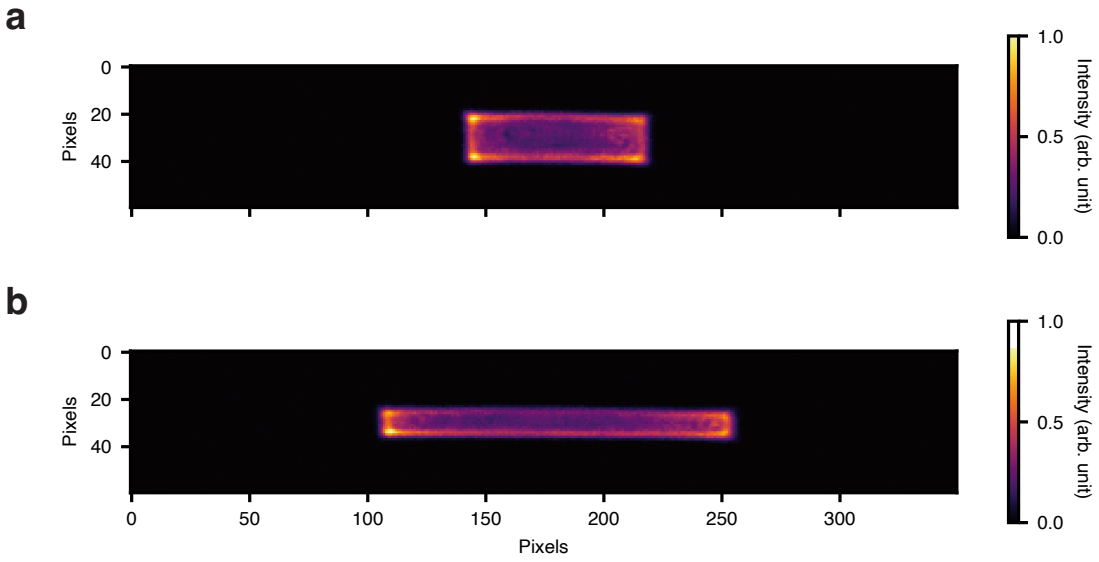

Figure 3.6: An exemplary spatially modulated pump beam is shown, generated using the spatial light modulator (SLM). The beam can be shaped into rectangular profiles with varying aspect ratios, as depicted exemplarily in panels **a** and **b**.

component into the $+1^{st}$ order, while the unmodulated light remains in the 0^{th} order. By adjusting the incidence angle of the pump beam on the SLM, the 0^{th} order can be directed away and blocked using a D-shaped mirror placed in the image plane, as illustrated in Figure 3.4.

The efficiency of SLM modulation is also sensitive to the pump beam's polarisation relative to the liquid-crystal alignment. Therefore, a half-wave plate is introduced before the SLM to tune the incident pump beam's polarisation for maximum modulation contrast.

To monitor the modulated pump beam, a non-polarising beam splitter (BS_2, 90:10 reflectance to transmittance) diverts 10% of the beam onto a *Thorlabs Zelux* camera. Exemplary spatial profiles of the modulated beam are shown in Figure 3.6, where rectangular patterns with distinct aspect ratios are presented. Furthermore, the SLM software supports aberration correction using Zernike polynomial functions to refine the final beam shape [6].

Thus, using this optical arrangement, both the temporal and spatial properties of the pump light are precisely controlled. The structured pump beam is coupled into the cavity using a long working distance, apochromatic, 10× magnification objective (numerical aperture 0.28, infinity-corrected, by *Mitutoyo Deutschland GmbH*).

[6] The intensity maxima in the rectangular intensity patterns are typically located at the edges. This effect can be mitigated by employing an asymmetric cylindrical zone plate phase mask, with additional aberration correction applied if required. The shape is optimised depending on the structure being pumped.

3.3 Experimental methods for photon gas measurements

Insights into the physics of the dye microcavity photon gas can be obtained by measuring its thermodynamic quantities, such as the total photon number, energy distribution, and spatial distribution. These quantities are probed non-destructively by detecting the light emitted from the cavity, often referred to as cavity fluorescence. Since the photons that leak through the cavity mirrors directly reflect the intra-cavity photon distribution, this emission provides a reliable mapping of the internal state of the photon gas.

The measurement system is divided into two main branches: one for imaging the density distribution in both real and momentum space, and the other for performing spectroscopy, also in both real and momentum spaces, as illustrated in Figure 3.7. Due to the high reflectivity of the cavity mirrors and the relatively low intra-cavity photon number, only a small fraction of photons escape the cavity. For a steady-state intra-cavity photon number of approximately 1000, the out-coupled optical power through one of the mirrors is typically less than half a picowatt per pulse. As such, the detection setup is optimised for low signal levels. To minimise background noise, the entire setup is enclosed in a light-tight housing to shield it from stray ambient light.

Prior to entering either the imaging or spectroscopic branches, the leakage photons must be efficiently collected and separated from residual stray light. This is achieved using a long-working-distance, apochromatic objective (numerical aperture 0.42, 20× magnification, infinity-corrected, by *Mitutoyo Deutschland GmbH*) to collect the cavity fluorescence. The collected light, after a 20 cm focal length achromatic tube lens, passed through a set of optical filters: a notch filter to suppress the residual pump light at 532 nm (F_1) and a short-pass filter to block wavelengths beyond 600 nm (F_2), which may arise from the alignment laser (e.g. HeNe) or other spurious sources.

Subsequently, the filtered light is imaged onto a variable rectangular aperture placed in the image plane. This aperture is used to block stray light and transmit only light originating from within the photon gas potential. It is particularly useful in rejecting light from unconfined plane-wave modes, especially in the presence of elongated or asymmetric finite-depth potentials.

The resulting cavity fluorescence is then relayed through a linear polariser (PL_2), which enables measurements to be performed within a selected polarisation subspace. This capability is essential for exploring polarisation-dependent effects in the photon gas [97]. Finally, a non-polarising beam splitter (BS_3) divides the optical path into two branches: one directed towards a spectrometer, and the other towards an density distribution setup for either real or momentum space imaging, as depicted in Figure 3.7.

3.3.1 Spatial and momentum space imaging

The density distribution measurement setup, shown in Figure 3.7, is designed to allow the probing of the spatial and momentum-space density distributions of the photon gas confined within a given potential. This configuration serves as a complementary tool to the spectroscopic setup, allowing qualitative cross-verification of the dispersion shape where applicable. In

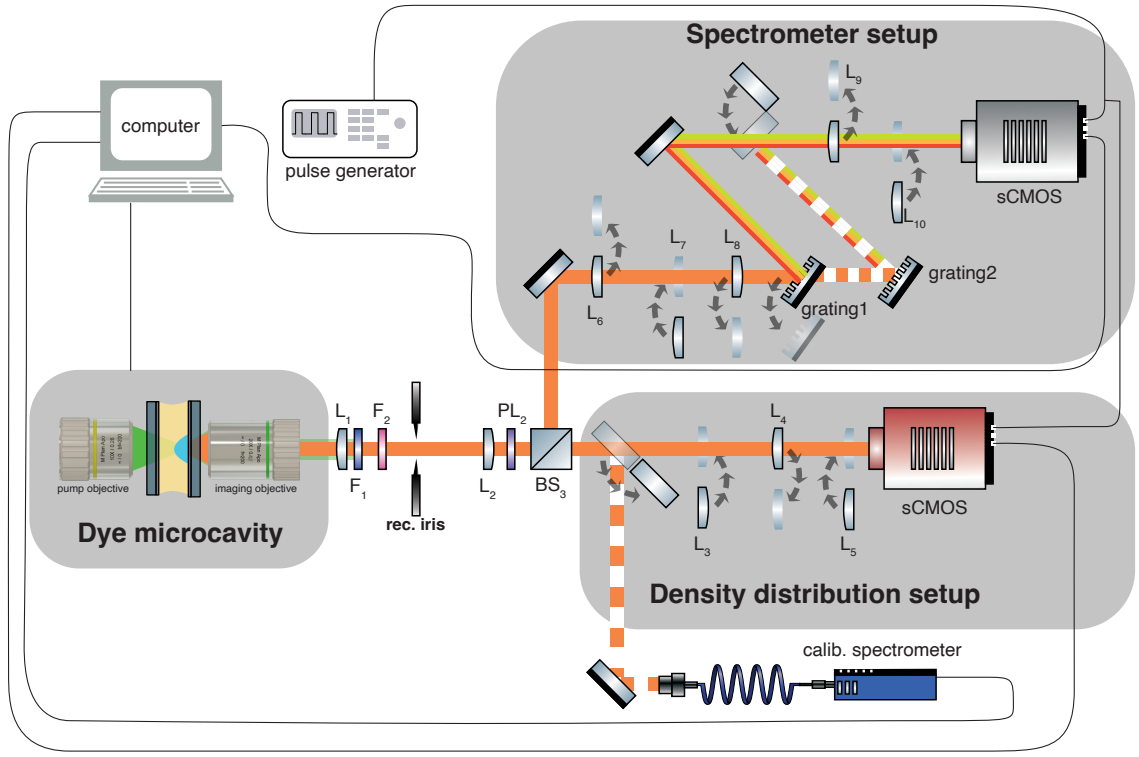

Figure 3.7: Dye microcavity emission detection setup. The collected cavity fluorescence is divided into two optical paths: one directed to the spatial and momentum-space imaging system (density distribution setup), and the other to the spectroscopy setup. The current configuration is shown operating in the real-space domain, which can be switched to momentum space by adjusting the relevant optical components, as indicated by the arrows. Further details on the optical elements used are provided in Appendix A. Some of the graphical components employed have been sourced from an online graphics component library [94].

this work, the investigated potentials are often narrow, small, or both. Consequently, the spatial resolution limit is reached for small or elongated potentials, or for potentials with steep boundaries, and the corresponding momentum-space distribution becomes proportionally broad, resulting in signal-to-noise constraints. Despite this, the imaging setup plays an important role in cavity alignment and qualitative verification, even though most quantitative results are inferred from spectroscopic data.

In its simplest form, the spatial imaging setup functions as a microscope. It is essential for aligning the cavity mirrors such that a specific structured region on the patterned mirror is brought into the focal plane of the imaging objective. Similarly, the alignment of the pump beam is performed using this imaging path [7].

The transmitted cavity fluorescence from the beam splitter is imaged directly onto a

[7] This is achieved by observing the fluorescence location and guiding it using the spatial light modulator (SLM), in conjunction with cross-checking the spectrometer camera. The resulting signal provides a distinct signature of the potential, which differs from that of the free-space continuum modes.

sCMOS camera (*Kiralux 12.3 MP Monochrome CMOS Camera*) using an achromatic lens with a focal length of 30 cm. This configuration yields an effective magnification of 30×. The microscope resolution, estimated using the Rayleigh criterion $0.61\lambda/\mathrm{NA}$ at the photon condensate wavelength $\lambda = 580$ nm, is approximately 0.84 µm. Combined with the high pixel density of the camera, this setup allows imaging near the diffraction-limited spatial resolution.

Momentum-space imaging is achieved by Fourier transforming the optical field. For light, this transformation is performed by a lens, which maps the propagation angle of a wavevector $\vec{k}$ (relative to the optical axis) to a position in its focal plane [101]. Thus, the angular momentum distribution of the photon gas can be directly accessed by measuring the intensity distribution in the focal plane. To perform momentum-space imaging, the back focal plane of the imaging objective must be relayed onto the same sCMOS sensor. A set of relay lenses (L_1 and L_2) preserves the back focal plane of the objective, while lenses L_3 and L_5 (with focal lengths of 20 cm and 10 cm, respectively) image this plane onto the camera. To maintain confocality, these lens assemblies are mounted on flip mounts, allowing switching between spatial and momentum-space imaging modes.

Pixel to momentum vector calibration

The mapping between pixels on the sCMOS camera and the transverse momentum vector components of the photons from the microcavity emission is established using ABCD matrix ray tracing [101]. Given the confocal arrangement of the optical system, ray transfer matrices are used to propagate rays from the cavity output to the detector.

Let the angle at which a ray exits the cavity mirror surface (comprising the DBR and substrate) be denoted by θ_i relative to the optical axis, at a position x_i. After propagating through the optical system, the ray illuminates a position x_f on the camera sensor, corresponding to an angle θ_f at the output plane. The transformation between these vectors can be expressed as:

$$\begin{bmatrix} x_i \\ \theta_i \end{bmatrix} = \underbrace{\begin{bmatrix} A & B \\ C & D \end{bmatrix}}_{M_{\mathrm{opt}}} \begin{bmatrix} x_f \\ \theta_f \end{bmatrix}$$

where M_{opt} is the total ABCD matrix for the optical path between the external surface of the cavity and the sCMOS sensor.

As light exits a medium with refractive index n_d (the dye solution) into air, Snell's law relates the internal angle θ to the external angle θ_i:

$$\theta = \arcsin\left(\frac{\sin\theta_i}{n_d}\right) . \tag{3.5}$$

Using this angle, the transverse component of the photon's wavevector in the x-direction is calculated as:

$$k_x = k_z \tan(-\theta) , \tag{3.6}$$

where k_z is the longitudinal wavevector component, defined in Equation 2.1. The y-component of the wavevector, k_y, is similarly determined from the pixel displacement y_f

along the y-axis of the sensor.

This calibration method assumes that the angular spread of the rays remains within the paraxial regime. With a numerical aperture of 0.42 for the imaging objective, this assumption is of course marginal. However, the potentials investigated in this work are shallow enough that the emission angles θ_i remain well below this upper limit (i.e. $\theta_i \ll 0.42$). Therefore, the ABCD matrix formalism is deemed valid for accurate momentum calibration in this regime.

3.3.2 Spectrally resolving the photon gas distribution

A thermodynamic characterisation of the photon gas requires direct access to its energy distribution. While spatial and momentum-space density distributions can offer some insights, they are inherently limited by resolution constraints. Momentum-space imaging may provide a more accurate proxy for energy distribution in specific cases, such as box potentials, where the spatial overlap of momentum eigenstates is minimal [28]. In such configurations, the momentum distribution approximates the energy distribution well. However, this correspondence does not generally hold for other potentials of interest, such as harmonic oscillator traps, where real-space Hermite–Gaussian eigenfunctions Fourier transform into rescaled Hermite–Gaussian functions in momentum space, resulting in significant mode overlap.

Therefore, direct spectroscopic measurements are necessary not only to resolve the energy distribution of the photon gas but also to obtain its absolute energy scale [8].

Spectroscopy of the cavity fluorescence is performed using two custom-built spectrometers. The first, a real-space spectrometer, is optimised for signal-to-noise ratio and is used for extracting the energy distribution. The second, sharing the same back-illuminated scientific CMOS camera, is configured to measure the photon dispersion relation. Most of the potentials studied in this work have maximum widths smaller than 50 µm. In such cases, the real-space spectrometer provides a higher signal-to-noise ratio, since the signal remains spatially concentrated. Conversely, in momentum space, the same signal is distributed over a broader area, making this configuration better suited for resolving the shape of the dispersion relation rather than the energy distribution.

Switching between the two spectrometers is achieved by introducing or removing the appropriately aligned lenses and gratings into the optical path using a flip-mounts, as shown in Figure 3.7.

Both spectrometers employ blazed reflective diffraction gratings with 1200 grooves/mm as the dispersion element. The dispersed spectrum is imaged onto a back-illuminated sCMOS camera (*Andor Marana 4.2B-11*), which provides approximately 95% quantum efficiency and active cooling. The detector consists of 2048 pixels (each 11 µm wide) along the dispersion axis, enabling high spectral resolution. Calibration of the dispersion axis is performed using a commercial spectrometer. The real-space configuration provides a spectral range of 62.5 nm and a resolution better than 0.3 nm. In momentum-space configuration, the spectral range extends to 74.4 nm with a maximum resolution of 1 nm.

To preserve spatial mode information and maximise signal collection in low-light regimes, no entrance slit is employed in either configuration. While this slit-less design results in a

[8] That is, the true energy of the photon, hc/λ_c, can be obtained directly from the measured wavelength.

reduction of spectral resolution, it enables direct measurement of mode shapes and improves signal-to-noise ratio, an essential requirement for experiments involving low intra-cavity photon numbers. Although alternative methods, such as tomographic spectroscopy [102, 103], are available to simultaneously extract both mode shape and spectral information, these techniques were not feasible for use in this work due to the extremely low photon numbers, which limit their practical sensitivity.

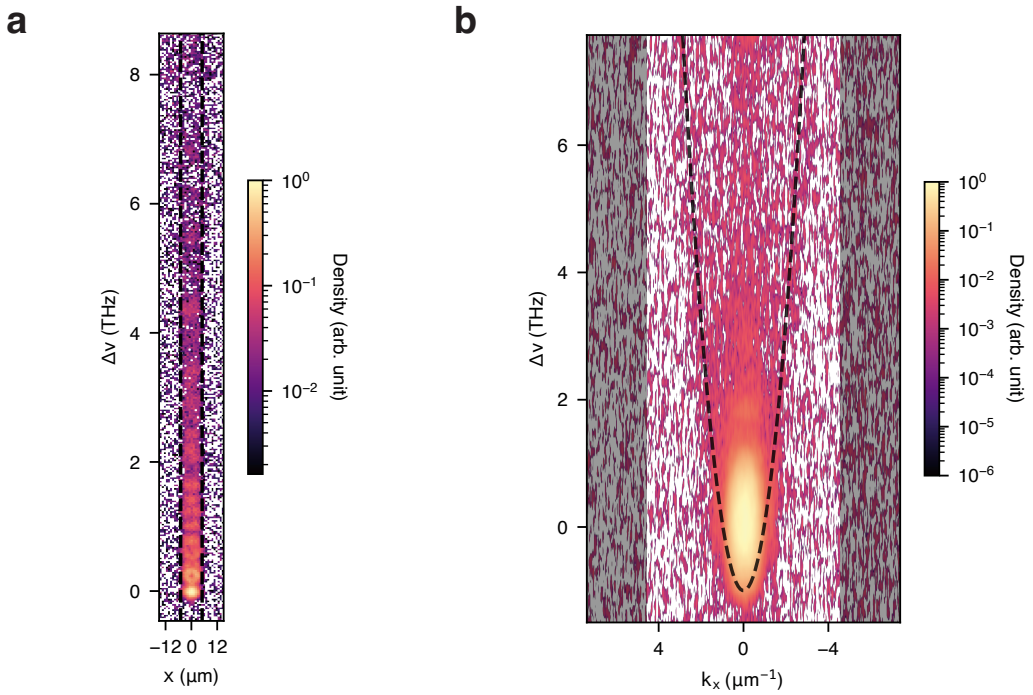

Figure 3.8: Exemplary spectral dispersion of a 10×10 µm box potential in real and momentum space in the quantum degenerate limit. **a.** The expected spatial bounds of the box potential are indicated by dashed black lines at -5 µm and 5 µm overlaid on the raw real-space spectrograph. **b.** The raw momentum-space spectrum of the same box potential is shown, with the expected parabolic dispersion marked by an overlaid dashed black curve. The regions shaded in grey denote areas beyond the numerical aperture (NA) of the detection setup.

To illustrate the differences in the results obtained using the two spectrometers, exemplary spectra for a photon gas confined in a 10 µm$\times$10 µm box potential are shown in Figure 3.8. As expected, the real-space spectrum exhibits a uniform mode size across all energies, consistent with the homogeneous spatial density of the box potential. In contrast, the momentum-space spectrum shows an energy-dependent broadening of the modes, following a parabolic dispersion relation $E \propto k^2$ [28]. Although the resolution in the momentum-space spectrometer is limited due to its slit-less configuration, the overall dispersion profile remains consistent with theoretical expectations. A detailed analysis of results obtained with this potential is presented in Chapter 6.

Photon number estimation

The total intra-cavity photon number, denoted by N, is used as the primary experimental tuning parameter in this work. An experimental estimate of N is obtained by calibrating the detected counts on the sCMOS sensor of the real-space spectrometer against the actual intra-cavity photon number. This calibration accounts for mirror transmission losses and the duration of the steady-state emission. It is performed using a broadband tunable source, such as a dye laser.

Depending on the potential landscape, N can be extremely low, occasionally on the order of a few tens of photons, resulting in a very low signal-to-noise ratio. To improve this, the camera integration time is configured to accumulate cavity fluorescence over many identical experimental realisations. This averaging enhances the signal without altering the underlying photon statistics.

Care is taken to ensure that the cavity cutoff remains stable during the integration period, as fluctuations in cavity length can degrade the spectral resolution, particularly under slit-less conditions. Data acquisition begins only after the cavity length has passively stabilised and mechanical drifts have been minimised. Furthermore, the integration duration is accounted for when converting detected counts to photon numbers.

It should be noted that systematic uncertainties in the calibration factor may introduce a shift in slope of the counts to photons calibration curve. However, as shown in subsequent chapters, the calibration constant can be eliminated when analysing appropriate photon gas observables for which the dependence on N cancels out. Consequently, the measurements remain internally consistent and precise, even if the absolute accuracy is subject to a fixed uncertainty.

CHAPTER 4

Nano-structuring potentials for photon gases

In this chapter, a novel fabrication method for realising high-curvature potentials necessary for experiments on the dimensional crossover of a photon gas in a dye microcavity is discussed. Currently, the established fabrication technologies for the dye microcavity platform yield feature sizes of approximately 3 µm, which is significantly larger than the photon condensate wavelength of around 580 nm, thereby inhibiting the fabrication of potentials with both high curvatures (corresponding to steep traps) and depths [31]. In other photon gas platforms, such as the erbium-ytterbium co-doped fibre (EYDF) cavity, potentials with both high curvatures and depths are achievable, but the dimensionality is restricted to one dimension [75, 104] [1], preventing experiments on observing a dimensional crossover of a photon gas.

As outlined in Section 2.1 of Chapter 2, the critical parameter in realising a potential for a dye microcavity photon gas is the longitudinal optical path length. To address this, the well-established additive fabrication technology of 3D printing polymer structures on the nanometre length scale using Direct Laser Writing (DLW) has been employed, a method that has been widely adopted across various research areas [33–44]. The stability of polymer in the dye solution under high intracavity power conditions is not straightforward to achieve; however, this challenge has been addressed and resolved in the referenced Master's thesis work [105]. Thus the adaptation of DLW technology for fabricating potentials in the dye microcavity platform is presented, together with a discussion of the unique challenges associated with 3D nano-printing on cavity mirrors and the corresponding solutions.

The chapter begins with a summary of the established methods for creating engineered potentials for the dye microcavity photon gas platform, employing the dispersion relation 2.6 (Section 4.1). In Section 4.2, the general working principles of the DLW experimental setup are discussed, followed by an examination of various configurations used in fabrication and the challenges associated with DLW fabrication on reflective cavity mirrors (Section 4.3). Finally, in Section 4.4, methods to overcome the challenges of printing on reflective mirrors and to achieve quasi-stepless polymer structures are presented.

[1] Access to the second dimension can be achieved if the fibre is multimode; however, tuning the dimensionality is not straightforward.

4.1 Arbitrary potentials for photon gas

The photon gas in a dye-filled microcavity is subjected to a confining potential generated by the transverse cavity length modulation term $d(\vec{r})/D_0$, as shown in equation 2.6, where the modulation refers not only to the physical distance between the cavity mirrors but also to the effective optical path length between them. This modulation may be implemented in three distinct ways, and the corresponding potential energy is therefore decomposed as expressed in Equation 2.1, which is reiterated here for convenience.

$$V(\vec{r}) \simeq \frac{m_{\text{eff}}c^2}{n_d^2}\frac{d(\vec{r})}{D_0} = \frac{m_{\text{eff}}c^2}{n_d^2}\left(\frac{\Delta d(\vec{r})}{D_0} + \frac{\Delta n(\vec{r})}{n_d} - \frac{n_s - n_d}{n_d}\frac{h(\vec{r})}{D_0}\right) \tag{4.1}$$

Firstly, the physical length of the cavity, $\Delta d(\vec{r})$, may be modified—for instance, by employing spherically curved mirrors with radii of curvature R_1 and R_2. This configuration yields an isotropic harmonic oscillator potential of the form

$$V(\vec{r}) = \frac{1}{2}m_{\text{eff}}\left(2\frac{c^2}{n_d^2}\frac{(R_1+R_2)/(R_1R_2)}{D_0}\right)r^2\,, \tag{4.2}$$

valid for $|\vec{r}| \ll D_0$, where the term in brackets represents the square of the angular trap frequency ω [27, 106].

More complex potential landscapes can be realised by locally altering the elevation of the mirror surface. Two well-established methods have been developed for this purpose. The first, known as the delamination method [31], involves the local elevation of a dielectric mirror stack (DBR) by depositing heat into an additional silicon layer. The second approach utilises focused ion beam (FIB) milling[107] where a subtractive approach is used by carving out the desired shape in the glass substrate followed by deposition of the dielectric mirror stack (DBR). These techniques have enabled the realisation of box-like potentials using delamination technique [28] and small traps for light using the FIB [108].

Secondly, modulation can also be achieved by locally varying the refractive index, thereby altering the effective optical path length. To date, the method implemented in dye-filled microcavities has exploited the second term in equation 4.1. This thermo-optic technique involves the use of a thermally sensitive polymer placed between the cavity mirrors. Upon the application of a heating laser, the polymer's refractive index undergoes a change $\Delta n(\vec{r})$, with the resulting potential determined by the spatial profile of the heating laser [109].

However, the creation of one-dimensional potentials required for the study of the dimensional crossover is necessitated by the use of a mirror structuring method with a resolution on the order of the photon gas wavelength. As delamination and the thermo-optic method, both heat-dependent techniques, typically achieve feature sizes of approximately 3µm, and although the FIB technique is, in principle, capable of carving deep, high-curvature structures into the glass substrate, the deposition of the DBR stack can only be performed after structuring. This adds significant complexity to the optimisation of the structuring process. Therefore, a novel method was developed in this work to realise deep, high-curvature potentials by exploiting the last term in Equation 4.1, where the local optical length is modulated by

printing polymer structures with varying height profiles using a Direct Laser Writing (DLW) system by the supplier Nanoscribe GmbH & Co. KG, as will be explained in the following sections. In collaboration with Dr. J. Schulz and Prof. Dr. G. von Freymann from RPTU Kaiserslautern-Landau, Kaiserslautern, Germany, the fabrication of the polymer structures was performed using such a Nanoscribe system. The fabrication system operation, as well as the pre- and post-processing of the cavity mirrors, were handled by them and will be discussed in detail later in this chapter. The iterative optimisation of the design parameters was carried out by the present author based on cavity fluorescence spectroscopy, in close coordination with J. Schulz.

4.2 Polymer direct laser writing

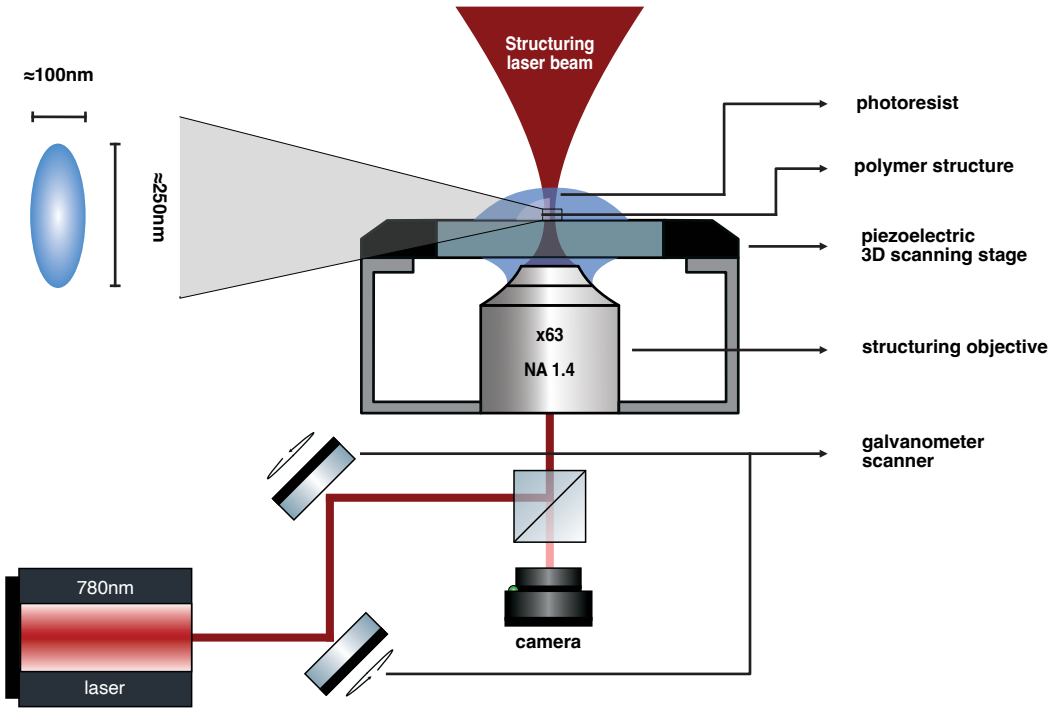

Figure 4.1: Simplified sketch of the polymer direct laser writing setup. The exposing light, provided by a laser with wavelength near 780 nm, is guided and controlled using two galvanometric scanners, and is focused onto the region of interest within the photoresist by a high numerical aperture (NA) 1.4 objective with 63× magnification. The substrate is held and positioned using piezoelectric scanning stage. The entire process is monitored with the aid of a camera placed in the imaging plane. The inset shows a voxel representing the region polymerised at the focal depth.

The polymer nanostructuring process operates by polymerising the monomers of the photoresist. The photoresist (IP-dip) requires exposure to light, typically in the UV range, to initiate the polymerisation process. To achieve small feature sizes, the exposing light must be focused using a high-NA, liquid-immersed objective (writing objective). However, two principal challenges must be overcome to achieve feature sizes below 1 µm: firstly, the

diffraction limit of the focused exposing light, and secondly, the tendency of the exposing light to polymerise the entire beam path within the photoresist.

To address both challenges, two-photon polymerisation is employed. Instead of UV light, infrared light (wavelength 780 nm; pulse duration 150 fs), at half the frequency of UV light, is used. This approach prevents polymerisation along the entire beam path, restricting the polymerised volume (voxel) to a size smaller than the diffraction limit. At the focus, sufficiently high intensity enables two-photon excitation of the photoresist, thereby initiating polymerisation.

In this work, the Nanoscribe Photonic Professional GT and Nanoscribe Quantum X systems by Nanoscribe GmbH & Co. KG were employed to 3D print nanostructures onto the mirror surface using two-photon polymerisation [38]. Feature sizes measuring 100 nm transversely and 250 nm longitudinally were realised. The polymer structures were printed in blocks by moving the mirror substrate with piezoelectric actuators, while the exposing light path was controlled using galvanometer scanners as shown in the Figure 4.1.

4.3 Direct laser writing configurations

Polymer nanostructuring using Direct Laser Writing (DLW) on the surface of materials such as glass can be performed in two main configurations: (a) immersion configuration and (b) dip-in configuration. The choice of DLW configuration depends on the transparency and thickness of the substrate. The advantages and limitations of the Direct Laser Writing (DLW) configurations for conventional cavity mirror substrates are first discussed, along with relevant solutions to these issues depending on the structures to be printed. In this work, both DLW configurations are employed. The immersion configuration, with certain modifications, is used for the structures presented in Chapter 5, whereas the dip-in configuration is utilised for flat-top structures, as discussed in Chapter 6.

A schematic sketch of the two configurations for the conventional cavity mirror is shown in Figure 4.2. The immersion configuration, also referred to as the conventional configuration, requires the substrate thickness to be much smaller than the working distance of the available writing objective so that the structuring laser beam (exposing light) can be focused through the substrate onto the opposite surface. As illustrated in Figure 4.2**a**, the 6 mm thick glass substrate of the cavity mirror is substantially larger than the working distance of the writing objective; thus, the immersion configuration here cannot be used for 3D printing the polymer structures.

In the dip-in configuration, the photoresist is placed between the writing objective and the surface of the material to be patterned, where it also serves as the immersion medium for the writing objective. This configuration permits the writing objective to approach very close to the surface of the cavity mirror (DBR), allowing for the fabrication of taller structures without being limited by the substrate thickness.

IP-DIP, with a refractive index of $n_s = 1.55$ [110], is employed both as the immersion medium for the writing objective and as the photoresist in the dip-in configuration, while immersion oil is employed as the immersion medium in the immersion configuration.

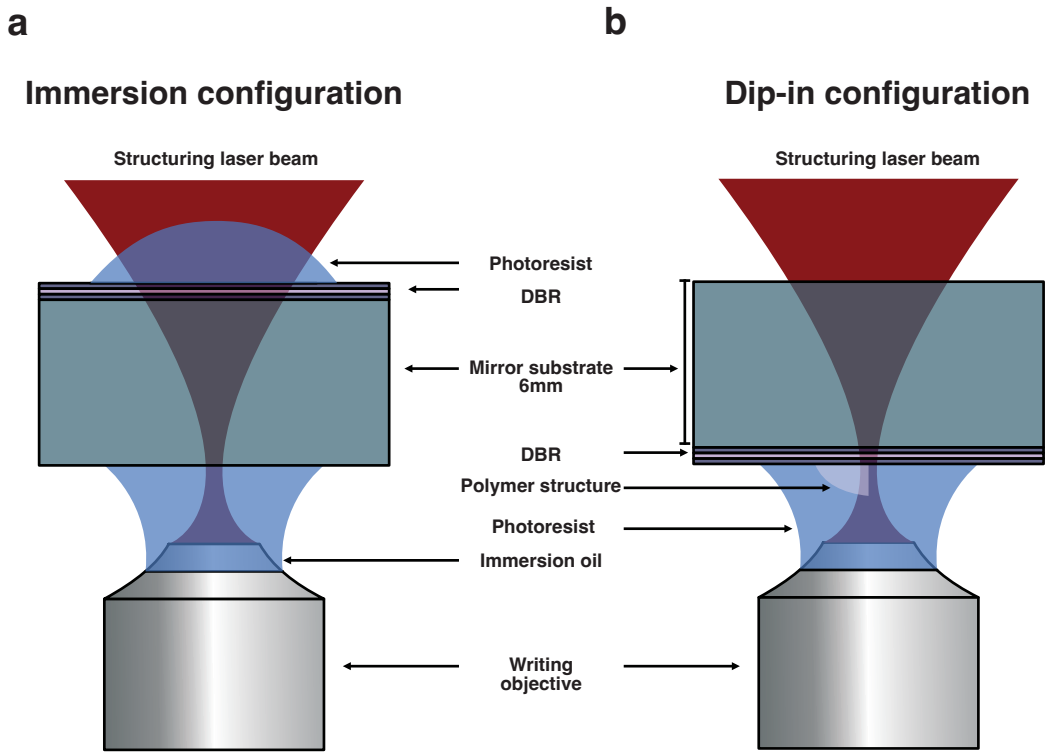

Figure 4.2: Direct laser writing (DLW) configuration for a conventional cavity mirror substrate. **a.** A schematic of the immersion configuration is shown, illustrating the limitation that structuring cannot be performed on the DBR surface due to the excessive substrate thickness (6 mm), which prevents the focus of the writing objective from reaching the region of interest. **b.** A schematic of the dip-in configuration is shown, in which the focus of the writing laser coincides with the region of interest, the DBR mirror surface, enabling polymer structuring.

The choice between the two DLW configurations for conventional cavity mirrors appeared to be straightforward, as the DBR stack is positioned on a 6 mm thick glass substrate. This arrangement precludes the use of the immersion configuration (see Figure 4.2**a**) for such mirrors with thick substrates. Consequently, the dip-in configuration, shown in Figure 4.2**b**, was initially tested.

To verify the fidelity of the structures fabricated using the dip-in configuration, an isotropic parabolic structure with a height profile

$$h(x, y) = h_0 - \zeta_x x^2 - \zeta_y y^2 \ , \tag{4.3}$$

was printed, where h_0 denotes the maximum height of the structure, and ζ_x and ζ_y represent the curvatures along the x and y directions, respectively. The height profile of the resulting structure was measured using Atomic Force Microscopy (AFM) [2] and is shown in Figure 4.3.

[2] A typical lateral resolution of approximately 20 nm and a vertical resolution of around 1 nm can be achieved using this technique.

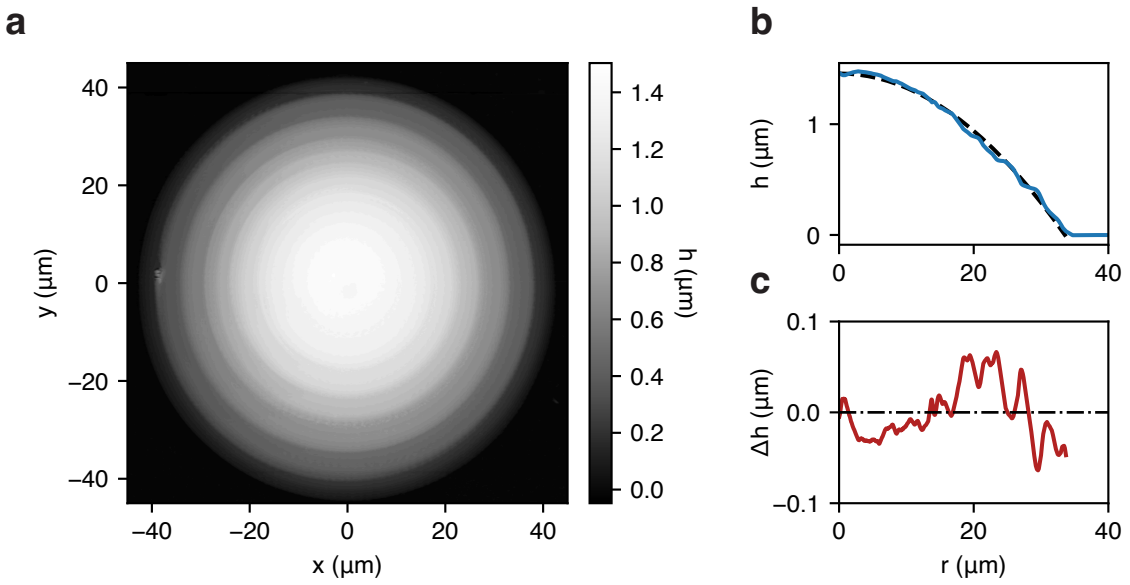

Figure 4.3: Measured height profile of the polymer structure with a parabolic height profile, fabricated using the dip-in configuration and characterised via atomic force microscopy (AFM). **a.** The transverse height profile is presented as a heat map, with the colour bar indicating height. **b.** The radial average of the height profile is shown, with the measured profile plotted as a solid blue curve and the ideal parabolic profile overlaid as a dashed black curve. **c.** The deviation of the measured radial average from the ideal parabolic shape is plotted as a solid red curve. Zero deviation is indicated by a dashed dotted black line.

The transverse height profile appears radially symmetric, with the height decreasing from the centre outwards as expected. However, step-like features are also observed, superimposed on the parabolic profile (see Figure 4.3**a**). To quantify this deviation, a radial average was performed on the measured two-dimensional height profile (Figure 4.3**a**), the radial average $h_m(r)$ (solid blue curve) was compared to the parabolic reference profile $h_e(r)$ (dashed black curve), which was obtained by fitting $h_m(r)$ with the maximum height and curvature treated as free parameters, as illustrated in Figure 4.3**b**.

The structure exhibits significant variation in curvature as a function of position. The deviation of the measured height profile $h_m(r)$ from the expected profile $h_e(r)$ is quantified as $\Delta h(r) = h_e(r) - h_m(r)$, shown in Figure 4.3**c**. Excluding deviations near the edge of the structure at approximately $r > 30$ µm, it is observed that substantial oscillations in the difference $\Delta h(r)$ occur within the bulk, attributable to the step-like features. These deviations in a microcavity are expected to alter the local density of states from that of an ideal harmonic oscillator, which is undesirable.

This deviation here may be attributed to an unwanted interference pattern generated by the exposing light in the dip-in configuration, as the mirrors possess finite reflectance at various incidence angles for the exposing light at 780 nm used to polymerise the photoresist. In Figure 4.4, the mirror reflectance at a wavelength of 780 nm as a function of incidence angle is presented. As the writing objective employed a high NA (1.4), the incidence angle

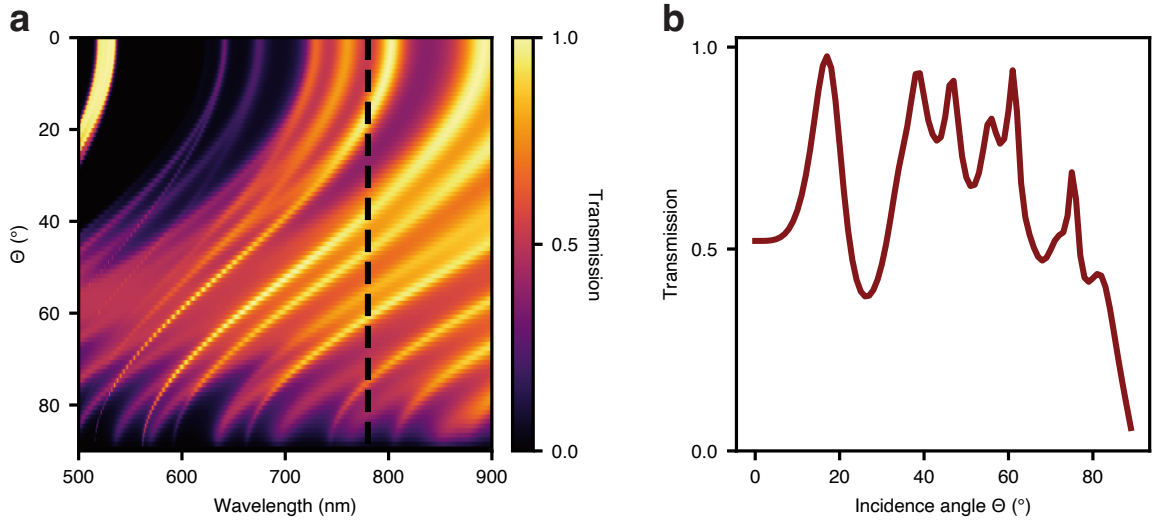

Figure 4.4: Transmission profile of the used DBR mirror around the direct laser writing (DLW) exposure wavelength. **a.** The DBR mirror transmission matrix is shown, with the exposure wavelength at 780 nm indicated by a dashed black line. **b.** The transmission at the exposure wavelength (780 nm) is plotted as a function of angle of incidence, corresponding to the numerical aperture (NA) of 1.4 for the writing objective in the immersion medium.

of the light ranged from 0 ° to a maximum of 70 °, and from Figure 4.4**b**, it is evident that substantial reflection of the exposing light occurred at the mirror surface. This reflection may have resulted in standing wave interference of the exposing light along the longitudinal (z) axis, creating alternating regions of high and low exposure in the photoresist, and thereby producing a polymer structure with step-like features.

4.4 Quasi-stepless nanostructuring

Step-like features that may arise from the interference pattern of the exposing light in the dip-in configuration can be suppressed by switching to the immersion configuration, as no standing waves are present in the polymerisation region, provided that the substrate thickness of the DBR mirror is reduced to below the working distance of the writing objective. To this end, the procedure illustrated in Figure 4.5 was employed to obtain quasi-stepless polymer nanostructures, as follows: the 6 mm thick substrate region of the mirror (referred to as the thick mirror) was ground, and polished to a thickness of approximately 100 µm. The resulting mirror flake (thin mirror) possessed a substrate thin enough for use in the immersion configuration, allowing the polymer nanostructuring to be performed and developed. However, the nano-structured thin mirror proved too fragile for use in the dye microcavity experimental setup. To provide mechanical stability, the structured thin mirror was bonded to a 5 mm thick glass substrate using an optically transparent adhesive. The adhesive was selected for its solubility in solvents such as acetone, enabling the thin mirror to be reused and restructured if necessary. Photographs of the mirror before and after this procedure are shown in Figure 4.5**b**.

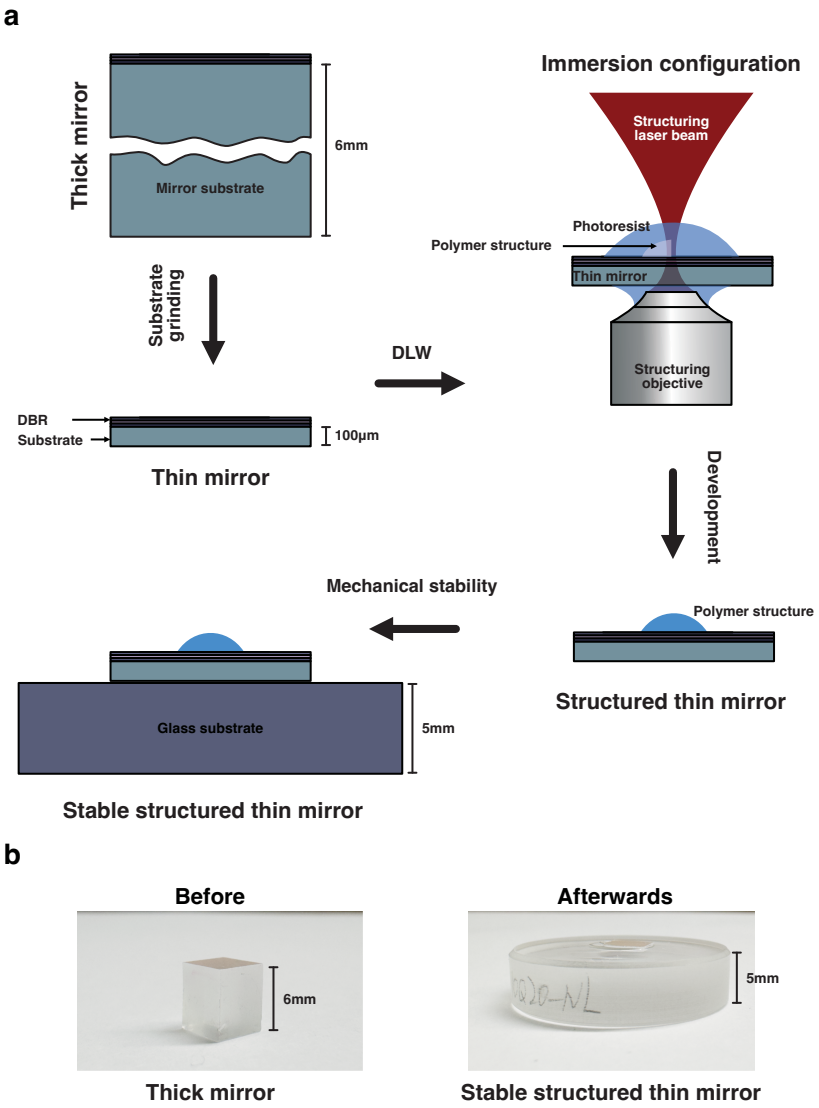

Figure 4.5: Quasi-stepless nanostructuring technique. **a.** A schematic illustrating the fabrication process for quasi-stepless nanostructures. The thick DBR mirror substrate is ground down to approximately 100 µm, rendering it sufficiently thin for use in the immersion configuration of direct laser writing (DLW) to produce smooth, quasi-stepless structures. Excess photoresist is removed during the development step. For mechanical stability and ease of handling in the dye microcavity setup, the structured thin mirror is bonded to a thick glass substrate. **b.** Images of the DBR mirror before and after application of the quasi-stepless nanostructuring technique.

The AFM height profile of the resulting parabolic structure, fabricated using the quasi-stepless nanostructuring method, is presented in Figure 4.6**a**. The two-dimensional height map exhibits a smooth gradient, with no indication of step artefacts. A radial average was applied to the measured two-dimensional profile (Figure 4.6**a**), yielding the measured height profile $h_m(r)$ (solid blue curve), which was subsequently compared to the parabolic profile $h_e(r)$ (dashed black curve), as shown in Figure 4.6**b**. The measured height profile $h_m(r)$

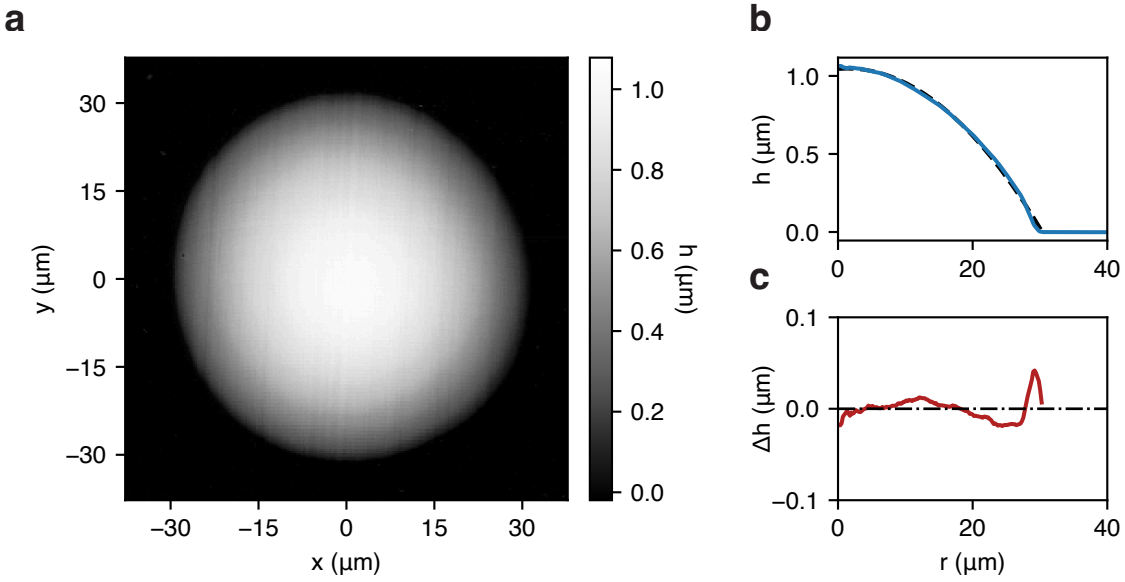

Figure 4.6: Measured height profile of the polymer structure with a parabolic height profile, fabricated using the quasi-stepless nanostructuring technique and characterised via atomic force microscopy (AFM). **a.** The transverse height profile is presented as a heat map, with the colour bar indicating height. **b.** The radial average of the height profile is shown, with the measured profile plotted as a solid blue curve and the ideal parabolic profile overlaid as a dashed black curve. **c.** The deviation of the measured radial average from the ideal parabolic shape is plotted as a solid red curve. Zero deviation is indicated by a dashed dotted black line.

closely follows the expected behaviour. The deviation between $h_m(r)$ and $h_e(r)$, denoted $\Delta h_m(r)$, is plotted in Figure 4.6**c**. As in previous results (cf. Figure 4.3**c**), low-frequency oscillations are absent in the central region of the structure, excluding the edge region around $r \geq 30$ µm. This confirms that the structure is quasi-stepless in the bulk. The maximum absolute deviation in this region, $|\Delta h_m|$, is substantially less than 0.05 µm.

Accordingly, in this work, the quasi-stepless nanostructuring method was employed for the fabrication of structures requiring a smooth change in height profile, such as the parabolic structure presented here. For other structures without such requirements, including flat-top geometries such as cuboids (corresponding to rectangular-base box potentials) and cylinders (corresponding to circular-base box potentials), the dip-in configuration was used, as the longitudinal modulation of the exposing light does not affect the transverse height profile of the structure.

4.4.1 Other constraints on direct laser writing

Although direct laser writing offers several advantages over other mirror structuring techniques, it is accompanied by a number of specific, albeit relatively minor, challenges and limitations. In this work, these limitations are discussed to ensure that future applications in dye microcavity platforms can be designed with these constraints in mind, potentially allowing them to be

addressed or overcome in subsequent developments.

Potential depth

Owing to the finite height of the polymer structure, the potential depth V_0 is also finite and is given by

$$V_0 = \frac{m_{\text{eff}}c^2}{n_d^2}\frac{n_s - n_d}{n_d}\frac{h_0}{D_0}, \tag{4.4}$$

where h_0 denotes the height of the polymer structure. The potential depth is directly proportional to h_0. An appropriate value for h_0 can therefore be estimated to ensure the potential is sufficiently deep while still maintaining adequate space between the structured surface and the unstructured cavity mirror to accommodate the dye solution.

The DLW-structured cavity configuration can be constrained to exhibit properties comparable to those of the conventional dye microcavity, as described in [27]. The optical path length in the conventional cavity [3], $n_d D_c$, can be matched to the optical path length in the DLW-structured cavity, given by

$$n_d D_c = n_d d_d + n_s h_0, \tag{4.5}$$

where d_d denotes the distance travelled by photons within the dye solution. For typical longitudinal mode number in conventional dye microcavity of $q = 7$ and a cutoff wavelength $\lambda_c = 580$ nm, this yields $d_d = 7\lambda_c/(2n_d) \simeq 1410$ nm [27].

Considering the $q \leq 11$, the maximum optical path length in the conventional cavity can be estimated as $n_d D_c = 11\lambda_c/2$, which implies $D_c \simeq 2215$ nm. Substituting into Equation 4.5, the structure height is found to be $h_0 \leq 748$ nm [4], assuming refractive indices $n_d = 1.44$ for the dye solution and $n_s = 1.55$ for the polymer.

Accordingly, the depth of the potential, excluding zero-point energy contributions, is given by $V_0 \leq 55$ meV, which corresponds to approximately $2k_B T$ at room temperature ($T = 300$ K). However, the effective depth observed in experiments, defined as the energy difference between the ground mode and the potential edge, will be reduced due to the presence of zero-point energy.

Mechanical stability

The direct laser writing structuring technique does not result in a permanent modification of the mirror surface, as the polymer structures can be removed mechanically without causing damage to the underlying DBR stack. This feature enables mirror reuse and facilitates rapid prototyping iterations. However, it also introduces certain challenges. Considerable care must be taken when handling the mirror, particularly during the reduction of cavity length and the adjustment of mirror tilt, to avoid direct contact between the structured surface and the opposing mirror.

[3] This assumes an ideal scenario. In practice, a portion of the field extends into the mirrors, resulting in the surface-to-surface spacing being smaller than the optical path length divided by the refractive index [63, 111]

[4] The true height of the printed structure may exhibit a global offset owing to residual deviations in the substrate tilt correction performed immediately prior to fabrication.

Despite this mechanical sensitivity, the polymer structures were found to be chemically stable within the dye solution bath and showed no signs of degradation over the course of extended experimental runs. After such prolonged use, partial evaporation of the dye solution may occur, necessitating mirror cleaning. This process is especially challenging, as no mechanical force can be applied without risking detachment of the structures. Consequently, cleaning must be performed exclusively using solvent rinses, such as isopropanol, to avoid dislodging or shifting the polymer structures from their original positions.

CHAPTER 5

Dimensional crossover: experimental results

In this chapter, an observation of a dimensional crossover from two to one dimension in a photon gas confined within a harmonic oscillator potential is presented. It is shown that while the photon gas exhibits signatures of Bose–Einstein condensation (BEC) phase transitions in two dimensions, it displays a crossover behaviour in one dimension. The harmonic oscillator confinement allows this distinction to emerge clearly, as the dimensionality substantially affects the density of states, which in turn governs the nature of the transition from a classical gas to a quantum degenerate regime in finite-depth potentials, as discussed in Section 2.2.3. Furthermore, as elaborated in Section 2.3.2, the suppression of additional effects such as interactions and dimension-influenced thermalisation facilitates the unambiguous observation of the dimensional crossover for the photon gas confined within a dye microcavity.

The chapter is structured as follows. In Section 5.1, the tuning of dimensionality in a harmonic oscillator confinement is examined, together with the criteria required for achieving a one-dimensional potential, followed by the modelling of the theoretical expectations for the observables. This is followed, in Section 5.2, by a discussion of how harmonic oscillator potentials across two to one dimensions can be realised for the photon gas using the direct laser writing (DLW) nanostructuring technique. Their characterisation is presented in Section 5.3. The effects of the dimensional crossover are then examined in Section 5.4 by analysing the energy-resolved occupation of the ground and excited energy levels of the potentials. Finally, a calorimetric analysis is presented in Section 5.5.

5.1 Theoretical modelling

As the dimensionality is reduced, the geometry of the confining potential is maintained as a harmonic oscillator. This choice is motivated by the fact that a harmonic oscillator in the isotropic two-dimensional (2D) limit supports a Bose–Einstein condensation (BEC) phase transition [20, 62, 112], thereby enabling direct comparison as the dimensionality is varied. The dimensional crossover is implemented by altering the aspect ratio of the harmonic

oscillator potential, beginning with an isotropic 2D configuration, transitioning through an anisotropic two-dimensional (2D-1D) regime, and ultimately reaching a highly elongated one-dimensional (1D) harmonic oscillator potential [1].

Consider the eigenenergies of a particle confined within a two-dimensional (2D) anisotropic harmonic oscillator potential, which are given by

$$E = \hbar\omega_x \left(i + \frac{1}{2}\right) + \hbar\omega_y \left(j + \frac{1}{2}\right), \quad i, j = 0, 1, 2, \ldots \tag{5.1}$$

where ω_x and ω_y denote the angular trap frequencies along the x and y directions, respectively, while i and j denote the corresponding quantum numbers.

To realise a dimensional crossover from two to one dimension, the ratio of the angular trap frequencies (trap aspect ratio), defined as $\Lambda = \omega_y/\omega_x$, serves as a tuning parameter. Under this definition, the energy spectrum in Equation 5.1 can be rewritten in the form

$$E = \hbar\omega_x \left(i + \frac{1}{2} + \Lambda j + \frac{\Lambda}{2}\right), \quad i, j = 0, 1, 2, \ldots \tag{5.2}$$

5.1.1 Constraints for 1D potential

The parameters defining the effective one-dimensional (1D) potential can be estimated by imposing constraints derived from the excitation probability of photons into the second spatial dimension. A spatial dimension here, along y is considered to be frozen out if the occupation of its excited level is substantially suppressed. For an anisotropic harmonic potential, this condition is satisfied when

$$\hbar\omega_y^{1D} > k_B T, \tag{5.3}$$

ensuring that the Boltzmann-weighted occupation probability, $\exp(-\hbar\omega_y/k_B T)$, becomes exponentially small [30]. Furthermore, if the excited state along the second dimension is not confined due to the finite depth of the potential, the system is effectively reduced to a one-dimensional confinement.

From the inequality 5.3, at ambient temperature $T = 300$ K, the minimum trapping frequency along the second dimension is estimated to be

$$\omega_y^{1D} > k_B \mathrm{T}/\hbar = 2\pi \times 6.25 \text{ THz} . \tag{5.4}$$

5.1.2 Theoretical expectation of observables

The potentials are theoretically modelled based on measured trap parameters. The measurement of trap parameters will be discussed in the following Section 5.3. The bound states of the harmonic oscillator potential are calculated based on the energy spacing defined by $\omega_{x,y}$, or alternatively by ω_x and the aspect ratio Λ, as introduced in Equation 5.2. The measurable

[1] The intermediate region is chosen such that substantial anisotropy is present, while remaining below the threshold for a one-dimensional regime. The conditions required to reach the one-dimensional limit will be discussed in the following section.

effective depth of the potential is given by $V_{\text{eff}} = V_0 - E_0$, where $E_0 = \hbar\omega_x/2 + \hbar\omega_y/2$ corresponds to the zero-point energy.

The resulting bound state spectrum is rescaled by setting E_0 to zero. The degeneracy, $g(\epsilon)$, of an energy level with energy ϵ is then determined by counting the number of occurrences of that level in the spectrum.

For a bound state with energy ϵ and corresponding degeneracy g_ϵ, the occupation probability is obtained from the Bose-Einstein distribution, as described in Equation 2.8 and reiterated here for convenience

$$N(\epsilon) = \frac{g(\epsilon)}{e^{\frac{\epsilon-\mu}{k_B T}} - 1} \,. \tag{5.5}$$

Here, the chemical potential μ is estimated by numerically solving the following equation

$$N = \sum_{\epsilon=0}^{\epsilon_{\max}} \frac{g(\epsilon)}{e^{\frac{\epsilon-\mu}{k_B T}} - 1} \tag{5.6}$$

where the total photon number N is determined experimentally, as described in Section 3.3.2.

Furthermore, the number of photons occupying the excited states, N_{ex}, and the ground state, N_0, is determined by the following expressions

$$N_{\text{ex}} = \sum_{\epsilon\neq 0}^{\epsilon_{\max}} \frac{g(\epsilon)}{e^{\frac{\epsilon-\mu}{k_B T}} - 1} \tag{5.7}$$

$$N_0 = \frac{g(0)}{e^{\frac{-\mu}{k_B T}} - 1} \tag{5.8}$$

The Equation 5.5 describes the spectral distribution of the photon gas and serves as a weighting function for the calculation of spatial and momentum-space distributions.

The spatial density distribution for these potentials is calculated by assuming the wavefunctions of a quantum harmonic oscillator. For a bound energy level with quantum numbers (i, j), the wavefunctions in the x and y directions are given by

$$\psi_i(x) = \frac{1}{\sqrt{2^i i!}} \left(\frac{m_{\text{eff}}\omega_x}{\pi\hbar}\right)^{1/4} \exp\left(-\frac{m_{\text{eff}}\omega_x x^2}{2\hbar}\right) H_i\left(\sqrt{\frac{m_{\text{eff}}\omega_x}{\hbar}}x\right) \,, \tag{5.9}$$

$$\psi_j(y) = \frac{1}{\sqrt{2^j j!}} \left(\frac{m_{\text{eff}}\omega_y}{\pi\hbar}\right)^{1/4} \exp\left(-\frac{m_{\text{eff}}\omega_y y^2}{2\hbar}\right) H_j\left(\sqrt{\frac{m_{\text{eff}}\omega_y}{\hbar}}y\right) \,, \tag{5.10}$$

where $H_{i,j}$ denote the Hermite polynomials. The density of the (i, j) mode with energy $\epsilon_{i,j}$ is obtained by taking the outer product of $\psi_i(x)$ and $\psi_j(y)$ and absolute square. The total spatial density distribution of the photon gas, for a total photon number N, is then given by:

$$\Psi(x, y) = \sum_{\epsilon_{i,j}} |\psi_i(x)\psi_j^*(y)|^2 N_{\epsilon_{i,j}} \,. \tag{5.11}$$

Similarly, the spatial distribution of excited states (i.e., excluding the ground state) is given by

$$\Psi_{\text{excited}}(x,y) = \sum_{\epsilon_{i,j}\neq 0} |\psi_i(x)\psi_j^*(y)|^2 N_{\epsilon_{i,j}} \,. \tag{5.12}$$

The momentum density distribution is obtained by applying a Fourier transform to the spatial wavefunctions of the harmonic oscillator potential. This transformation maps the wavefunctions to Hermite-Gaussian forms in momentum space, identical in form to their spatial counterparts, up to phase factors, thus allowing the momentum space density distribution to be calculated accordingly.

5.2 Parabolic structures as harmonic oscillator potentials

The photon gas potentials induced by the DLW, as discussed in Chapter 2 and Chapter 4, exhibit an inverted geometry relative to the height profile of the structure, owing to the negative sign, for $n_s > n_d$, as expressed below:

$$V(x,y) = -\frac{m_{\text{eff}}c^2}{n_d^2}\frac{n_s - n_d}{n_d}\frac{h(x,y)}{D_0} \tag{5.13}$$

It can be observed that the potential depth increases as the structural height increases. Consequently, by fabricating a structure with a maximum height h_0, corresponding to a maximum potential depth V_0, and allowing the height to decrease radially with a parabolic profile, an attractive potential with harmonic oscillator geometry can be realised. This is illustrated by considering a height profile as follows

$$h(x,y) = \begin{cases} h_0 - \zeta_x x^2 - \zeta_y y^2 & \text{if } h_0 - \zeta_x x^2 - \zeta_y y^2 \geq 0 \\ 0 & \text{otherwise} \end{cases} \tag{5.14}$$

where $h(x,y)$ denotes the height of the polymer structure at the transverse coordinates (x,y), ζ_x and ζ_y represent the curvature parameters along the x and y axes, respectively.

By substituting this height profile into Equation 5.13 and rearranging terms, the resulting potential is given by

$$\begin{aligned} V_1(x,y) &= -\frac{m_{\text{eff}}c^2}{n_d^2}\frac{n_s - n_d}{n_d}\frac{h_0 - \zeta_x x^2 - \zeta_y y^2}{D_0} \\ &= -\frac{m_{\text{eff}}c^2}{n_d^2}\frac{n_s - n_d}{n_d}\frac{h_0}{D_0} + \frac{1}{2}m_{\text{eff}}\left(\frac{c^2}{n_d^2}2\frac{n_s - n_d}{n_d}\frac{\zeta_x}{D_0}x^2 + \frac{c^2}{n_d^2}2\frac{n_s - n_d}{n_d}\frac{\zeta_y}{D_0}y^2\right) \end{aligned} \tag{5.15}$$

This expression can be directly compared to the two-dimensional anisotropic harmonic potential of finite depth V_0, defined as

$$V_2(x,y) = -V_0 + \frac{1}{2} m_{\text{eff}} \left(\omega_x^2 x^2 + \omega_y^2 y^2 \right) \tag{5.16}$$

from which it is evident that the angular trap frequencies are determined by the curvature parameters via

$$\omega_{x,y} = \frac{c}{n_d} \sqrt{2 \frac{n_s - n_d}{n_d} \frac{\zeta_{x,y}}{D_0}} \,. \tag{5.17}$$

The constraints on the angular trapping frequencies $\omega_{x,y}$ can be estimated based on the maximum allowable structure height, ($h_0 \leq 748$ nm), as discussed in Section 4.4.1, and by the transverse extent of the fabricated structure. The transverse extent is limited to under 60 µm, which facilitates efficient coupling of the structured pump light with sufficient intensity and helps to mitigate deviations of the structure's height profile from the designed geometry.

As detailed in Section 4.4.1, for $D_0 \simeq 2215$ nm , $n_s = 1.55$, and $n_d = 1.44$, the curvature parameter of the structure and the corresponding angular trapping frequencies are bounded from below as follows

$$\zeta_{x,y} \geq 8.31 \times 10^2 \text{ m}^{-1} \tag{5.18}$$

$$\omega_{x,y} \geq 2\pi \times 0.22 \text{ THz} \tag{5.19}$$

Consequently, the polymer structures must be fabricated with heights below 748 nm, and with curvature parameters no less than $8.31 \times 10^2 \text{m}^{-1}$. In the case of quasi-1D confinement, a minimum curvature of $\zeta_y^{1\text{D}} = 5.2 \times 10^5 \text{m}^{-1}$ is required along the strongly confined axis, corresponding to a trapping frequency of $\omega_y^{1\text{D}} = 2\pi \times 6.25$ THz (see Section 5.1.1).

It should be noted that these estimations provide only approximate bounds for the relevant parameters, rather than absolute values, as the trapping characteristics also depend on non-static, continuously tunable parameters such as the cavity length D_0.

Parabolic polymer structures designed within these constraints and exhibiting varying ratios of angular trapping frequencies have thus been fabricated to emulate isotropic two-dimensional (2D), anisotropic two-dimensional (2D–1D), and one-dimensional (1D) harmonic oscillator potentials, respectively. Their properties are characterised in the Section 5.3.

5.3 Characterisation and modelling of harmonic potentials

A characterisation of the potentials rendered by the polymer nanostructuring is carried out through measurements of the spatial, momentum, and spectral density distributions, obtained via cavity fluorescence. Obtained experimental data for the spatial density distribution of the degenerate photon gas confined in isotropic two-dimensional (2D), anisotropic two-dimensional (2D–1D), and one-dimensional (1D) harmonic oscillator potentials is presented in Figure 5.1, with corresponding microscope images of the fabricated polymer structures

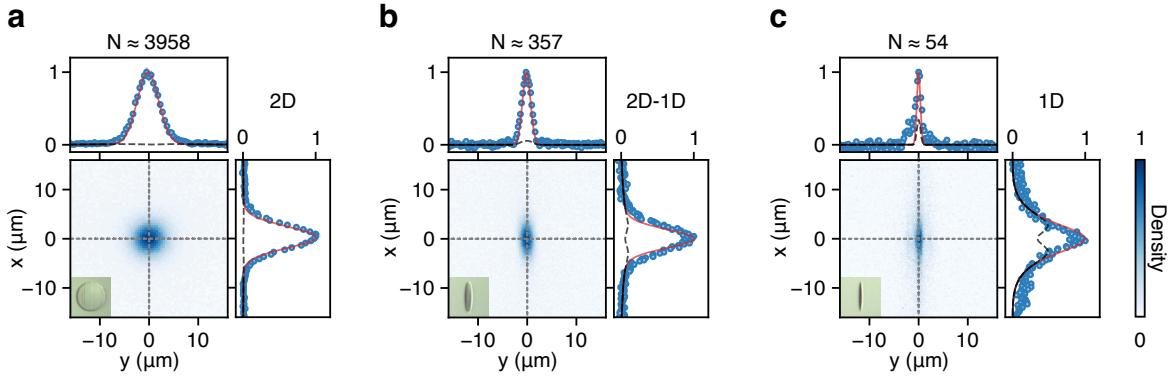

Figure 5.1: Spatial photon density distributions in the quantum degenerate regime for varying trap dimensionalities. **a–c.** Photon density profiles are shown for a two-dimensional (**a**, $\Lambda = 1$), anisotropic two-dimensional (**b**, 2D–1D, $\Lambda = 5$), and one-dimensional (**c**, $\Lambda = 22$) harmonic oscillator potential. Insets display microscope images of the corresponding polymer structures, fabricated on the cavity mirror using the quasi-stepless nanostructuring technique. Dashed lines indicate the positions of horizontal and vertical cross-sectional cuts through the centre of the photon cloud, which are shown in the side and top panels, respectively. In each cross-section, the dashed grey curve represents the thermal contribution, while the solid red curve shows the contribution from the ground mode, demonstrating its macroscopic occupation across all geometries. Theoretical predictions are based on a Bose–Einstein distribution of photons within the cavity modes, with total photon numbers of $N = 3958$ (2D), $N = 357$ (2D-1D), and $N = 54$ (1D). The deviation observed in the 1D configuration is attributed to the excitation of free-space modes near the edge of the confining potential.

shown in the insets.

As expected, the spatial density distribution appears symmetric in the 2D configuration, while asymmetries emerge in the 2D-1D and 1D cases. Line cuts along the x and y axes are compared to theoretical predictions based on the estimated photon number and trapping frequencies ω_x and ω_y, which are extracted from the spectral measurements. These comparisons demonstrate that the spatial extent of the photon gas becomes increasingly compressed along the tightly confining y-direction, while remaining broad along the x-axis as the system transitions from 2D to 1D. This behaviour, illustrated in the side panels of Figure 5.1, is consistent with theoretical expectations derived in the Section.5.1.2, for the extracted potential parameters.

While spatial distributions provide useful information, they are insufficient for determining the energy level spacing, degeneracies, and the mode occupations of the photon gas within these potentials as the different modes spatially overlap and thus cannot be resolved individually. These quantities are measured using a custom-built spectrometer setup, as described in Section 3.3. An exemplary real-space spectrum of a photon gas confined in a one-dimensional harmonic oscillator potential is presented in Figure 5.2**a**, where the discrete eigenmodes of the 1D quantum harmonic oscillator potential are clearly resolved.

The spacing between energy levels and the distribution of photons among these states are inferred by integrating the raw spectral data along the vertical (spatial) axis of the image in Figure 5.2**a**. The resulting integrated spectrum is shown in Figure 5.2**b**, and the positions of the spectral peaks are extracted and plotted as a function of mode number in Figure 5.2**c**.

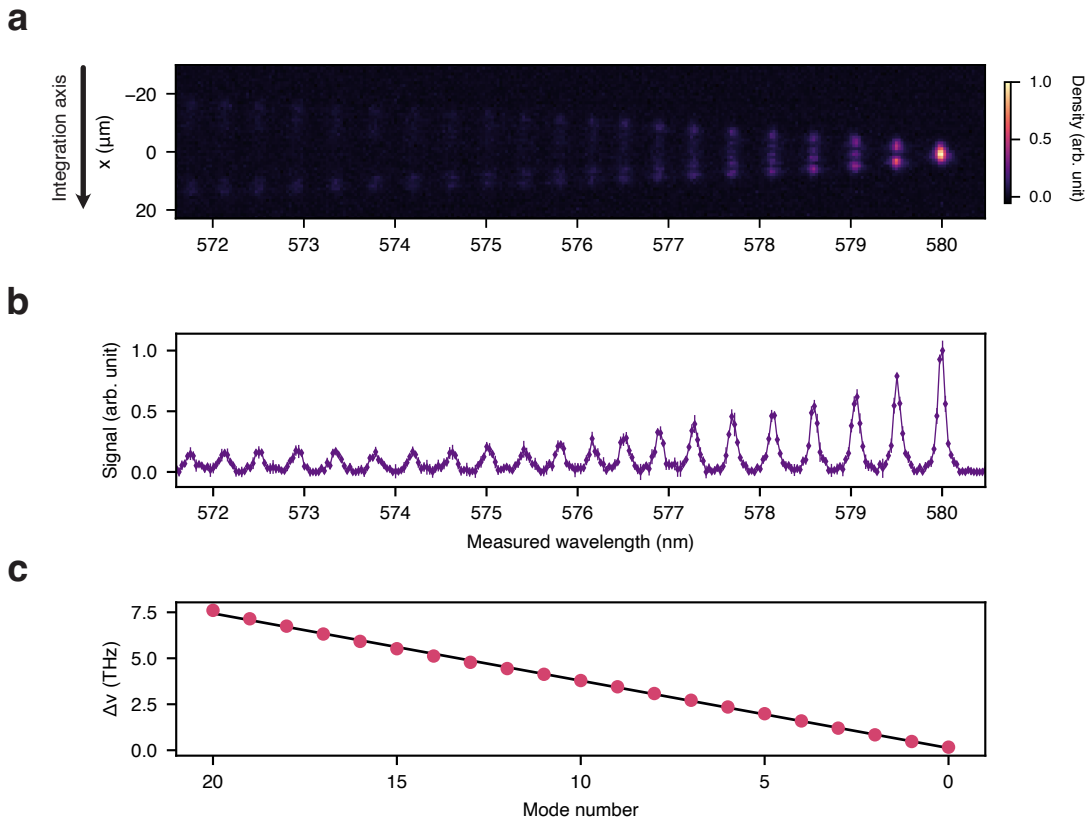

Figure 5.2: Spectrum analysis. An exemplary spectrum of the cavity fluorescence is presented for the one-dimensional case. **a.** The raw spectrometer image is shown, where the vertical axis corresponds to the spatial coordinate (x-axis), and the horizontal axis combines spatial (y-axis) and dispersive information. Spectral integration is performed along the vertical axis (spatial x-axis), as indicated by the arrow. Panels **a** and **b** share horizontal axis. **b.** The resulting spectrum, corrected for mirror transmission, is plotted on a linear scale. **c.** The positions of the observed modes are plotted in units of THz, relative to the ground mode identified in panel **b**, as a function of mode number. A linear increase in mode energy, $\Delta\nu$, with mode number is observed, in agreement with the expected behaviour of a harmonic oscillator potential, as indicated by the solid black line.

The linear trend observed in the peak positions confirms that the mode spacing is constant, consistent with the expected energy spectrum of a harmonic oscillator potential.

Moreover, the spatial mode profile observed in the raw spectrum reveals the absence of bound excited energy levels along the second spatial dimension, even beyond the 21$^{\text{st}}$ mode along the x axis. This absence implies that the ratio of trap frequencies is at least $\Lambda = \omega_y/\omega_x \geq 22$, corresponding to $\omega_y = 22 \times \omega_x = 2\pi \times 8.14$ THz, which exceeds the minimum frequency required for one-dimensional confinement, ω_y^{1D} (see Equation 5.4). This observation further confirms that the realised potential operates in an effectively one-dimensional regime.

For the study of dimensional crossover, precise control over the potential geometry in both spatial dimensions is essential. To confirm that the second dimension also exhibits harmonic confinement, one can examine the mode structure and the emergence of higher-dimensional

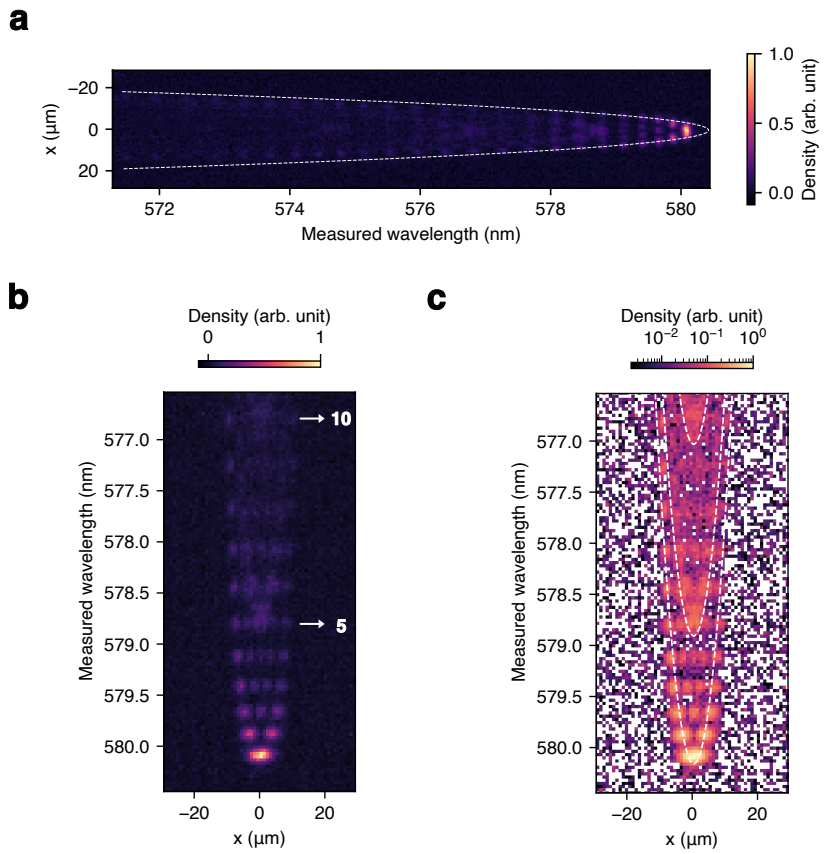

Figure 5.3: Spectrum analysis for the anisotropic 2D–1D case ($\Lambda = 5$). **a.** The raw spectrometer image is shown using a linear colour map, where the vertical axis corresponds to the spatial coordinate and the horizontal axis combines spatial and dispersive information. The mode size increases parabolically along the x direction, as indicated by the white dashed curve. **b–c.** Signatures of the emergence of the second dimension. In **b** (rotated and zoomed in version of **a**), the potential exhibits one-dimensional mode structure up to the fifth excited state, beyond which the first excited mode along the second dimension (along the y direction) appears. At the tenth mode along the x direction, the second excited mode along y also becomes visible, as expected from harmonic oscillator level spacing. This emergence of a family of excited modes is more clearly visible in the logarithmic colour map shown in **c**, where the mode structure is highlighted by dashed white parabolic curves.

features in the intermediate (2D–1D) regime, where the trap aspect ratio is $\Lambda = 5$.

In the raw spectrum corresponding to the 2D–1D potential shown in Figure 5.3**a**, a parabolic progression of real-space mode size as a function of energy is observed (indicated by the white dashed line). Upon closer inspection (see the zoomed-in spectrum in Figure 5.3**b**) distinct second-dimensional modes, specifically $(i = 0, j = 1)$ and $(i = 0, j = 2)$, are seen to emerge quite precisely at the positions of the $i = 5$ and $i = 10$ modes of the less confining x-direction.

These second-dimensional modes are accompanied by the corresponding mode families $(i, 1)$, $(i, 2)$ and so on, forming additional parabolic branches highlighted in Figures 5.3**b**–**c**. This clearly indicates that the second spatial dimension is also governed by a harmonic oscillator potential, with a trap aspect ratio of $\Lambda = \omega_y/\omega_x = 5$, thus confirming the intended

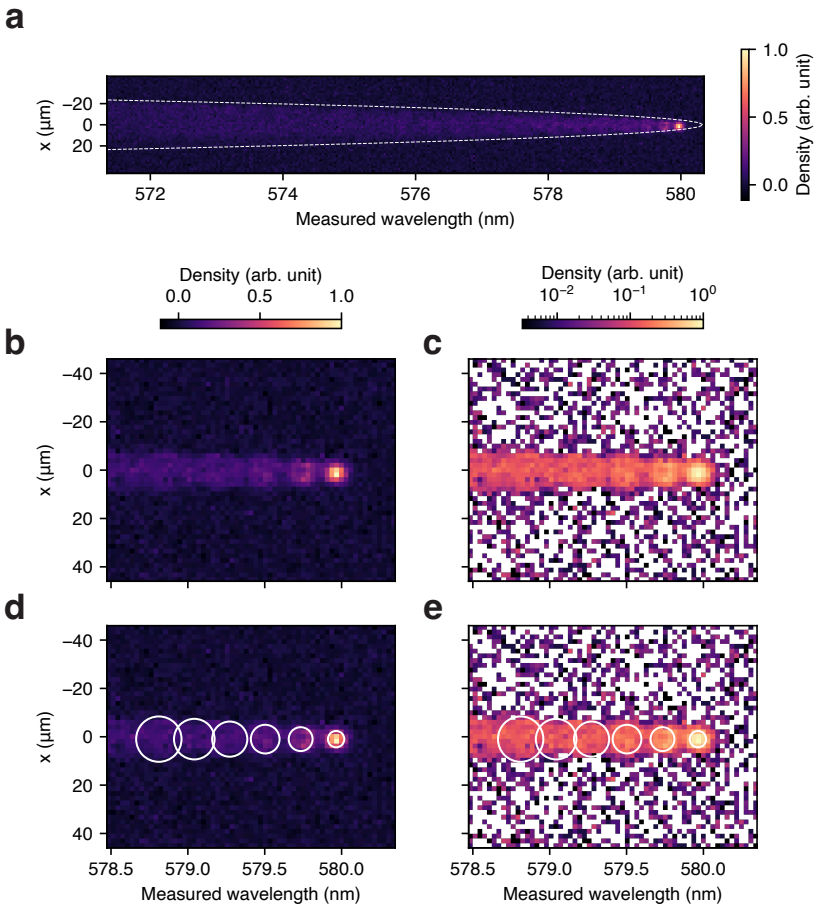

Figure 5.4: Spectrum analysis for the isotropic 2D case. **a.** The raw spectrometer image is shown using a linear colour map. The vertical axis corresponds to the spatial coordinate, while the horizontal axis combines spatial and dispersive information. The mode size increases parabolically along the x direction, as indicated by the white dashed curve. **b–e.** Signatures of isotropy. A zoomed-in views of panel **a** are presented. In **b**, the potential supports circularly symmetric modes, without any clear one-dimensional mode character. These isotropic modes are further visualised in **c** using a logarithmic colour map, which highlights the increasing spatial extent of the higher-order modes. In panels **d–e**, the spatial structure of the modes is compared to the expected harmonic spacing. Equidistantly spaced white circles (from centre to centre) are overlaid to illustrate the correspondence with the harmonic oscillator levels. At low energies, the mode separation is sufficiently large to allow individual modes to be resolved. However, the overlap between modes increases with energy, as indicated by the merging of adjacent circles, which leads to a reduction in spectral resolution.

geometry of the confinement.

Finally, the spectrum corresponding to the isotropic 2D harmonic potential, shown in Figure 5.4**a**, also exhibits the characteristic parabolic increase in mode size as a function of increasing energy (or, inversely with decreasing wavelength), similar to the 2D–1D case. Upon zooming into the low-energy region, the mode shapes are observed to be circularly symmetric and increase in spatial extent with rising energy, as indicated by the equidistant white circles (see Figures 5.4**a**–**c**).

This circular symmetry confirms the absence of anisotropy in the confinement, consistent with the spatial density distributions discussed earlier. Although mode overlap becomes more pronounced at higher energies, due to the nature of slit-less spectroscopy and the increasing size of harmonic oscillator mode size, the overlap among the lowest-lying modes remains sufficiently small to allow reliable extraction of the trap frequency.

Thus, by analysing the mode shapes and energy level spacing, the parameters characterising the harmonic potentials were estimated and are summarised in Table 5.1, along with the corresponding longitudinal mode number q [2]. In addition to the trapping frequencies ω_x and ω_y, the effective potential depth V_{eff} was determined. This quantity was measured as the energy difference between the ground state and the last bound state of the potential, identified by the termination of cavity fluorescence and the emergence of unconfined free-space modes.

Dimension	Λ	ω_x (THz)	ω_y (THz)	V_{eff} (THz)	V_{eff} ($k_{\text{B}}T$)	q
2D	1	$2\pi \times 0.223$	$2\pi \times 0.223$	7.747	1.239	8
2D-1D	5	$2\pi \times 0.33$	$2\pi \times 1.65$	7.855	1.256	8
1D	22	$2\pi \times 0.37$	$2\pi \times 8.14$	7.629	1.220	10

Table 5.1: Measured parameters of the potentials for photons gas realised using DLW. The potentials exhibit harmonic oscillator mode spacing with varying trap aspect ratio and thus ratio of trapping frequencies Λ, with effective depth V_{eff} i.e energy spacing between the ground mode and top of the potential for corresponding longitudinal mode number q

Additionally, access to the momentum-space distribution was enabled by the experimental setup through an optical Fourier transform, as discussed in Chapter 3. Figure 5.5 presents the momentum-space distribution of the photon gas in both 2D and 2D-1D harmonic potentials [3], under classical and quantum degenerate regimes. The expected extent of the thermalised photon gas in momentum space was determined from the effective potential depth, V_{eff}, as measured from the spectrum. This extent is indicated by a red dashed circle, where the wavevectors satisfy the condition $k_x^2 + k_y^2 = 2m_{\text{eff}}V_{\text{eff}}/\hbar^2$, and lies within the detection limits imposed by the numerical aperture (NA) of the setup, denoted by the black circle.

Good agreement is observed between the measured size of the photon gas cloud and theoretical predictions, thereby validating the parameters derived from the spectral data. The anisotropy of the potential is evident in the momentum distribution: in the quantum degenerate regime, the ground mode shape appears isotropic for the 2D potential and elongated for the 2D-1D case (see Figure 5.5). It should be noted that the momentum-space photon distribution is rotated by 90° [4] with respect to the spatial density distribution (see Figure 5.1), a feature that is particularly apparent in the 2D-1D case (Figure 5.5**b**). Theoretical expectations for the momentum-space distribution were also computed and show good agreement with the experimental data (see side panels in Figure 5.5).

[2] The choice of q is motivated by the fact that any further reduction in the cavity length would result in a collision between the plane cavity mirror and the structure fabricated on the opposite mirror. The value of q was minimised as far as possible, depending on the height of the structure.

[3] In the 1D case, momentum-space measurements were not feasible due to the broad momentum distribution combined with the low photon number, which led to poor signal-to-noise ratio.

[4] In atomic Bose Einstein condensates, the inversion of the axis during time of flight has long been regarded as evidence of a transition from a thermal cloud to a Bose Einstein condensate [66, 113, 114].

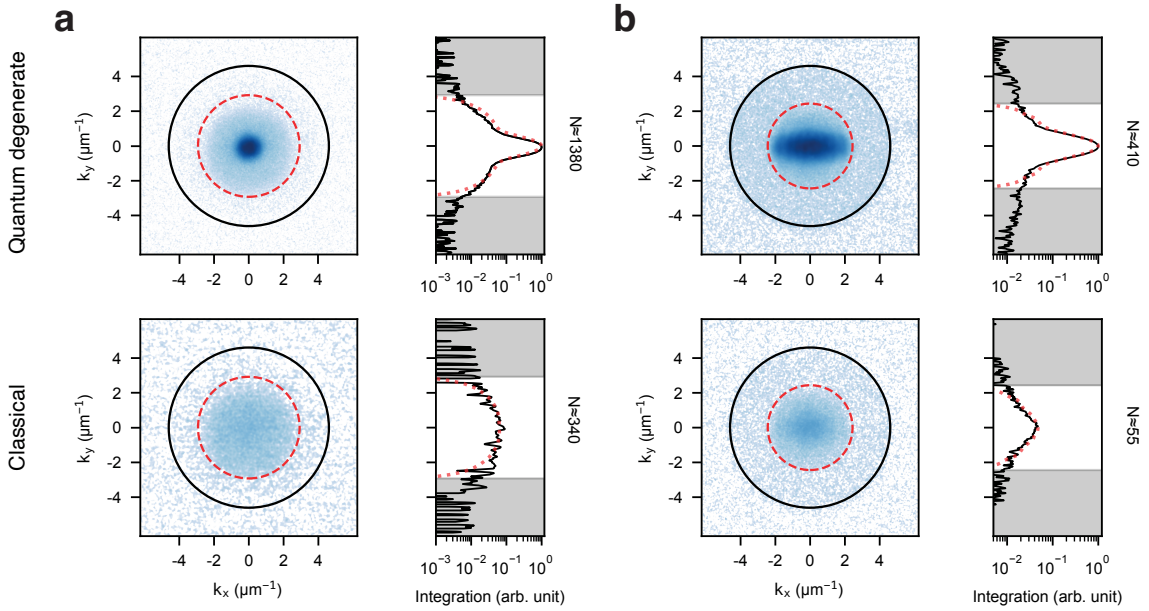

Figure 5.5: Experimental momentum-space distributions. Exemplary momentum-space distributions of the cavity fluorescence are shown for the two-dimensional (panel **a**) and anisotropic two-dimensional (2D–1D, panel **b**) configurations, in both the classical and quantum degenerate regimes. The red dashed circle indicates wavevectors satisfying $k_x^2 + k_y^2 = 2m_{\mathrm{eff}}V_{\mathrm{eff}}/\hbar^2$, while the black circle marks the numerical aperture (NA) of the imaging system. Side panels display the distributions integrated along the k_x direction, with the corresponding theoretical expectations plotted as red dotted lines. The extended tails of the distributions, reaching into regions of wavevector space beyond the confinement of the trapping potential (denoted by grey shaded areas), are attributed to emission from free-space modes that are not confined by the potential.

5.4 Absence of criticality

Having established the presence of quantum harmonic oscillator potential across the dimensional crossover from 2D to 1D, the influence of dimensionality on the presence of a Bose–Einstein condensation (BEC) phase transition is investigated. The total photon number, N, is selected as the scanning parameter. This choice is justified by the dependence of the chemical potential on both temperature and total photon number; an increase in the total photon number plays a role analogous to a reduction in temperature.

As the ground mode is spectrally resolved in the 2D, 2D–1D, and 1D spectra, the number of photons in the excited states, N_{ex}, is obtained by summing over all spectral modes excluding the ground state. In Figure 5.6, the photon population of the excited states, N_{ex}, is compared to that of the ground state, N_0, as a function of N, for all three configurations.

Since a well defined critical photon number is not available for the 2D–1D case [30], the observables N, N_{ex}, and N_0 are scaled individually to an aspect-ratio dependent characteristic photon number $\tilde{N}$. The scaling photon number, $\tilde{N}$, is defined as the photon number at which the $\tilde{\mu} = \partial U/\partial N$, reaches half of its low photon number limit, i.e., $\tilde{\mu}(\tilde{N}) = \tilde{\mu}(N \to 0)/2$. This

quantity is estimated theoretically to enable consistent comparisons across dimensions [5].

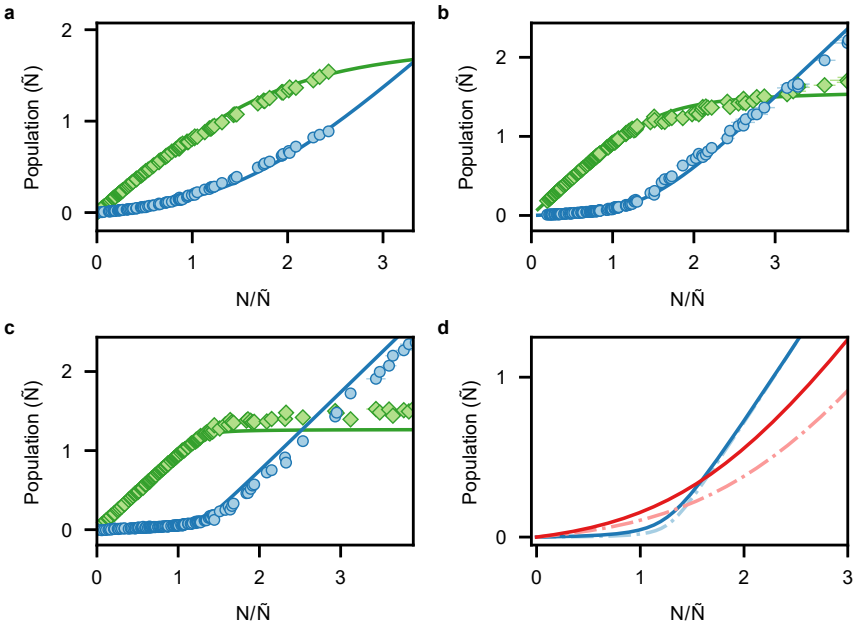

Figure 5.6: Ground versus excited mode populations. **a–c.** The populations in the ground mode (blue dots) and in the excited modes (green diamonds) are shown as a function of scaled total photon number for the 1D case (**a**, $\Lambda = 22$), the 2D–1D case (**b**, $\Lambda = 5$), and the 2D potential (**c**, $\Lambda = 1$). Solid lines represent theoretical predictions based on a Bose–Einstein distribution across the cavity modes. **d.** A comparison of theoretical ground-mode populations is presented for one-dimensional (red) and two-dimensional (blue) harmonic potentials, each with an equal number of energy levels. Predictions for finite-size systems with trap depth $1.2k_{\mathrm{B}}T$ (solid lines) are contrasted with those for quasi-infinite systems of depth $10k_{\mathrm{B}}T$ (dash-dotted lines). The dimensional crossover is observed to have a more pronounced effect on ground-state population than the finite size of the system. For visual comparison, the horizontal axis is rescaled for each geometry using the normalised photon number $\tilde{N}$, defined as $\tilde{N} = 628$ (2D), $\tilde{N} = 64$ (2D–1D), and $\tilde{N} = 23$ (1D), as described in the main text.

Initially, both the ground and excited state populations increase linearly, with the population of the excited states growing significantly faster. This trend, however, undergoes a sharp change in the case of the isotropic 2D potential with $\Lambda = 1$, where the population in the excited states ceases to increase and saturates. In contrast, the ground state population exhibits a threshold-like increase, continuing to grow (see Figure 5.6**a**), indicating the onset of Bose–Einstein condensation (BEC).

A similar but less pronounced behaviour is observed in the 2D–1D crossover potential with $\Lambda = 5$. In contrast, for the 1D potential with $\Lambda = 22$, no threshold behaviour is detected. Instead, the populations in both the ground and excited states exhibit a smooth, monotonic

[5] Alternative definitions of the characteristic photon number may be formulated. For instance, it may be determined as the photon number at which the internal energy per photon first undergoes a change in gradient during the transition from a classical gas to a quantum degenerate gas, or it may be specified by higher order moments of the internal energy per photon. However, the definition adopted in the present work, although seemingly arbitrary, is straightforward to evaluate.

increase, suggesting the absence of a BEC phase transition. These observations are in good agreement with theoretical predictions based on Equations 5.7 and 5.8.

In the 1D case, the finite depth of the potential, identical to that used in the 2D configuration, results in a reduced number of available modes, thereby softening any sharp features associated with the phase transition. To assess the extent of this effect, theoretical expectations for the ground-state population, obtained numerically, are presented for both finite-depth ($1.2k_BT$) and quasi-infinite-depth ($10k_BT$) potentials in 1D and isotropic 2D geometries, each with the same number of bound energy levels. The corresponding results are shown in Figure 5.6**d**.

While the threshold behaviour characteristic of the BEC transition becomes marginally sharper in the quasi-infinite 2D case, no such features emerge in the 1D configuration. This result suggests that dimensionality plays a dominant role over potential depth in determining the presence or absence of BEC phase transition signatures.

5.5 Calorimetry along the dimensional crossover

For isotropic 2D harmonic potential, a direct mapping between N and T exists, i.e, both the critical photon number and critical temperature are well defined [30], and C_V has been employed in prior studies to demonstrate the BEC phase transition in a photon gas [71]. However, for dimensions less than 2, such as in the case of a anisotropic two-dimensional potential with aspect ratio $\Lambda = 5$, no such mapping is available. Consequently, as discussed in Section.2.2.3, the thermodynamic quantity $\tilde{\mu}(N)$ is chosen as the primary thermodynamic observable to investigate the BEC phase transition, owing to its capacity to sharply distinguish between a BEC phase transition and a crossover.

As introduced in Section 2.2.3, $\tilde{\mu}(N)$ is defined as the partial derivative of the internal energy with respect to the total particle number (in this context, the total photon number), given by

$$\tilde{\mu} = \frac{\partial U}{\partial N} \ , \tag{5.20}$$

where the internal energy U of the photon gas is computed by summing the energies of the bound modes weighted by the corresponding photon occupancies

$$U = \sum_{\epsilon} \epsilon_{\epsilon} N_{\epsilon} \ . \tag{5.21}$$

Experimentally, U and N can be extracted from the measured real-space spectra. Importantly, the experimental observables U/N and $\tilde{\mu} = \partial U/\partial N$ are independent of the calibration constant α that relates the photon number, N, to the camera counts C via $N = \alpha C$. Since $U = \sum_{\epsilon} \epsilon N_{\epsilon} = \alpha \sum_{\epsilon} \epsilon C_{\epsilon}$, it follows that $U/N = \sum \epsilon C_{\epsilon}/C$. Consequently, $\tilde{\mu}$ is also independent of α, and changes in this calibration constant does not affect the underlying physics.

The internal energy per photon, U/N, as a function of the normalised photon number $N/\tilde{N}$, is displayed in Figure 5.7**b** for all three potential geometries: 2D, 2D-1D, and 1D. In all cases, U/N is observed to decrease with increasing $N/\tilde{N}$, following theoretical expectations, though at different rates depending on the geometry. However, high-frequency noise in the measured U/N data introduces substantial numerical artefacts when calculating the derivative. This

was mitigated by first binning the photon number data for U to suppress numerical noise.

The impact of this binning procedure is analysed in Figures 5.8-5.10, where three different common ratios are applied to the binning process. The original and binned data are shown in blue, green, and red, while the resulting $|\tilde{\mu}|$ are compared to theoretical predictions (solid black lines). Although binning does influence the level of numerical noise, it does not alter the qualitative features associated with BEC transitions or crossovers. Smaller bin sizes (i.e., smaller common ratios) fail to sufficiently suppress the noise, whereas larger bin sizes (larger ratios) reduce data resolution. A compromise is therefore adopted to balance these two extremes.

The observed variation of $|\tilde{\mu}|$ on $N/\tilde{N}$, extracted from the numerically differentiated binned photon number data for U (bins of photon number in a geometric series spacing with a common ratio of 1.2, 1.3 and 1.2 for the 2D, the 2D–1D and the 1D harmonic oscillator potentials, respectively), reveals a strong contrast between BEC and crossover regimes (see Figure 5.7**a**). For all three geometries,$|\tilde{\mu}|$ decreases as the photon gas evolves from a classical regime to a quantum-degenerate state. In the 2D isotropic harmonic oscillator potential, a sharp decline in $|\tilde{\mu}|$ is observed around $N/\tilde{N} \approx 1$, after which it remains nearly constant, consistent with the presence of a BEC transition. In contrast, for the one-dimensional potential, $|\tilde{\mu}|$ decreases smoothly, thereby indicating the absence of a genuine Bose-Einstein condensation (BEC) phase transition and the presence of a crossover. The intermediate case of the anisotropic two-dimensional (2D-1D) geometry, characterised by an aspect ratio $\Lambda = 5$, exhibits softened phase transition features. This behaviour underscores a gradual and continuous evolution from a sharp BEC phase transition to a smooth crossover.

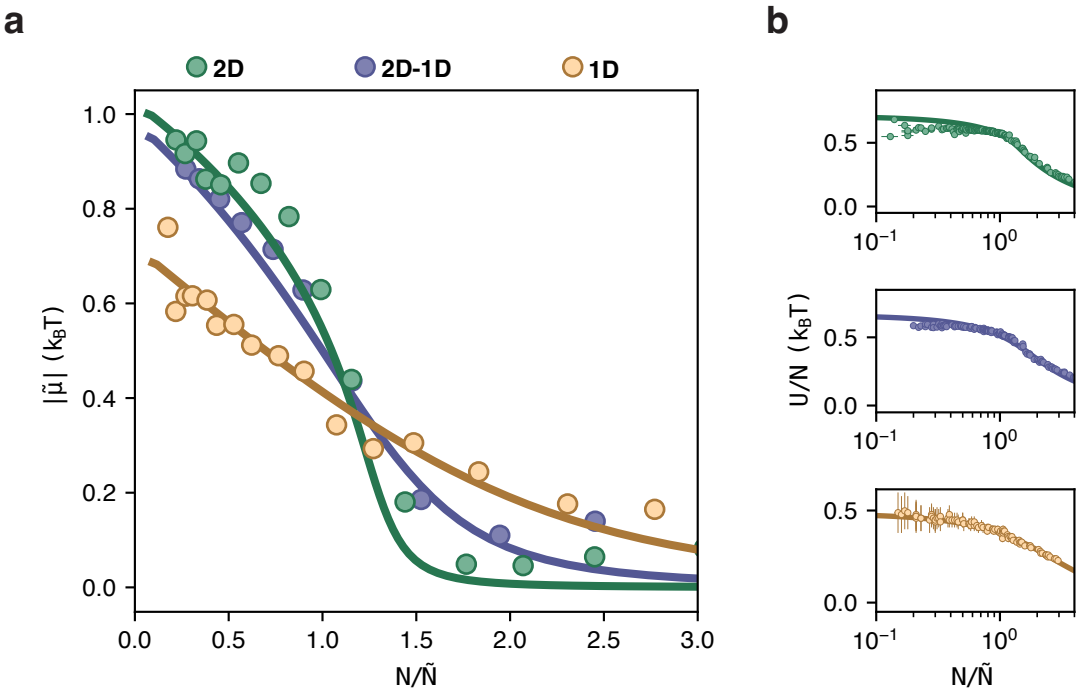

Figure 5.7: Caloric properties of the photon gas. The transition from a thermodynamic phase transition in two dimensions to a smooth crossover in one dimension is reflected in the behaviour of $\tilde{\mu}$. **a.** The measured absolute value of $|\tilde{\mu}|$, normalised by the thermal energy $k_{\mathrm{B}}T$, is shown as a function of the rescaled total photon number $N/\tilde{N}$ for the 1D, 2D–1D, and 2D harmonic oscillator potentials (symbols). The zero-point energy is set to zero. Theoretical predictions for each geometry are shown as solid curves. **b.** The measured internal energy per photon, also normalised by $k_{\mathrm{B}}T$ (symbols), is plotted against the rescaled total photon number $N/\tilde{N}$ for the same geometries, arranged from top to bottom as 2D, 2D–1D, and 1D. The corresponding theoretical expectations are shown as solid lines.

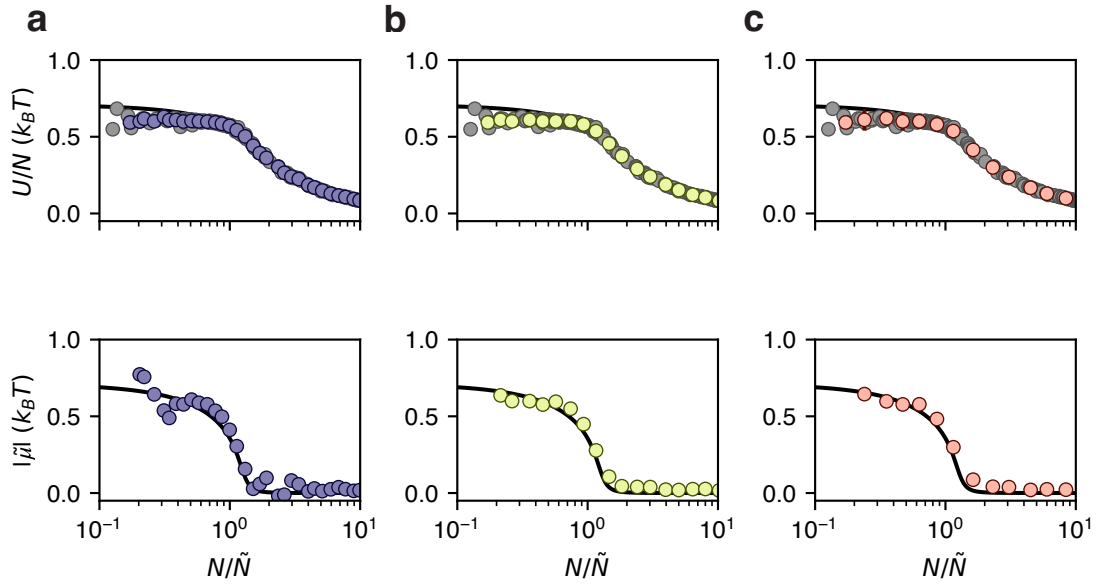

Figure 5.8: Binning effects on the caloric properties in the two-dimensional (2D) potential. **a–c.** The unbinned internal energy per photon, U/N, is shown in grey, with the corresponding theoretical prediction indicated by the solid black curve. Binned data, presented as mean values ± standard deviation, are shown for three different geometric binning series with common ratios of 1.145 (blue), 1.271 (green), and 1.381 (red), plotted in separate columns. **d–f.** The corresponding data for the $|\tilde{\mu}|$, are shown using the same binning schemes (symbols), with theoretical expectations again indicated by the solid black curve.

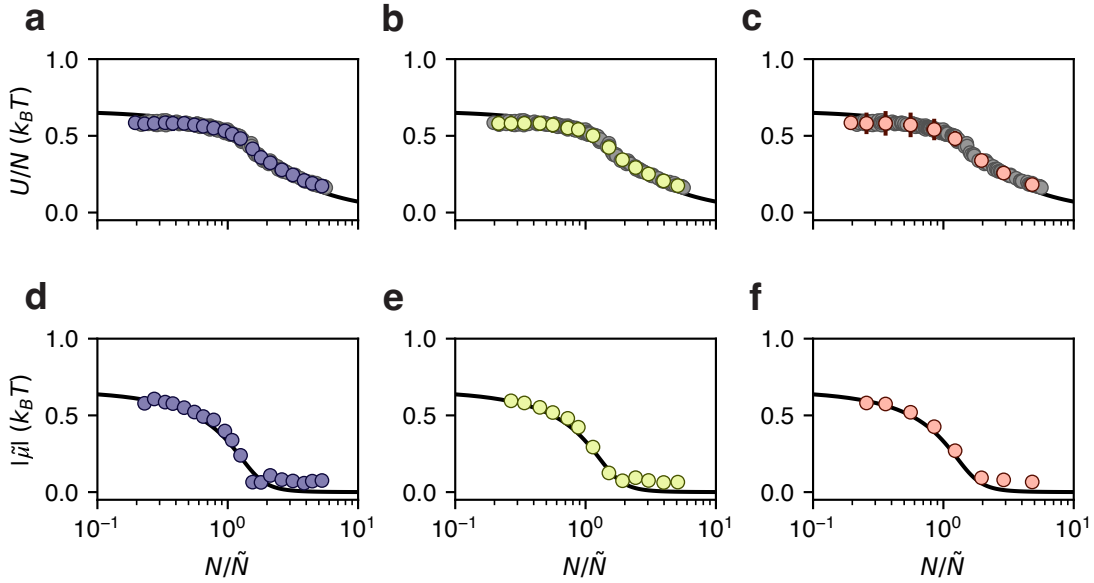

Figure 5.9: Binning effects on the caloric properties for the 2D–1D potential. **a–c.** The unbinned internal energy per photon, U/N, is shown in grey, with theoretical expectations indicated by the solid black curve. Binned data, presented as mean values ± standard deviation, are plotted using geometric binning series with common ratios of 1.189 (blue), 1.278 (green), and 1.523 (red), each shown in a separate column. **d–f.** Corresponding results for the absolute value of the normalised $|\tilde{\mu}|$, are shown (symbols), with theoretical predictions again plotted as solid black curves.

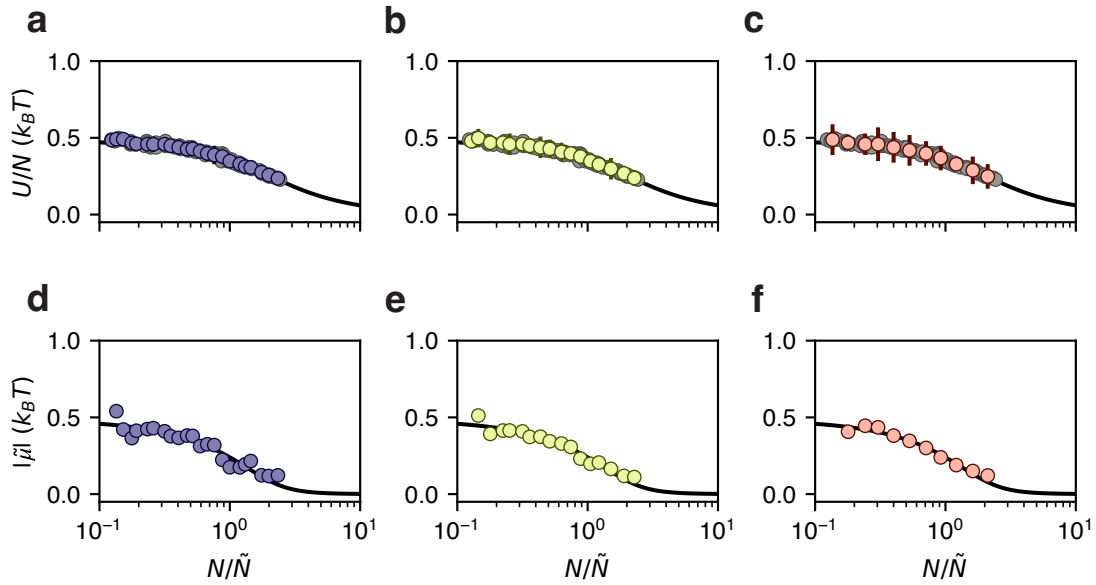

Figure 5.10: Binning effects on the caloric properties for the 1D potential. **a–c.** The unbinned internal energy per photon, U/N, is shown in grey, with the corresponding theoretical expectations indicated by the solid black curve. Binned data, presented as mean values ± standard deviation, are plotted using geometric binning series with common ratios of 1.144 (blue), 1.198 (green), and 1.318 (red), shown in three separate columns. **d–f.** The corresponding data for the absolute value of the normalised $|\tilde{\mu}|$, are shown as symbols, with theoretical predictions again plotted as solid black curves.

CHAPTER 6

Engineering coupled and high-curvature potentials for photon gas in dye microcavities using direct laser writing

The direct laser writing technique has proven to be a powerful method for fabricating high-curvature structures within the dye microcavity platform, as demonstrated in the previous chapter. In this chapter, the aim is to illustrate how this approach can open new avenues of physics to be explored in this platform.

The high curvature and sub-micron feature sizes achievable with direct laser writing, down to approximately 0.1 µm enable the fabrication of small potentials while preserving sharp edges. To investigate this, small box potential with a side length of 10 µm is investigated in Section 6.1, testing whether the potential geometry is preserved upon miniaturisation. Subsequently, the limit of coupled single mode potentials is explored through the realisation of a double well potential in Section 6.2, allowing estimation of the coupling strength between individual wells. This coupling strength is then used to assess the feasibility of fabricating extended 1D lattice geometries, as discussed in Section 6.3. Finally, an exploration of a regime in which the characteristic photon number falls beneath one photon is presented in Section 6.4. All of these structures will be investigated spectroscopically. For the majority of potentials covered in this chapter, attention is directed towards the potential landscape and, when possible, the associated distribution. These observations constitute a proof of principle study. These potential landscapes do not require gradual variations in curvature. Instead, a step function like height profile is sufficient and can be achieved using the simpler dip-in configuration of direct laser writing, thereby eliminating the need for a substrate preparation stage.

6.1 Small box potential for photon gas

Box potentials for the dye microcavity platform, realised using a delamination technique in previous work [28], enabled the investigation of compressibility in an optical quantum gas. The smallest box sizes previously demonstrated had side lengths of 20 µm. When attempting to reduce the box size further, the curvature of the structure's walls plays a substantial role, rendering the potential closer to that of a harmonic oscillator and consequently distorting the intended dispersion. This limitation has now been overcome through the application of direct laser writing (DLW), which allows the fabrication of box potentials with side lengths below 20 µm without significantly affecting the dispersion as the transverse feature size is $\leq$ 100 nm. This advancement is demonstrated here by DLW 3D-printing a box potential with side lengths of 10 µm.

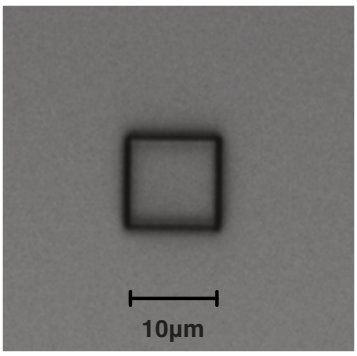

Figure 6.1: Optical microscope image of a 10 µm × 10 µm box structure fabricated using the dip-in configuration of direct laser writing (DLW).

A box potential is realised by printing the 3D polymer structure with the following height profile

$$h(x,y) = \begin{cases} h_0 & \text{if } (L_x - 2|x|) \cdot (L_y - 2|y|) \geq 0 \\ 0 & \text{otherwise} \end{cases} \tag{6.1}$$

where L_x and L_y represent the side lengths of the box along the x and y directions, respectively. The structure possesses a uniform height of h_0. A microscope image of the resulting 3D-printed polymer structure on a cavity mirror with $L_x = L_y = 10$ µm is shown in Figure 6.1.

The potential landscape is obtained by substituting this height profile into Equation 2.1, yielding

$$V(x,y) \simeq \begin{cases} -V_0 & \text{if } (L_x - 2|x|) \cdot (L_y - 2|y|) \geq 0 \\ 0 & \text{otherwise} \end{cases} \tag{6.2}$$

This represents a box potential with a depth

$$V_0 = \frac{m_{\text{eff}} c^2}{n_d^2} \frac{n_s - n_d}{n_d} \frac{h_0}{D_0} \ . \tag{6.3}$$

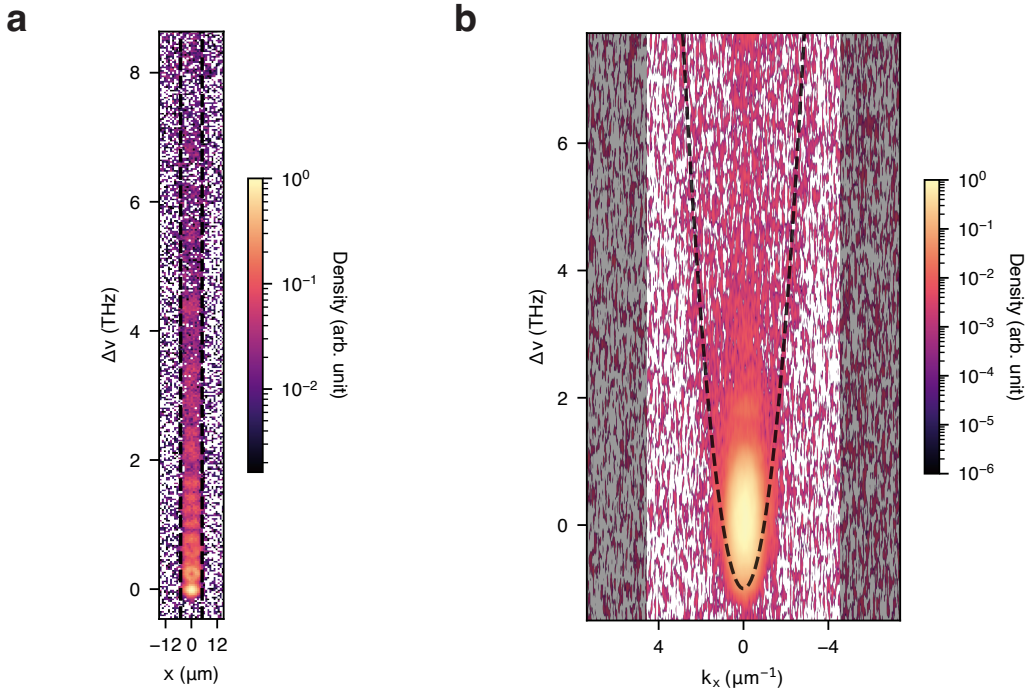

Figure 6.2: Exemplary spectral dispersion of a 10 µm × 10 µm box potential in real and momentum space. **a.** The expected spatial bounds of the box potential are indicated by dashed black lines at −5 µm and 5 µm, overlaid on the raw real-space spectrogram. The match with the anticipated spatial extent highlights signatures of sharp confinement boundaries. **b.** The raw momentum-space spectrum of the same box potential is shown, with the expected parabolic dispersion indicated by an overlaid dashed black curve, consistent with the relation $\Delta\nu \propto k_x^2$. Regions shaded in grey denote wavevector components beyond the numerical aperture (NA) of the detection system.

The spatial extent of the modes in real space is expected to remain constant regardless of energy. In contrast, in momentum space, the mode size is anticipated to increase with energy, exhibiting a parabolic dispersion [28]. To investigate this behaviour, a dual spectroscopy setup, comprising both real and momentum space spectrometers, was employed to measure the corresponding spectra of the photon gases in such box potential (see Figure 6.2). In real space, the modes were observed to maintain a constant size, as expected. This is indicated by the black dashed lines at −5 µm and 5 µm, corresponding to the designed width $L_x = 10$ µm, in Figure 6.2**a**. In momentum space, despite a reduced signal to noise ratio resulting from the larger mode sizes, a parabolic dispersion was observed, consistent with the theoretical relation $\Delta\nu \propto k_y^2$, as shown by the black dashed curve in Figure 6.2**b**.

The results indicate that the DLW-fabricated box structure reproduces essential features of a photon gas in a box potential in both real and momentum space, even at transverse scales as small as 10 µm. Additionally, the effective potential depth, $V_{\text{eff}} > \hbar 2\pi \times 6$ THz, implies that the side walls of the structure remain sufficiently steep, preserving the depth of the potential. This finding is particularly substantial, as it allows for realising deep, single-mode (zero-dimensional) traps, which are critical for lattice engineering as will be discussed in the following sections. More comprehensive investigations of polymer based box potentials have

already been reported in the referenced Master's thesis [105]. However, in the present work, a photon gas confined in a significantly smaller box potential than those previously realised [28, 105] has been demonstrated, and also its dispersion in momentum space has been measured spectroscopically.

6.2 Coupled microscopic potentials

Previous significant work on two coupled potentials in dye-filled microcavity platforms was conducted using a delamination technique. In that study, two coupled wells, resembling harmonic oscillators, each supporting a single bound energy level, were investigated, with coupling rates on the order of $2\pi \times 30$ GHz [93]. In the present work, the use of the DLW technique, which enables smaller transverse feature sizes, allows the realisation of box-like potential wells, each supporting a single bound energy level.

The energy spacing in a box potential with side length L scales as $1/L^2$. For sufficiently small transverse dimensions, a potential of finite depth V_0 may support only a single bound energy level. This bound state exhibits no degrees of freedom in any spatial direction, thereby rendering the system effectively zero-dimensional or may be regarded as a photonic quantum dot.

Here, a radially symmetric version of the box potential is considered, specifically, a circular pillar potential of radius R and depth V_0. The resulting potential landscape is described as follows

$$V(x,y) \simeq \begin{cases} -V_0 & \text{if } (R^2 - (x-a)^2 - (y-b)^2) \geq 0 \\ 0 & \text{otherwise} \end{cases} \tag{6.4}$$

where the potential is centred at coordinates (a, b).

Such a potential may be realised through the fabrication of a cylindrical polymer pillars, as shown in Figure 6.3. The associated height profile is defined by:

$$h(x,y) = \begin{cases} h_0 & \text{if } (R^2 - (x-a)^2 - (y-b)^2) \geq 0 \\ 0 & \text{otherwise} \quad . \end{cases} \tag{6.5}$$

The energy eigenvalues of a circular pillar potential are given by

$$E_{(i,j)} = \frac{\hbar^2}{2m_{\text{eff}}R^2}[z_{(i,j_r)}]^2 \quad \text{for } i = 0, \pm1, \pm2, \pm3, \ldots \text{ and } j_r = 1, 2, 3, \ldots \ , \tag{6.6}$$

where $z_{(i,j_r)}$ denotes the j_r^{th} zero of the regular Bessel function $J_i(z)$ [115, 116].

A system may be considered zero-dimensional if the ground state energy $E_{0,1}$ lies below the potential depth V_0, while the first excited state's energy $E_{\pm1,1}$ exceed it. These conditions establish lower and upper bounds for the radius R, expressed as

$$R_{\text{lower}} = \sqrt{\frac{\hbar^2}{2m_{\text{eff}}V_0}[z_{(0,1_r)}]^2} \tag{6.7}$$

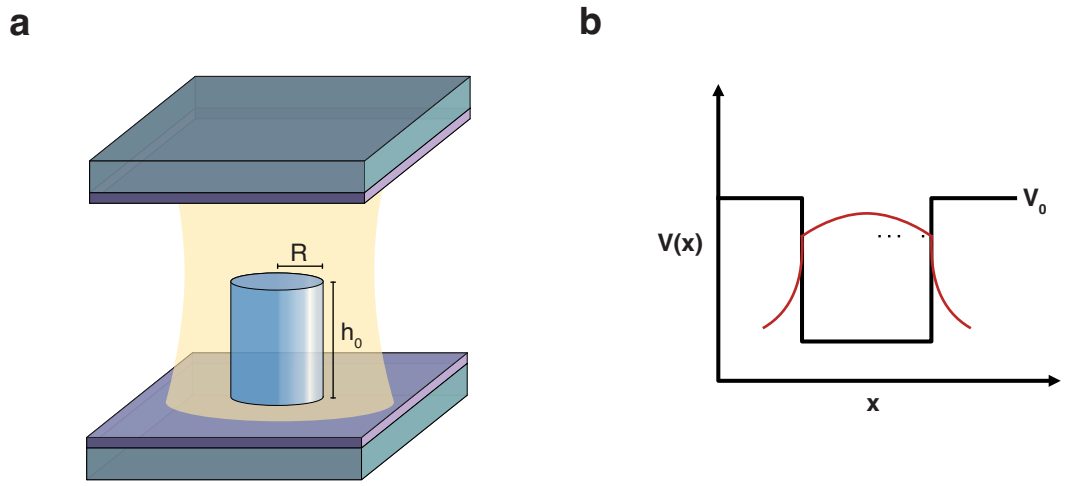

Figure 6.3: Schematic of a zero-dimensional potential. **a.** A microcavity incorporating a cylindrical polymer structure is shown. Circular pillar potentials are realised by fabricating a cylindrical structure with a circular base of radius R and height h_0 onto the mirror surface using the dip-in configuration of direct laser writing (DLW). **b.** The corresponding potential energy landscape is shown, featuring a single bound mode with an evanescently leaking component.

$$R_{\text{upper}} = \sqrt{\frac{\hbar^2}{2m_{\text{eff}}V_0}[z_{(\pm1,1,r)}]^2} \tag{6.8}$$

For a maximum potential depth of $V_0 = 2k_BT$, the corresponding bounds are $R_{\text{lower}} = 0.7\mu\text{m}$ and $R_{\text{upper}} = 1.1\mu\text{m}$, which fall within the feature size limits of the DLW fabrication method.

The mode profile in such a potential extends beyond the potential boundary, exhibiting an exponentially decaying tail. This evanescent part of the wavefunction provides a mechanism for photon tunnelling, which can be utilised to couple two such sites, thereby forming a double-well potential (see Figure 6.4).

The Hamiltonian describing such a double-well system can be written as

$$\mathcal{H} = \begin{pmatrix} 0 & 0 \\ 0 & \Delta E \end{pmatrix} - \hbar J \begin{pmatrix} 0 & 1 \\ 1 & 0 \end{pmatrix} = \begin{pmatrix} 0 & -\hbar J \\ -\hbar J & \Delta E \end{pmatrix} , \tag{6.9}$$

where ΔE denotes the energy detuning between the two wells, and J is the coupling strength [93]. The corresponding eigenenergies are

$$E_\pm = \Delta E/2 \mp \sqrt{(\hbar J)^2 + (\Delta E/2)^2} = \Delta E/2 \mp \hbar J' \implies \Delta E_\pm = 2\hbar J' \tag{6.10}$$

The resulting symmetric (ground) and antisymmetric (excited) eigenmodes, $\psi_\pm$, can be expressed as superpositions of the wavefunctions ψ_1 and ψ_2 of the individual wells

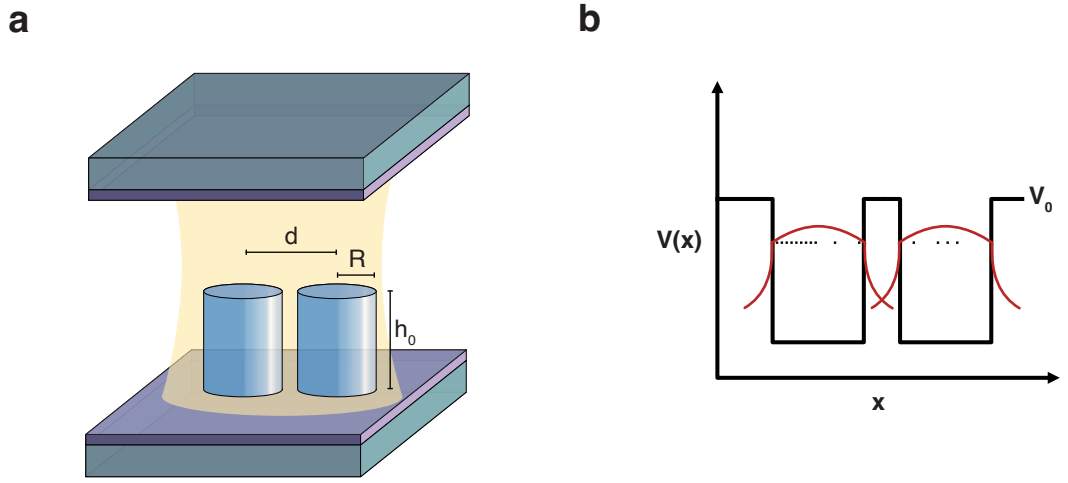

Figure 6.4: Schematic of two coupled zero-dimensional potentials. **a.** A microcavity incorporating two cylindrical polymer structures is shown. Each structure has a circular base of radius R and height h_0, and they are fabricated onto the mirror surface with a centre-to-centre separation of d, using the dip-in configuration of direct laser writing (DLW). **b.** The corresponding potential energy landscape is shown, featuring a single bound mode with evanescent coupling between the adjacent potentials.

$$\begin{aligned} \psi_+ &= \cos(\theta/2) \cdot \psi_1 + \sin(\theta/2) \cdot \psi_2 \\ \psi_- &= \sin(\theta/2) \cdot \psi_1 - \cos(\theta/2) \cdot \psi_2 \end{aligned} \tag{6.11}$$

where the mixing angle is defined as

$$\theta = \tan^{-1}(2\hbar J/\Delta E) \ . \tag{6.12}$$

In Figure 6.5, raw spectra of a photon gas confined within coupled cylindrical polymer structures of radius $R \approx 0.6\,\mu$m in a dye-filled microcavity are shown in panels Figure 6.5**d** to Figure 6.5**f**. These correspond to three different centre-to-centre spacings of the structures, $d = 2\,\mu$m, $1.5\,\mu$m, and $0.8\,\mu$m, as illustrated in panels Figure 6.5**a** to Figure 6.5**c**, respectively. Form the spectra, signatures of a symmetric ground state and an antisymmetric excited state are observed, consistent with the expected coupling between two potential wells.

Furthermore, the spatial mode density of the excited state is symmetric, suggesting that $\theta \approx \pi/2$, and hence $\Delta E \ll 2\hbar J$. It follows that the dominant contribution to the mode splitting $\Delta E_\pm$ arises from the coupling strength J. Additionally, it was observed that, upon tilting one of the cavity mirrors, no change in mode spacing was detected, suggesting that the coupling strength was dominant over the energy detuning.

The energy detuning ΔE is directly proportional to the height difference between the two polymer cylindrical pillars. The deviation introduced by inherent fabrication roughness is estimated as $\Delta h < 0.02\,\mu$m [1], corresponding to a relative energy shift of $\Delta E/E_{0,1} < 0.06$.

[1] Estimated from atomic force microscopy (AFM) measurements taken in the bulk of the structure, although of

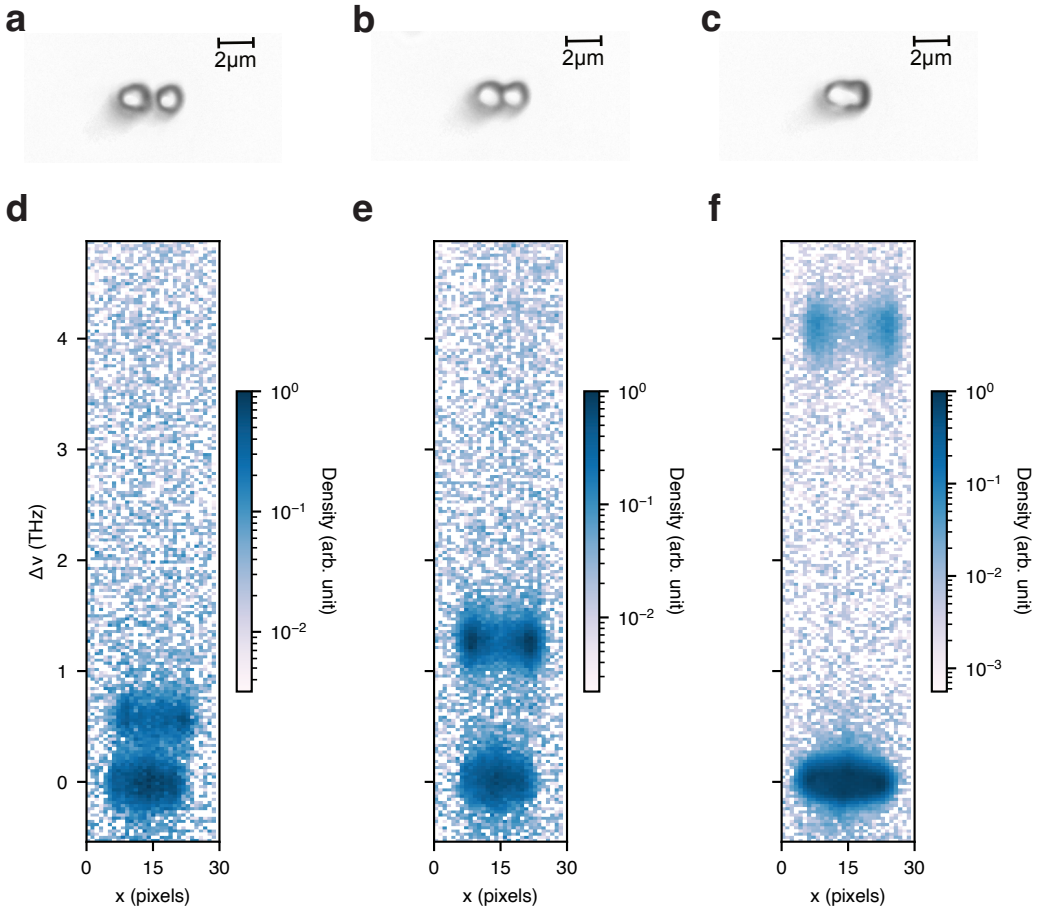

Figure 6.5: Mode hybridisation in a double-well potential. **a–c.** Optical microscope images of cylindrical polymer structures fabricated using the dip-in configuration of direct laser writing (DLW). The centre-to-centre spacing between the cylinders is $d = 2\,\mu\text{m}$, $1.5\,\mu\text{m}$, and $0.8\,\mu\text{m}$ in panels **a**, **b**, and **c**, respectively. The corresponding raw spectra of the coupled double-well potentials are shown in panels **d–f**, revealing two bound modes that are attributed to arise due to mode hybridisation. The horizontal axis represents the spatial dimension along the double-well axis, while the vertical axis denotes the dispersive direction, indicating the measured energy spacing with respect to the ground state in units of THz. To enhance the visibility of the antisymmetric (excited) eigenmodes, the image has been slightly defocused; as a result, the x-axis does not correspond to calibrated length units.

The coupling strength J is primarily determined by three parameters: the individual potential depth V_0, the base radius R of the potentials, and the centre-to-centre distance d between the potentials.

Owing to the constraints set by Equations 6.7 and 6.8, and the maximum achievable potential depth $V_{\text{max}} = 2k_BT$, the distance d is employed as the primary control parameter for tuning the coupling strength.

From the spectrograms, the energy difference between the ground and excited modes is

different geometry, described in Section 4.4.

extracted and plotted as a function of centre-to-centre distance d in Figure 6.6.

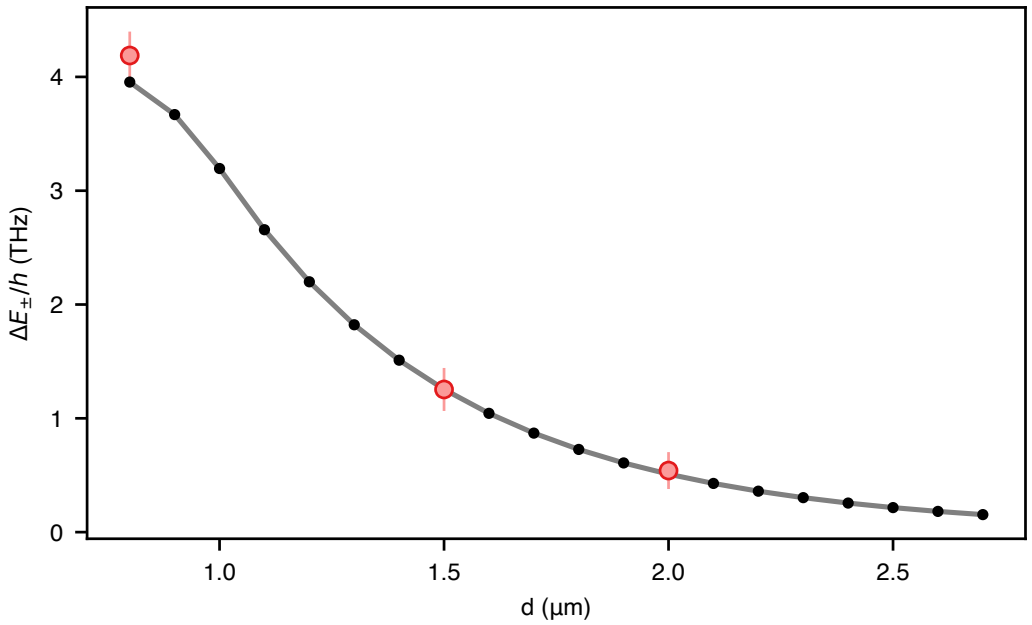

Figure 6.6: Mode separation energy in the double-well potential as a function of centre-to-centre distance d between the potentials. The measured data, extracted from the raw spectra shown in Figure 6.5, are indicated by red symbols. Corresponding numerical predictions are shown as black symbols, with a grey curve interpolating between them.

It is observed that the mode splitting $\Delta E_{\pm}$ increases as the centre-to-centre distance d is reduced, in good agreement with theoretical predictions obtained numerically using open-source Python package PyPBEC [117] [2]. The maximum coupling strength, $J \approx J'$, is achieved for a configuration in which the polymer pillars partially overlap [3], with $J' \approx 2\pi \times 2$ THz.

In contrast, for configurations without physical overlap (see Figure 6.5**a**), the coupling strength is reduced to $J' \approx 2\pi \times 0.25$ THz . Nevertheless, this value remains approximately an order of magnitude larger than those reported in previous studies on double-well potentials in dye-filled microcavity platforms [93]. Consequently, the use of multiple coupled pillars arranged in lattice geometries becomes experimentally feasible, as will be discussed in the following sections.

[2] The Python package was used exclusively for the extremely small potentials and lattice geometries presented in this work, as it was particularly helpful for the rapid optimisation of the design parameters of complex potential landscapes

[3] In this regime, the coupled wells may also be interpreted as an elongated box supporting two eigenmodes. The model remains valid because the mode amplitude is maximal at the pillar centre, and a similar arrangement of overlapping coupled pillars has been employed in polariton experiments [25].

6.3 Band structure engineering for photon condensates

The here observed high coupling strength between individual zero-dimensional potentials, in principle, allows for the realisation of large lattices. This is because strong coupling reduces the system's sensitivity to detuning variations between sites that may arise due to surface inhomogeneities. This can enable the study of phenomena such as the one-dimensional Kardar–Parisi–Zhang universality class [50–57], dissipation induced stable vortices in non-interacting systems [59], and the Bosonic skin effect through tunable coupling strength [58]. As a proof of principle technological demonstration towards realising such extended lattices, one-dimensional lattice structures consisting of 20 sites of various geometries have been fabricated using direct laser writing (DLW).

6.3.1 1D chain

A one-dimensional chain of cylindrical pillars, with a height of $h_0 = 400$ nm and a radius of $R = 0.7$ µm, was printed with a centre-to-centre spacing of $d = 1.3$ µm using a dip-in configuration. A top-down view of the resulting structure, captured using an optical microscope, is presented in Figure 6.7**a**. Analogous to the case of the double-well potential, the spectrogram of the photon gas distribution at cutoff wavelengths of 579.5 nm is shown in Figure 6.7**b**. The spectrogram reveals extended lattice modes with an increasing number of nodes as a function of energy. The experimentally measured spectrum (at equilibrium) is compared to a numerically calculated equilibrium spectral distribution, as shown in Figure 6.7**d**, corresponding to the lattice geometry illustrated in Figure 6.7**b**. A good agreement between the experimental and numerical spectra is observed (see integrated spectrum in Figure 6.7**e**), indicating the feasibility of hosting a near to equilibrium photon gas in extended lattices. However, the coupling strength in this structure lies at the higher end due to the partial overlap of the pillars, as evident in Figure 6.7**a**. As a result, the system may also be interpreted as a periodically modulated one-dimensional rectangular potential, which would similarly support comparable mode shapes and energy spacings. In many experimental platforms, arrays of overlapping pillars are regarded as lattice geometries. Such arrangements display characteristic lattice features [63] and have been employed in polaritonic systems to investigate Kardar-Parisi-Zhang physics [25].

6.3.2 SSH chain

The coupling between two zero-dimensional potentials can be controlled via the centre-to-centre distance, d. To demonstrate the realisation of a band structure in a lattice potential, characterised by features such as a band gap and distinct from continuous potentials like the one-dimensional rectangular potential, the Su–Schrieffer–Heeger (SSH) model [45–48] geometry was chosen. The SSH model requires alternating coupling constants, J_1 and J_2. Depending on the coupling constant of the terminating lattice sites, either a topologically trivial band structure with a band gap or a topologically non-trivial edge state situated within the band gap can be realised, as shown in Figure 6.8.

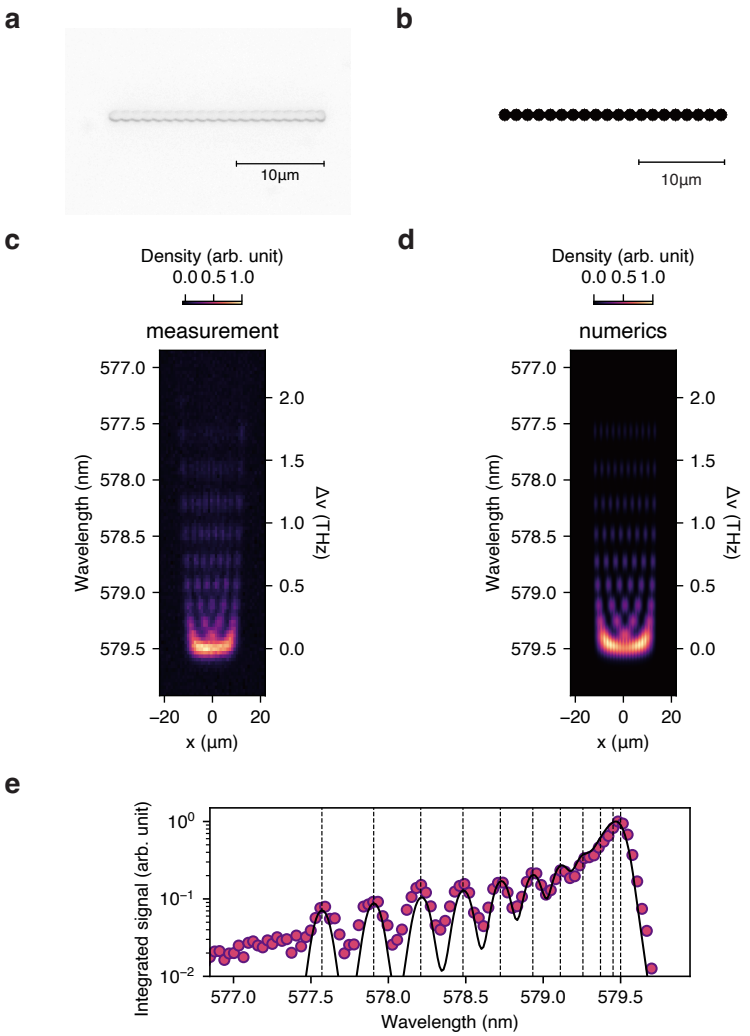

Figure 6.7: One-dimensional chain potential. **a.** Optical microscope image of a one-dimensional (1D) chain consisting of 20 cylindrical polymer structures, each with a radius $R = 0.7$ µm and a centre-to-centre spacing of 1.3 µm. **b.** Schematic of the 1D chain used for calculating the photon gas mode spectrum. **c.** Measured real-space spectrum of the photon gas confined within the 1D chain potential. **d.** Numerically calculated equilibrium distribution mode spectrum based on the schematic in panel **b**, including spectrometer resolution. Panels **c** and **d** display spectrograms in which the horizontal axis corresponds to the spatial dimension along the lattice chain, while the vertical axis represents the dispersion axis. **e.** Integrated spectra, with measured data shown as magenta-coloured symbols and the numerical prediction, based on a Bose–Einstein distribution, shown as a solid black curve. The exact expected mode positions are indicated by vertical black dashed lines.

The lattice potentials were implemented by coupling 20 zero-dimensional potentials with corresponding coupling strengths. Microscope images of the 3D-printed polymer structures for both the trivial and non-trivial SSH cases are presented in Figures 6.8**c** and 6.8**d**, respectively. The pillars were designed with a maximum height of $h_0 = 600$ nm and a radius of $R = 0.5$ µm. The centre-to-centre distances $d_1 = 0.7$ µm and $d_2 = 1.7$ µm were chosen to realise two

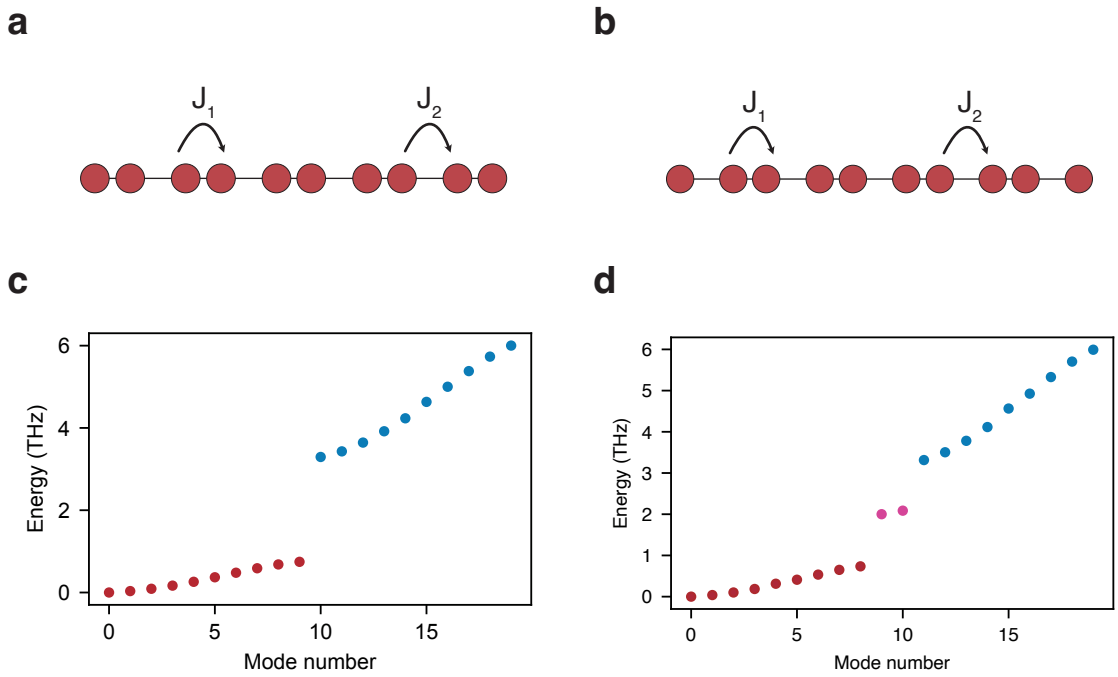

Figure 6.8: Schematic of the Su–Schrieffer–Heeger (SSH) one-dimensional model. **a.** A one-dimensional (1D) chain of zero-dimensional potentials is shown, with alternating coupling strengths J_1 and J_2, and terminating with a J_1 coupling. **b.** A similar 1D chain is shown, terminating instead with a J_2 coupling. **c.** Exemplary band structure calculated for the configuration in panel **a** (with 20 sites), showing a lower band (red) and an upper band (blue) with a visible band gap. **d.** Exemplary band structure calculated numerically, using PyPBEC [117], for the configuration in panel **b** (with 20 sites), also exhibiting a band gap. In this case, additional states appear in the middle of the gap, corresponding to topological edge modes.

clearly distinct coupling strengths, J_1 and J_2, respectively. Unlike in a 1D continuous chain, the pillars do not exhibit overlap, at least for the $d_2 = 1.7$ µm case, confirming the presence of discrete lattice potentials.

The spectrogram of the photon gas in the SSH lattices is shown in Figure 6.9 [4], where a clear separation between the ground and excited bands is observed in both cases, with an energy gap between them. This indicates the existence of two distinct coupling strengths, J_1 and J_2. In the trivial case, the band gap remains empty, whereas in the non-trivial case, two edge modes appear within the gap, one at each edge, in addition to the ground and excited energy bands. This confirms the feasibility of realising large lattices with significant photon hopping probability, enabled by high coupling strengths without site overlap. This proof of principle study demonstrates the potential of DLW for the fabrication of large lattice models,

[4] The difference in the onset of free-space modes between the SSH trivial and SSH non trivial lattice structures is attributed to a global offset in their heights. The offset may arise from inconsistencies in the tilt correction of the cavity mirror during fabrication. Because the structures are separated by more than 2 mm, even slight errors in tilt correction can introduce this effect. The issue may be avoided by printing the structures of interest side by side.

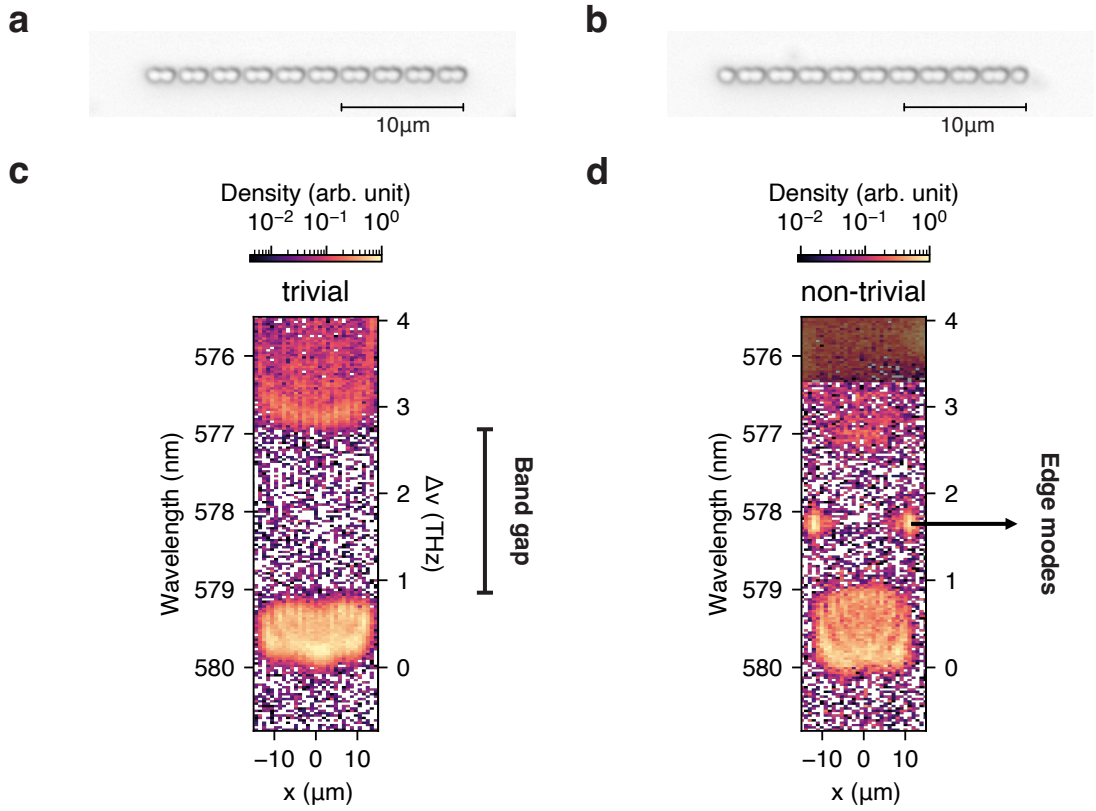

Figure 6.9: Investigating the Su–Schrieffer–Heeger (SSH) one-dimensional model in a dye microcavity. **a.** Optical microscope image of a one-dimensional (1D) chain of zero-dimensional potentials, consisting of 20 sites with alternating centre-to-centre spacings of $d_1 = 0.7$ µm and $d_2 = 1.7$ µm, corresponding to coupling strengths J_1 and J_2, respectively. The chain terminates with a J_1 coupling. **b.** Optical microscope image of a similar 1D chain with the same alternating spacings (d_1 and d_2), but terminating with a J_2 coupling. **c.** Measured real-space spectrum of the photon gas confined in the lattice potential shown in panel **a**, displaying upper and lower bands separated by a visible band gap. **d.** Measured real-space spectrum of the photons in the lattice potential shown in panel **b**, where in addition to the upper and lower bands, distinct edge modes are visible at either spatial boundary, with energies located in the middle of the band gap. The grey-shaded regions correspond to the ends of the potential and indicate the emergence of free-space modes. Panels **c** and **d** display spectrograms in which the horizontal axis corresponds to the spatial dimension along the lattice chain, while the vertical axis represents the dispersion axis.

enabling future studies of driven-dissipative physics in lattice geometries.

6.4 Towards sub one-photon characteristic photon number

The study of two-level systems, typically comprising an atom coupled to an electric field, has been thoroughly investigated [118] [119–121]. In recent work with a dye microcavity, a thermalised two-level system of light (that is, a potential featuring only two bound states accessible to photons), has been investigated [60]. In that work, the energy splitting between the modes ($\Delta E \simeq h \cdot 50$ GHz) was substantively smaller than the thermal energy. Above a characteristic photon number $N_{\mathrm{ch}} \simeq 2k_{\mathrm{B}}T/h\Delta\nu \simeq 250$, the ground-state mode was dominantly populated, whereas at low photon number, the populations of the states were nearly equal.

Continuing with the theme of few-level systems, it is also of interest to consider regimes in which the characteristic photon number, required for condensation into ground state, is on the order of a single photon or less, on average. Preliminary investigations into this regime have here been enabled in the dye microcavity platform through the use of DLW, and the initial results are presented herein. To design a potential in that regime, it is instructive to begin with strict constraints, as discussed below.

The occupation probability of a bound state with energy ϵ, relative to the ground state energy and with degeneracy $g(\epsilon)$, is described by the Bose–Einstein distribution, as expressed in Equation 2.8, which is reiterated here for convenience

$$N(\epsilon) = \frac{g(\epsilon)}{e^{(\epsilon-\mu)/k_{\mathrm{B}}T} - 1} \tag{6.13}$$

As outlined in Section 2.2.2, the corresponding saturation photon number at a fixed temperature T is given by

$$N_s = \sum_{\epsilon\neq 0}^{\epsilon_{\max}} \frac{g(\epsilon)}{e^{\epsilon/k_{\mathrm{B}}T} - 1} \,. \tag{6.14}$$

In a two-level potential the degeneracy $g(\epsilon)$ may be lifted by introducing transverse asymmetry and by restricting the system to a single polarisation subspace. The resulting potential supports two excited bound energy levels, each corresponding to a distinct spatial dimension, the saturation photon number can be decomposed as

$$\begin{aligned} N_s &= \sum_{\epsilon\neq 0}^{\epsilon_2} \frac{1}{e^{\epsilon/k_{\mathrm{B}}T} - 1} \,, \\ &= \frac{1}{e^{\epsilon_1/k_{\mathrm{B}}T} - 1} + \frac{1}{e^{\epsilon_2/k_{\mathrm{B}}T} - 1} = n_{e_1} + n_{e_2} \,. \end{aligned} \tag{6.15}$$

The saturation photon number n_e for a single bound energy level at an energy $h\Delta\nu$ above the ground state may then be expressed as

$$n_{\mathrm{e}}(\Delta\nu) = \frac{1}{e^{\frac{h\Delta\nu}{k_{\mathrm{B}}T}} - 1} \,. \tag{6.16}$$

For the case $N_s < 1$, it is evident that both n_{e_1} and n_{e_2} must individually satisfy $n_e(\Delta\nu) < 1$. Accordingly, for sufficiently large energy spacings $\Delta\nu$, the saturation photon number per level remains below unity. This condition imposes a constraint on the energy spacing $\Delta\nu$ at ambient temperature $T = 300$ K,

$$\Delta\nu \geq \frac{\ln(2) k_B T}{h} \approx 4.3 \text{ THz} \tag{6.17}$$

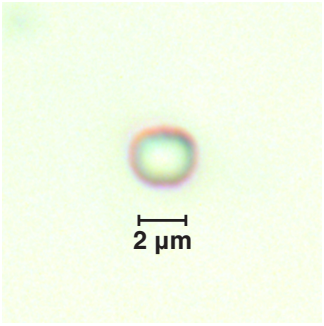

Figure 6.10: Optical microscope image of an asymmetric pillar structure fabricated using the dip-in configuration of direct laser writing (DLW).

To realise such a system, a small polymer pillar structure exhibiting transverse asymmetry is employed, with lateral dimensions $L_x = 2.29$ µm and $L_y = 1.9$ µm , was fabricated on a cavity mirror. The cavity fluorescence spectrum corresponding to this structure is shown in Figure 6.11. It is evident that the potential supports three bound states. By virtue of the transverse asymmetry, the degeneracy of the excited state here is lifted, yielding two distinct excited states rather than a one. Crucially, the measured energy spacing between the ground mode and the first excited state is 4.15 THz, corresponding to a saturation photon number of 1.06 photons on average; the energy spacing between the ground mode and the second excited state is 5.12 THz, corresponding to a saturation photon number of 0.79 photons on average, where the saturation photon numbers are calculated using Equation 6.16. Thus, the system approaches the limit in which one photon suffices to saturate a single bound level, as indicated by Equation 6.17. Taken together, the two excited states yield a total saturation photon number of 1.85 photons. However, the onset of condensation into the ground state may occur at a characteristic photon number lower than this limit due to finite-size effects [21].

Following the definition used in reference [60], the characteristic photon number for a single polarisation subspace, i.e the photon number at which the "thermal cloud" saturates, is given by $N_{ch} = k_B T/(h\Delta\nu)$, which for $\Delta\nu = 4.15$ THz yields an average value of $N_{ch} = 1.5$.

Further, measurements were performed to determine the population of each bound state as a function of the total photon number; the results are displayed in Figure 6.12. For each total photon number, the counts within the spectral regions corresponding to the individual mode extents (as defined in Figure 6.11) were recorded. Because the photon numbers involved were very low, a calibration factor converting counts to photons was obtained by averaging the ratio of ground mode counts to the theoretically expected populations at condensate fractions of 0.9, 0.85, 0.8 and 0.75. It is observed that the behaviour of the ground mode population differs markedly from that of the excited states. The excited states (shown in blue and purple

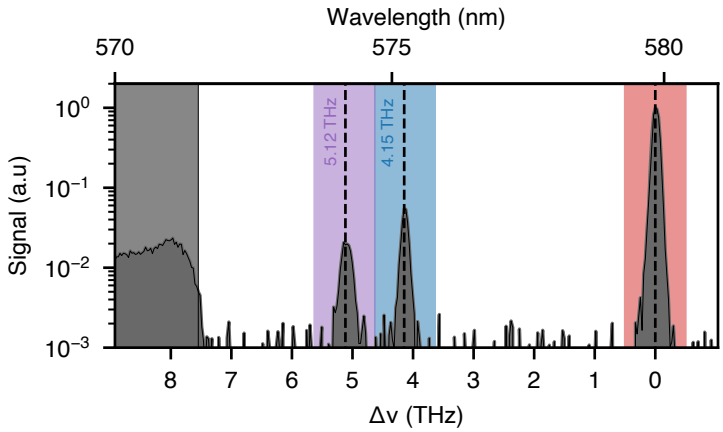

Figure 6.11: Integrated spectrum of a small asymmetric potential containing only three bound states. Due to the mode size and spectrometer resolution, the modes have finite width, which are marked by red, blue and purple shaded regions for the ground, first excited and second excited states. The onset of free space unbound states is indicated by a grey shaded region.

symbols) clearly exhibit saturation, whereas the ground mode population continues to increase as the total photon number is raised, indicating the onset of condensation into the ground state. In addition, a change in the slope of the ground mode population is apparent around 1.5 photons on average, as anticipated. The population trends of the two excited states follow the theoretical expectation and approach saturation in accordance with theory (numerically estimated). It should be noted that these observations pertain to a single polarisation subspace.

In future experiments, by fine-tuning the lateral extent and aspect ratio of the potential, the total saturation photon number may be reduced to well below one photon on average.

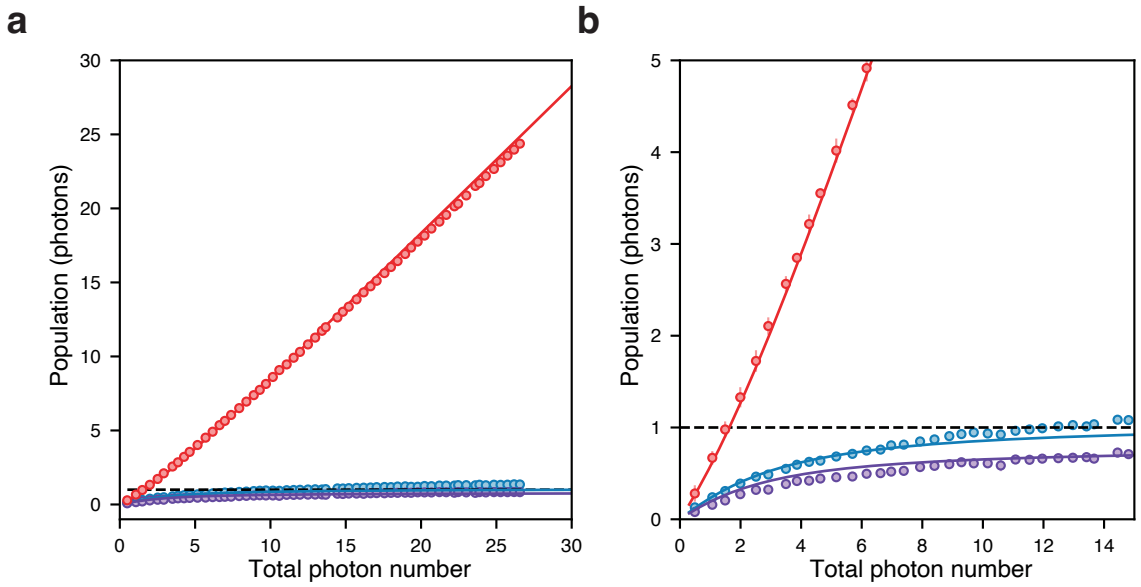

Figure 6.12: Population of the bound states as in Figure 6.11 as a function of total photon number, i.e. the summation of populations of the bound states. **a** The population in the ground mode (red symbols), first excited mode (blue symbols) and second excited mode (purple symbols). The theoretical expectation is indicated by a solid line. A horizontal dashed line represents population equal to one photon. The ground mode population increases as total photon number increases, while the excited states show saturation. **b** Zoomed-in region of plot in **a**, showing the saturation effects of excited states nearing the one photon limit, while the ground mode is observed to change slope around the one photon population mark.

CHAPTER 7

Conclusions

This thesis has presented an experimental investigation into the nature of the transition of a photon gas in a dye-filled microcavity platform, as the dimensionality is reduced from two dimensions to one dimension under harmonic confinement. It has been observed, both via population measurements and calorimetric analysis, that the isotropic two-dimensional case exhibits a Bose-Einstein condensation characteristic of an ideal Bose gas. In contrast, this sharp transition becomes softened under an intermediate anisotropic two-dimensional harmonic confinement with an aspect ratio of $\Lambda = 5$. Upon further increasing the anisotropy, a one-dimensional harmonic confinement is realised, where a smooth crossover from the classical regime to a quantum-degenerate phase is observed. This behaviour stands in stark contrast to the isotropic two-dimensional case. The realisation of such highly anisotropic and high-curvature potentials has been made possible through the implementation of Direct Laser Writing (DLW) polymer nanostructures onto a cavity mirror, marking their first use in a dye-filled microcavity photon gas platform.

As DLW has been primarily suited to the fabrication of small polymer structures, various trapping geometries have been explored to investigate its broader potential in this platform. Notably, coupled double-well potentials have been realised with minimum coupling rates that significantly exceed previous demonstrations within dye microcavities. These configurations have subsequently been employed to fabricate extended one-dimensional chains of up to twenty lattice sites, including geometries based on the Su-Schrieffer-Heeger (SSH) model. These results confirm that complex band structure engineering of extended lattice geometries is now feasible. Beyond the demonstration of well-established potential landscapes, DLW has enabled a preliminary exploration of new finite-size regimes where condensation may occur with an average occupancy of less than one photon, at which the thermal cloud saturates.

Looking forward, it would be of interest to study alternative trapping potentials for photons. In particular, potentials stronger than linear could enable Bose-Einstein condensation with phase transition signatures even in one dimension [20], and the associated spatial correlations should be investigated [122]. In finite-sized traps the correlations may still extend across the entire system. It would therefore be insightful to fix the system size, defined by spatial extent and potential depth, while varying the dispersion relation from harmonic to stronger than linear, to better explore the conditions under which phase transitions arise.

Within the dye microcavity platform, by tuning the low-frequency cutoff, photon losses can be changed from a nearly lossless regime to that of a driven-dissipative condensate [29]. This adjustment is expected to impact the system's correlations and may further influence the polarisation properties of the condensate [96, 97], which presents an interesting avenue for future research.

The DLW structuring approach demonstrated here offers significant flexibility in the engineering of photonic potentials. It enables the design of both continuous potentials such as the harmonic oscillator and discrete coupled-lattice geometries with large coupling strengths. For the one-dimensional lattices like the ones explored in this thesis, with incoherent hopping, is predicted to give rise to the bosonic skin effect [58], which could be implemented with tilted lattice with hopping mediated by bath such as dye solution. It would also be of interest to investigate whether Kardar–Parisi–Zhang (KPZ) scaling, as observed in polariton condensates, emerges in this system [25]. Extending the lattice to two dimensions is predicted to result in KPZ behaviour distinct from the one-dimensional case [123]. Furthermore, in two-dimensional driven-dissipative lattices, the formation of stable vortices is expected [59, 124], and the possibility of vortex cluster formation remains to be explored [125].

APPENDIX A

Information on optics used

Lens	Focal length (cm)
L_1	20
L_2	20
L_3	20
L_4	30
L_5	10
L_6	7.5
L_7	30
L_8	20
L_9	30
L_{10}	25

Table A.1: List of lenses mentioned in Figure 3.7 and their focal lengths.

References

[1] N. D. Mermin and H. Wagner, *Absence of Ferromagnetism or Antiferromagnetism in One- or Two-Dimensional Isotropic Heisenberg Models*, Physical Review Letters **17** (1966) 1133.

[2] P. C. Hohenberg, *Existence of Long-Range Order in One and Two Dimensions*, Physical Review **158** (1967) 383.

[3] S. Dettmer et al., *Observation of Phase Fluctuations in Elongated Bose-Einstein Condensates*, Phys. Rev. Lett. **87** (2001) 160406.

[4] P. Krüger, S. Hofferberth, I. E. Mazets, I. Lesanovsky and J. Schmiedmayer, *Weakly Interacting Bose Gas in the One-Dimensional Limit*, Phys. Rev. Lett. **105** (2010) 265302.

[5] V. L. Berezinsky, *Destruction of long range order in one-dimensional and two-dimensional systems having a continuous symmetry group. I. Classical systems*, Sov. Phys. JETP **32** (1971) 493.

[6] J. M. Kosterlitz and D. J. Thouless, *Ordering, metastability and phase transitions in two-dimensional systems*, Journal of Physics C: Solid State Physics **6** (1973) 1181.

[7] J. M. Kosterlitz, *The critical properties of the two-dimensional xy model*, Journal of Physics C: Solid State Physics **7** (1974) 1046.

[8] D. J. Bishop and J. D. Reppy, *Study of the Superfluid Transition in Two-Dimensional* ^{4}He *Films*, Physical Review Letters **40** (1978) 1727.

[9] Z. Hadzibabic, P. Krüger, M. Cheneau, B. Battelier and J. Dalibard, *Berezinskii–Kosterlitz–Thouless crossover in a trapped atomic gas*, Nature **441** (2006) 1118.

[10] R. Desbuquois et al., *Superfluid behaviour of a two-dimensional Bose gas*, Nature Physics **8** (2012) 645.

[11] P. A. Murthy et al., *Observation of the Berezinskii-Kosterlitz-Thouless Phase Transition in an Ultracold Fermi Gas*, Physical Review Letters **115** (2015) 010401.

[12] F. D. M. Haldane, *Effective Harmonic-Fluid Approach to Low-Energy Properties of One-Dimensional Quantum Fluids*, Physical Review Letters **47** (1981) 1840.

[13] T. Giamarchi, *Quantum Physics in One Dimension*, Oxford University Press, 2003.

[14] A. C. D. van Enter and J. L. van Hemmen, *Absence of phase transitions in certain one-dimensional long-range random systems*, Journal of Statistical Physics **39** (1985) 1.

[15] M. A. Norcia et al., *Two-dimensional supersolidity in a dipolar quantum gas*, Nature **596** (2021) 357.

[16] P. Richerme et al., *Non-local propagation of correlations in quantum systems with long-range interactions*, Nature **511** (2014) 198.

[17] B.-W. Li et al., *Probing Critical Behavior of Long-Range Transverse-Field Ising Model through Quantum Kibble-Zurek Mechanism*, PRX Quantum **4** (1 2023) 010302.

[18] G. Biagioni et al., *Dimensional Crossover in the Superfluid-Supersolid Quantum Phase Transition*, Physical Review X **12** (2022) 021019.

[19] Y. Guo et al., *Observation of the 2D-1D Dimensional Crossover in Strongly Interacting Ultracold Bosons*, Nature Physics (2024) doi:10.1038/s41567-024-02459.

[20] V. Bagnato and D. Kleppner, *Bose-Einstein condensation in low-dimensional traps*, Physical Review A **44** (1991) 7439.

[21] W. Ketterle and N. J. van Druten, *Bose-Einstein condensation of a finite number of particles trapped in one or three dimensions*, Physical Review A **54** (1996) 656.

[22] I. Carusotto and C. Ciuti, *Quantum fluids of light*, Rev. Mod. Phys. **85** (1 2013) 299.

[23] E. Wertz et al., *Spontaneous formation and optical manipulation of extended polariton condensates*, Nat. Phys. **6** (2010) 860.

[24] M. Wouters, T. C. H. Liew and V. Savona, *Energy relaxation in one-dimensional polariton condensates*, Phys. Rev. B **82** (2010) 245315.

[25] Q. Fontaine et al., *Kardar–Parisi–Zhang universality in a one-dimensional polariton condensate*, Nature **608** (2022) 687.

[26] Z. Li et al., *Dissipative Phase Transition with Driving-Controlled Spatial Dimension and Diffusive Boundary Conditions*, Phys. Rev. Lett. **128** (9 2022) 093601.

[27] J. Klaers, J. Schmitt, F. Vewinger and M. Weitz, *Bose–Einstein condensation of photons in an optical microcavity*, Nature **468** (2010) 545.

[28] E. Busley et al., *Compressibility and the equation of state of an optical quantum gas in a box*, Science **375** (2022) 1403.

[29] F. E. Öztürk et al., *Observation of a non-Hermitian phase transition in an optical quantum gas*, Science **372** (2021) 88.

[30] E. Stein and A. Pelster, *Thermodynamics of trapped photon gases at dimensional crossover from 2D to 1D*, New J. Phys. **24** (2022) 023013.

[31] C. Kurtscheid et al., *Realizing arbitrary trapping potentials for light via direct laser writing of mirror surface profiles*, Europhys. Lett. **130** (2020) 54001.

[32] A. Redmann et al., *Bose-Einstein Condensation of Photons in a Four-Site Quantum Ring*, Physical Review Letters **133** (2024) 093602.

[33] S. Maruo, O. Nakamura and S. Kawata, *Three-dimensional microfabrication with two-photon-absorbed photopolymerization*, Optics Letters **22** (1997) 132.

[34] C. N. LaFratta, J. T. Fourkas, T. Baldacchini and R. A. Farrer, *Multiphoton Fabrication*, Angewandte Chemie International Edition **46** (2007) 6238.

[35] M. Malinauskas, M. Farsari, A. Piskarskas and S. Juodkazis, *Ultrafast laser nanostructuring of photopolymers: A decade of advances*, Physics Reports **533** (2013) 1.

[36] M. Thiel, J. Fischer, G. von Freymann and M. Wegener, *Direct laser writing of three-dimensional submicron structures using a continuous-wave laser at 532 nm*, Applied Physics Letters **97** (2010) 221102.

[37] J. Fischer, G. von Freymann and M. Wegener, *The Materials Challenge in Diffraction-Unlimited Direct-Laser-Writing Optical Lithography*, Advanced Materials **22** (2010) 3578.

[38] J. K. Hohmann, M. Renner, E. H. Waller and G. von Freymann, *Three-Dimensional μ-Printing: An Enabling Technology*, Advanced Optical Materials **3** (2015) 1488.

[39] S. Coelho, J. Baek, J. Walsh, J. Justin Gooding and K. Gaus, *Direct-laser writing for subnanometer focusing and single-molecule imaging*, Nature Communications **13** (2022) 647.

[40] C. R. Ocier et al., *Direct laser writing of volumetric gradient index lenses and waveguides*, Light: Science & Applications **9** (2020) 196.

[41] M. Deubel, M. Wegener, S. Linden, G. v. Freymann and S. John, *3D-2D-3D photonic crystal heterostructures fabricated by direct laser writing*, Optics Letters **31** (2006) 805.

[42] M. S. Rill et al., *Photonic metamaterials by direct laser writing and silver chemical vapour deposition*, Nature Materials **7** (2008) 543.

[43] T. Gissibl, S. Thiele, A. Herkommer and H. Giessen, *Two-photon direct laser writing of ultracompact multi-lens objectives*, Nature Photonics **10** (2016) 554.

[44] J. Schulz and G. von Freymann, *Broadband Mode Division Multiplexing of OAM-Modes by a Micro Printed Waveguide Structure*, Advanced Optical Materials **12** (2024) 2302597.

[45] W. P. Su, J. R. Schrieffer and A. J. Heeger, *Solitons in Polyacetylene*, Physical Review Letters **42** (1979) 1698.

[46] E. Fradkin and J. E. Hirsch, *Phase diagram of one-dimensional electron-phonon systems. I. The Su-Schrieffer-Heeger model*, Physical Review B **27** (1983) 1680.

[47] E. J. Meier, F. A. An and B. Gadway, *Observation of the topological soliton state in the Su–Schrieffer–Heeger model*, Nature Communications **7** (2016) 13986.

[48] W. Yan, B. Zhang and F. Chen, *Photonic topological insulators in femtosecond laser direct-written waveguides*, npj Nanophotonics **1** (2024) 40.

[49] M. Kardar, G. Parisi and Y.-C. Zhang, *Dynamic Scaling of Growing Interfaces*, Physical Review Letters **56** (1986) 889.

[50] E. Altman, L. M. Sieberer, L. Chen, S. Diehl and J. Toner, *Two-Dimensional Superfluidity of Exciton Polaritons Requires Strong Anisotropy*, Physical Review X **5** (2015) 011017.

[51] K. Ji, V. N. Gladilin and M. Wouters, *Temporal coherence of one-dimensional nonequilibrium quantum fluids*, Physical Review B **91** (2015) 045301.

[52] L. He, L. M. Sieberer, E. Altman and S. Diehl, *Scaling properties of one-dimensional driven-dissipative condensates*, Physical Review B **92** (2015) 155307.

[53] A. Zamora, L. M. Sieberer, K. Dunnett, S. Diehl and M. H. Szymańska, *Tuning across Universalities with a Driven Open Condensate*, Physical Review X **7** (2017) 041006.

[54] P. Comaron et al., *Dynamical Critical Exponents in Driven-Dissipative Quantum Systems*, Physical Review Letters **121** (2018) 095302.

[55] D. Squizzato, L. Canet and A. Minguzzi, *Kardar-Parisi-Zhang universality in the phase distributions of one-dimensional exciton-polaritons*, Physical Review B **97** (2018) 195453.

[56] I. Amelio and I. Carusotto, *Theory of the Coherence of Topological Lasers*, Physical Review X **10** (2020) 041060.

[57] A. Ferrier, A. Zamora, G. Dagvadorj and M. H. Szymańska, *Searching for the Kardar-Parisi-Zhang phase in microcavity polaritons*, Physical Review B **105** (2022) 205301.

[58] L. Garbe, Y. Minoguchi, J. Huber and P. Rabl, *The bosonic skin effect: Boundary condensation in asymmetric transport*, SciPost Phys. **16** (2024) 029.

[59] V. N. Gladilin and M. Wouters, *Vortices in Nonequilibrium Photon Condensates*, Physical Review Letters **125** (2020) 215301.

[60] C. Kurtscheid, A. Redmann, F. Vewinger, J. Schmitt and M. Weitz, *Thermodynamics and State Preparation in a Two-State System of Light*, arXiv.org, 2024.

[61] J. Klaers, F. Vewinger and M. Weitz, *Thermalization of a two-dimensional photonic gas in a 'white wall' photon box*, Nature Phys **6** (2010) 512.

[62] C. J. Pethick and H. Smith, *Bose–Einstein Condensation in Dilute Gases*, 2nd ed., Cambridge: Cambridge University Press, 2008.

[63] A. V. Kavokin, J. J. Baumberg, G. Malpuech and F. P. Laussy, *Microcavities*, 2nd ed., Oxford: Oxford University Press, 2022.

[64] M. Kardar, *Statistical Physics of Particles*, Higher Education from Cambridge University Press, 2007.

[65] K. Huang, *Statistical Mechanics*, 2nd, Weinheim, Germany: Wiley & Sons Ltd, 1988 496.

[66] F. Dalfovo, S. Giorgini, L. P. Pitaevskii and S. Stringari, *Theory of Bose–Einstein Condensation in Trapped Gases*, Reviews of Modern Physics **71** (1999) 463.

[67] L. P. Pitaevskii and S. Stringari, *Bose–Einstein Condensation*, Oxford, UK: Oxford University Press, 2003.

[68] K. B. Davis et al., *Bose-Einstein Condensation in a Gas of Sodium Atoms*, Physical Review Letters **75** (1995) 3969.

[69] M. H. Anderson, J. R. Ensher, M. R. Matthews, C. E. Wieman and E. A. Cornell, *Observation of Bose-Einstein condensation in a dilute atomic vapor*, Science (New York, N.Y.) **269** (1995) 198.

[70] R. Shankar, *Principles of Quantum Mechanics*, 2nd, New York: Springer, 1994.

[71] T. Damm et al., *Calorimetry of a Bose–Einstein-condensed photon gas*, Nat Commun **7** (2016) 11340.

[72] M. Aaboud et al., *Evidence for light-by-light scattering in heavy-ion collisions with the ATLAS detector at the LHC*, Nature Phys **13** (2017) 852.

[73] M. Pieczarka et al., *Bose–Einstein condensation of photons in a vertical-cavity surface-emitting laser*, Nat. Photon. **18** (2024) 1090.

[74] R. C. Schofield et al., *Bose–Einstein condensation of light in a semiconductor quantum well microcavity*, Nature Photonics **18** (2024) 1083.

[75] R. Weill, A. Bekker, B. Levit and B. Fischer, *Bose-Einstein condensation of photons in a long fiber cavity*, Opt. Express, OE **29** (2021) 27807.

[76] J. Schmitt, M. Weitz and J. Klaers, *Absorption and Emission Spectral Data of Room-temperature Rhodamine 6G Dye Solution and some typical Dye Microcavity parameters*, Zenodo, 2024.

[77] J. Schmitt, *Dynamics and correlations of a Bose–Einstein condensate of photons*, Journal of Physics B: Atomic, Molecular and Optical Physics **51** (2018) 173001.

[78] R. F. Kubin and A. N. Fletcher, *Fluorescence quantum yields of some rhodamine dyes*, Journal of Luminescence **27** (1982) 455.

[79] D. Magde, R. Wong and P. G. Seybold, *Fluorescence Quantum Yields and Their Relation to Lifetimes of Rhodamine 6G and Fluorescein in Nine Solvents: Improved Absolute Standards for Quantum Yields*, Photochemistry and Photobiology **75** (2002) 327.

[80] J. R. Lakowicz, *Principles of Fluorescence Spectroscopy*, 3rd, New York: Springer, 2006.

[81] G. Angel, R. Gagel and A. Laubereau, *Femtosecond relaxation dynamics in the electronic ground state of dye molecules studied by polarization-dependent amplification spectroscopy*, Chemical Physics Letters **156** (1989) 169.

[82] E. H. Kennard, *On The Thermodynamics of Fluorescence*, Physical Review **11** (1918) 29.

[83] J. Schmitt et al., *Thermalization kinetics of light: From laser dynamics to equilibrium condensation of photons*, Physical Review A **92** (2015) 011602.

[84] F. E. Öztürk, F. Vewinger, M. Weitz and J. Schmitt, *Fluctuation-Dissipation Relation for a Bose-Einstein Condensate of Photons*, Physical Review Letters **130** (2023) 033602.

[85] M. Rigol, V. Dunjko and M. Olshanii, *Thermalization and its mechanism for generic isolated quantum systems*, Nature **452** (2008) 854.

[86] J.-S. Caux and J. Mossel, *Remarks on the notion of quantum integrability*, Journal of Statistical Mechanics: Theory and Experiment **2011** (2011) P02023.

[87] T. Kinoshita, T. Wenger and D. S. Weiss, *A quantum Newton's cradle*, **440** (2006) 900.

[88] M. Gring et al., *Relaxation and Prethermalization in an Isolated Quantum System*, Science **337** (2012) 1318.

[89] F. Herrmann and P. Schmälzle, *Simple explanation of a well-known collision experiment*, American Journal of Physics **49** (1981) 761.

[90] L. Vidmar and M. Rigol, *Generalized Gibbs ensemble in integrable lattice models*, Journal of Statistical Mechanics: Theory and Experiment **2016** (2016) 064007.

[91] A. Rodin, B. A. Olsen, M. Choi and A. Tan, *Microscopic theory of thermalization in one dimension with nonlinear bath coupling*, Physical Review Research **4** (2022) 033057.

[92] C. Zanoci, Y. Yoo and B. Swingle, *Thermalization at low temperatures via weakly damped multisite baths*, Physical Review B **108** (2023) 035156.

[93] C. Kurtscheid et al., *Thermally condensing photons into a coherently split state of light*, Science **366** (2019) 894.

[94] A. Freise, *GW Optics Component Library*, `https://www.gwoptics.org/ComponentLibrary/`, 2010.

[95] L. Song, E. J. Hennink, I. T. Young and H. J. Tanke, *Photobleaching kinetics of fluorescein in quantitative fluorescence microscopy.*, Biophysical Journal **68** (1995) 2588.

[96] R. I. Moodie, P. Kirton and J. Keeling, *Polarization dynamics in a photon Bose-Einstein condensate*, Physical Review A **96** (2017) 043844.

[97] S. Enns, J. Schulz, K. Karkihalli Umesh, F. Vewinger and G. v. Freymann, *Polarization properties of photon Bose-Einstein condensates*, 2025, arXiv:2506.06141.

[98] R. W. Gerchberg and W. O. Saxton, *A practical algorithm for the determination of phase from image and diffraction plane pictures*, Optik **35** (1972) 237.

[99] T. Haist, M. Schönleber and H. J. Tiziani, *Computer-generated holograms from 3D-objects written on twisted-nematic liquid crystal displays*, Optics Communications **140** (1997) 299.

[100] G. Sinclair et al., *Interactive application in holographic optical tweezers of a multi-plane Gerchberg-Saxton algorithm for three-dimensional light shaping*, Optics Express **12** (2004) 1665.

[101] B. Saleh and M. Teich, *Fundamentals of Photonics, 3rd Edition*, 2019.

[102] L. Yuan, Q. Song, H. Liu, K. Heggarty and W. Cai, *Super-resolution computed tomography imaging spectrometry*, Photonics Research **11** (2023) 212.

[103] P. Zhou, Y. Lv, Y. Zheng, J. Zhou and L. Chen, *CTIS spectral image reconstruction technology based on slit-scanning architecture*, Optics Express **32** (2024) 25276.

[104] R. Weill, A. Bekker, B. Levit and B. Fischer, *Bose–Einstein condensation of photons in an erbium–ytterbium co-doped fiber cavity*, Nature Communications **10** (2019) 747.

[105] K. Karkihalli Umesh, *Investigation of 3D Printed Potentials for Photon Gases*, Masterarbeit in Physik: Institut für Angewandte Physik, Rheinische Friedrich-Wilhelms-Universität Bonn, 2021.

[106] J. Klärs, *Bose-Einstein-Kondensation von paraxialem Licht*, Thesis: Universitäts- und Landesbibliothek Bonn, 2011.

[107] D. Hunger, C. Deutsch, R. J. Barbour, R. J. Warburton and J. Reichel, *Laser micro-fabrication of concave, low-roughness features in silica*, AIP Advances **2** (2012) 012119.

[108] B. T. Walker et al., *Driven-dissipative non-equilibrium Bose–Einstein condensation of less than ten photons*, Nature Physics **14** (2018) 1173.

[109] D. Dung et al., *Variable potentials for thermalized light and coupled condensates*, Nature Photonics **11** (2017) 565.

[110] T. Gissibl, S. Wagner, J. Sykora, M. Schmid and H. Giessen, *Refractive index measurements of photo-resists for three-dimensional direct laser writing*, Optical Materials Express **7** (2017) 2293.

[111] Erik Busley, *Investigation of Paraxial Light Concentration and Homogeneously Trapped Two-Dimensional Optical Quantum Gases*, PhD thesis: Rheinische Friedrich-Wilhelms-Universität Bonn, 2022.

[112] M. Calvanese Strinati, F. Vewinger and C. Conti, *Nonlocality-induced surface localization in Bose-Einstein condensates of light*, Phys. Rev. A **105** (4 2022) 043318.

[113] A. Griesmaier, J. Werner, S. Hensler, J. Stuhler and T. Pfau, *Bose–Einstein Condensation of Chromium*, Physical Review Letters **94** (2005) 160401.

[114] Y. Tang and et al., *Anisotropic Expansion of a Dipolar Bose–Einstein Condensate*, New Journal of Physics **17** (2015) 045006.

[115] R. W. Robinett, *Visualizing the solutions for the circular infinite well in quantum and classical mechanics*, American Journal of Physics **64** (1996) 440.

[116] D. J. Griffiths and D. F. Schroeter, *Introduction to Quantum Mechanics*, 3rd ed., Cambridge University Press, 2018.

[117] R. Nyman, H. Dhar, J. Rodrigues and F. Mintert, *Phase transitions of light in a dye-filled microcavity: observations and simulations*, Journal of Physics: Conference Series **1919** (2021) 012006.

[118] A. Einstein, *Zur Quantentheorie der Strahlung*, Physikalische Zeitschrift **18** (1917) 121.

[119] G. S. Agarwal, "Quantum statistical theories of spontaneous emission and their relation to other approaches", *Quantum Optics*, ed. by G. Höhler, Berlin, Heidelberg: Springer, 1974 1.

[120] M. O. Scully and M. S. Zubairy, *Quantum Optics*, Cambridge: Cambridge University Press, 1997.

[121] M. A. Macovei, *Dense dipole-dipole-coupled two-level systems in a thermal bath*, Physical Review A **110** (2024) 023712.

[122] T. Damm, D. Dung, F. Vewinger, M. Weitz and J. Schmitt, *First-order spatial coherence measurements in a thermalized two-dimensional photonic quantum gas*, Nature Communications **8** (2017) 158.

[123] K. Deligiannis et al., *Kardar-Parisi-Zhang universality in discrete two-dimensional driven-dissipative exciton polariton condensates*, Physical Review Research **4** (2022) 043207.

[124] V. N. Gladilin and M. Wouters, *Vortex-pair annihilation in arrays of photon cavities*, Phys. Rev. A **105** (1 2022) 013527.

[125] R. Panico et al., *Onset of vortex clustering and inverse energy cascade in dissipative quantum fluids*, Nature Photonics **17** (2023) 451.

Acknowledgements

I extend my sincere gratitude to Prof. Dr. Martin Weitz and Dr. Frank Vewinger for their willingness to serve as my PhD supervisor. Additionally, I would like to express my profound appreciation to Prof. Dr. Georg von Freymann for accepting the role of my second reviewer for my PhD dissertation.

This project was a collaborative endeavour between the University of Bonn and the RPTU Kaiserslautern. I would like to express my gratitude to Prof. Dr. Georg von Freymann and Dr. Julian Schulz for their unwavering optimism and positive attitude throughout the numerous iterations of the design and fabrication process of polymer structures. In later years, I also want to acknowledge Sven Enns for fabricating the structures. Furthermore, I would like to thank Priv.-Doz. Dr. Axel Pelster, Dr. Enrico Stein, and Joschua Krauß for their insightful discussions on theoretical aspects. I would also like to express my gratitude to several members of the working group who made it enjoyable to discuss physics. These include Prof. Dr. Julian Schmitt, Dr. Andreas Redmann, and Dr. Andris Erglis.

Dr. Frank Vewinger was the one person who could provide guidance and support on a wide range of issues, from finding a suitable cable to explaining the rationale behind our research. I am deeply grateful for your mentorship and unwavering support.

My mentors played a pivotal role in my academic journey. I would particularly like to express my gratitude to Mrs. Sheela, who provided invaluable guidance during my high school years in Koppal. Additionally, I am indebted to Prof. Dr. Arun Varma Thampan and Prof. Dr. Sivarani Thirupathi, who guided and encouraged me during my B.Sc. years in Bengaluru. Their support was instrumental in helping me persevere my master's degree abroad.

Living abroad for an extended period and managing academic deadlines and stress, especially in the current uncertain world, presented significant challenges. However, I gradually realised the importance of maintaining mental well-being in such circumstances. I would like to express my gratitude to my friends who assisted me in seeking appropriate support, particularly Steffi Moll and Susmitha Acharya. Finally, I want to thank my parents and my brother for their unwavering support throughout every new adventure I embarked on.